CHALMERS

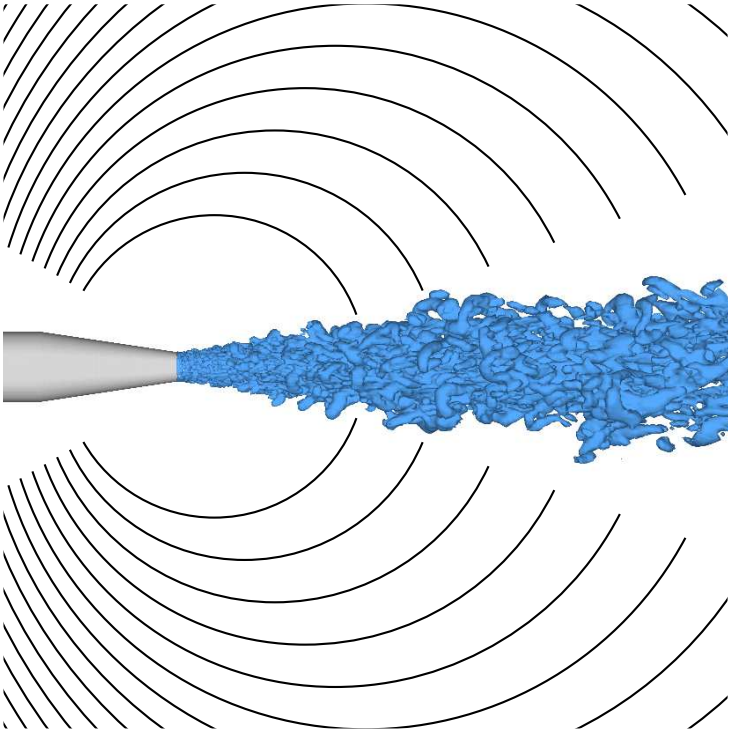

A Study of Mach 0.75 Jets and Their Radiated Sound Using Large-Eddy Simulation

NIKLAS ANDERSSON

Division of Thermo and Fluid Dynamics
CHALMERS UNIVERSITY OF TECHNOLOGY
Göteborg, Sweden, 2003

THESIS FOR THE DEGREE OF LICENTIATE IN ENGINEERING

A Study of Mach 0.75 Jets and Their Radiated Sound Using Large-Eddy Simulation

NIKLAS ANDERSSON

Division of Thermo and Fluid Dynamics

CHALMERS UNIVERSITY OF TECHNOLOGY

Göteborg, Sweden, 2003

A Study of Mach 0.75 Jets and Their Radiated Sound Using Large-Eddy Simulation

NIKLAS ANDERSSON

ISSN 1101-9972
ISRN CTH-TFD-PB-03/05

Institutionen för termo- och fluiddynamik
Chalmers Tekniska Högskola
SE-412 96 Göteborg, Sweden
Phone +46-(0)31-7721400
Fax: +46-(0)31-180976

Printed at Chalmers Reproservice
Göteborg, Sweden 2003

A Study of Mach 0.75 Jets and Their Radiated Sound Using Large-Eddy Simulation

by
Niklas Andersson
nian@tfd.chalmers.se
Division of Thermo and Fluid Dynamics
Chalmers University of Technology
SE-412 96 Göteborg
Sweden

Abstract

Large-Eddy Simulations (LES) of a compressible nozzle/jet configuration have been carried out. Two jets were simulated, an isothermal jet and a jet with a higher temperature than the surrounding air. The Mach number was in both cases 0.75 and the jet Reynolds number was 5.0×10^4. Sound pressure levels in far-field observer locations were evaluated using both Kirchhoff surface integration and Lighthill's acoustic analogy. The Favre filtered Navier-Stokes equations were solved using a finite volume method solver with a low dissipative third-order upwind scheme for the convective fluxes, a second-order centered difference approach for the viscous fluxes and a three-stage second-order Runge-Kutta time marching technique. The computational domain was discretized using a block structured boundary fitted mesh with approximately 3.0×10^6 cells. The calculations were performed on a parallel computer, using message-passing interface (MPI). A compressible form of Smagorinsky's subgrid scale model was used for computation of the subgrid scale stresses. Absorbing boundary conditions based on characteristic variables were adopted for all free boundaries. Velocity components specified at the entrainment boundaries were estimated from corresponding Reynolds Averaged Navier-Stokes (RANS) calculations, which enable the use of a rather narrow domain. This, furthermore, ensures that the correct amount of fluid is entrained into the domain. Two-point space-time correlations were obtained for locations in the shear layer center, from which length and time scales of turbulence structures were evaluated. Aerodynamic results and predicted sound pressure levels are both in good agreement with experiments. Experimental data were provided by Laboratoire d'Etude Aerodynamiques, Poitiers, France, (Jordan *et al.*, 2002*a*,*b*; Jordan & Gervais, 2003).

Preface

Chapter 7.1 is based on a paper presented at the 9th AIAA/CEAS Aeroacoustic Conference and Exhibit, Hilton Head, South Carolina, May 12-14, 2003, (Andersson *et al.*, 2003).

Acknowledgments

This work was conducted at the Division of Thermo and Fluid Dynamics at Chalmers University of Technology as part of the EU 5th Framework Project JEAN (Jet Exhaust Aerodynamics & Noise), contract number G4RD-CT2000-000313.

I would like to express my gratitude to my supervisors, Prof. Lars Davidson, for all good advice and for encouraging me during my work, and Prof. Lars-Erik Eriksson, for sharing his great knowledge concerning compressible flows and numerical methods.

I would also like to thank all participants in the JEAN project for fruitful discussions at the project meetings.

Many thanks to Peter Jordan and co-workers at Laboratoire d'Etude Aeródynamiques, Poiters, France, for providing us with experimental data. Special thanks to Peter Jordan for always having time to answer my questions and for showing interest in our work.

Computational resources provided by UNICC at Chalmers and the by national resource NSC, are gratefully acknowledged.

Finally, I would like to thank my colleagues at the Division of Thermo and Fluid Dynamics for creating a stimulating working atmosphere.

Nomenclature

Upper-case Roman

C_p	specific heat at constant pressure
$C_R,\ C_I$	Smagorinsky model coefficients
D_j	nozzle outlet diameter
$\mathcal{F}_j$	flux component
L_c	potential core length
$\mathcal{L}$	integral length scale
Pr	Prandtl number
Q	state vector in equations on conservative form
Re_D	Reynolds number based on the jet diameter
R	gas constant
R	correlation amplitude
S_{ij}	strain rate tensor
$\mathcal{S}_j$	cell face area normal vector
St	Strouhal number $(St = (f D_j)/U_j)$
T	temperature
$\mathcal{T}$	integral time scale

Lower-case Roman

c	speed of sound
e	energy
f	frequency
h	enthalpy
k	kinetic energy
p	pressure
q	state vector in equations on primitive form
q_j	energy diffusion vector
r	radial coordinate
r	distance from source to observer
r_i	component of vector from source to observer

t	time
u_i	cartesian components of velocity vector
u	axial velocity component
v	radial velocity component
w	tangential velocity component
x_i	cartesian coordinate vector component
$\mathbf{x}$	flow field location
$\mathbf{x}$	observer location
$\mathbf{y}$	source location

Upper-case Greek

Δ	filter width
Ω_{ij}	rotation tensor

Lower-case Greek

δ_{ij}	Kronecker delta
ε_ν	viscous dissipation
θ	angle from the x-axis
μ	viscosity
ν	kinematic viscosity ($\nu = \mu/\rho$)
ξ	spatial separation
ρ	density
σ_{ij}	viscous stress tensor
τ	temporal separation
τ_{ij}	subgrid scale stress tensor
τ_r	retarded time

Subscripts

c	center line
E	Eulerian
j	jet, nozzle exit condition
L	Lagrangian
t	turbulent quantity
0	total condition
∞	free stream or ambient conditions

Superscripts

c	convection

SGS	subgrid scale
$\sim$	Favre filtered quantity
$-$	spatially filtered quantity
$''$	unresolved quantity
$'$	resolved fluctuation

Symbols

$\langle \ldots \rangle_t$	time averaged quantity
$\langle \ldots \rangle_\theta$	circumferentially averaged quantity

Abbreviations

CAA	Computational Aero Acoustics
CFD	Computational Fluid Dynamics
CFL	Courant-Friedrichs-Lewy
DNS	Direct Numerical Simulation
HBR	High By-pass Ratio
LDV	Laser Doppler Velocimetry
LEE	Linearized Euler Equations
LES	Large Eddy Simulation
MPI	Message Passing Interface
OASPL	Overall Sound Pressure Level
RANS	Reynolds Averaged Navier-Stokes
SPL	Sound Pressure Level

Contents

Chapter 1

Introduction

1.1 Motivation

The number of commercial aircraft in service is continuously increasing and airports around the world are growing in size. Moreover, new airports are often built in the vicinity of cities. Restrictions of noise levels in the surroundings of airports have made the reduction of near-ground operation noise an important issue for aircraft and engine manufacturers, and noise generation has now become an important design factor that is taken into consideration early in the construction process. Flow-induced aircraft noise can be divided into two categories: airframe noise and noise generated by the jet engine. The first category includes noise generated by landing gear, high lift devices and the aircraft fuselage itself and the second includes turbo-machinery noise, core noise and jet noise. At take-off, the main sources of noise are the propelling jet and the engine fan, of which the jet exhaust is usually the strongest noise source at full power. In commercial aircraft, increasing the by-pass ratio, i.e. the ratio of air passing through the engine core to the air passing the engine in a by-pass duct, has given a significant reduction in aircraft noise. However, although increasing the by-pass ratio leads to reduced noise levels, the major motivation for this development has not been noise reduction. Rather, the development towards more efficient engines has lead to the use of a higher by-pass ratio with noise reduction as a positive side effect. The lower noise levels of high by-pass ratio (HBR) engines are directly attributable to the reduction in jet noise resulting from lower jet velocities. Unfortunately, without a step change in technology, the maximum by-pass ratio is limited by a number of factors, e.g. the length of the fan blades, rotor speed and engine nacelle drag, and large engines are currently very close to this limit. Consequently, the possibility for reducing jet noise by increasing

the by-pass ratio is rapidly decreasing. Other techniques to lower the noise levels have been investigated in the past decades. Among these concepts, many are of a mixing enhancement nature, e.g. chevrons, lobed mixers and tabs. The lobed mixer efficiently evens out velocity differences of the core flow and the by-pass flow, which reduces the exhaust velocity and hence the sound generated. Chevrons and tabs are both devices added to the nozzle geometry that protrude into the flow and thereby enhance the mixing of core, fan and ambient air streams. While these noise-reducing concepts have proven to be able to lower the noise levels, the reduction comes with an efficiency penalty. The contradiction of noise reduction for near-ground operation and requirements for higher thrust and engine efficiency at cruise conditions will probably be common for all new noise-reducing concepts. Furthermore, requirements for higher thrust are often satisfied by increasing the flow through existing engines with only minor modifications, which leads to higher exhaust velocities and temperatures and increases the contribution of the jet to the overall noise.

New noise-reducing concepts will arise from a better understanding of the source mechanisms. For evaluation of the performance of these new concepts, reliable methods for modeling of the source mechanisms must be available. An EU project, JEAN[1], that focuses on investigating jet noise both numerically and experimentally and has a long term aim to improve existing noise predicting tools, was started in February 2001. Various known methodologies for noise prediction will be tested in the project and compared for a few test cases. The work presented in this thesis has been done within this project.

1.2 Turbulent Free Jet

The turbulent free jet is an example of a free shear flow, i.e. a flow with mean flow gradients that develop in the absence of boundaries (George, 2000). Such a flow is characterized by a main flow direction in which the velocity is significantly larger than in the transverse direction. The gradients in the transversal direction are also much larger than those in the main direction. A turbulent jet appears when fluid is continuously added locally to otherwise stagnant or at least irrotational surroundings. These kinds of flows are common in nature and in engineering applications. Examples are the residual gases spread into

[1]Jet Exhaust Aerodynamics and Noise, EU 5th Framework Project, contract number G4RD-CT2000-000313

the atmosphere by a furnace chimney and the propelling jet of an aircraft engine. The turbulent jet is separated from its non-turbulent surroundings by an interface often referred to as the viscous superlayer, by analogy with the viscous sublayer of a boundary layer, or the Corrsin superlayer after its discoverer (Hinze, 1975; George, 2000). The shape of the interface is random and continuously changing and its thickness is characterized by the Kolmogorov microscale (George, 2000). The flow in these outer regions of the jet is therefore intermittent in nature, i.e. sometimes turbulent and sometimes not, as the shape of the jet and its interface with the surroundings changes. The level of intermittancy increases radially outwards through the jet shear layer. Minimum intermittancy is found in the radial location in which the shear is highest. Levels of intermittancy in the jet have been measured by e.g. Wygnanski & Fiedler (1969). The shape of the interface is strongly affected by the turbulent flow below it and then mainly by the larger structures of the flow (Hinze, 1975; George, 2000). The motion of the interface induces irrotational fluid motion of the surrounding fluid.

The amount of turbulent fluid continuously increases downstream due to entrainment, i.e. fluid is added to the turbulent jet from its surroundings. The entrainment process causes the jet to spread in the transversal direction, and the jet flow can therefore never reach homogeneity (George, 2000). As long as the jet remains turbulent, the range of scales present in the jet will increase due to the increasing size of the jet. In the entrainment process, mass is continuously added to the turbulent jet, but no momentum is added.

Figure 1.1 shows the development of a jet. Fluid is continuously added through a nozzle to a surrounding of ambient air. As it exits the nozzle, the flow of the high velocity fluid is fully aligned with the nozzle wall, and a core region of potential flow is formed. A shear layer is generated between the high velocity fluid and its surroundings. The thickness of this shear layer depends on the boundary layer thickness at the nozzle exit. Due to entrainment of ambient fluid, the shear layer grows in size downstream. As the width of the shear layer increases, the radial extent of the potential core region decreases and more and more of the flow becomes turbulent. Shortly after the potential core closure, the entire jet is turbulent and thus fully developed.

The jet becomes self-preserving or self-similar in the fully developed region. This means that profiles of mean flow quantities can be collapsed by proper scaling. It has long been assumed that these self-

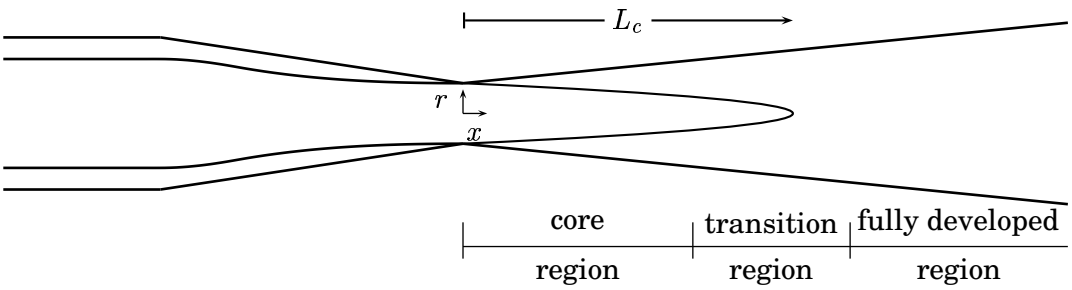

Figure 1.1: Flow regions in a developing jet.

similar profiles are independent of initial conditions for all quantities and therefore universal for all jets. This assumption has been questioned by George (1989), however.

LES and DNS have been used for jet flow applications in a number of publications. These mostly study jets at moderate Reynolds number due to the high computational costs of performing simulations of a high Reynolds number jet. Many of these studies have been carried out in order to predict jet noise. However, as it is a free shear flow frequently occurring in both nature and industrial applications, the jet is interesting to study in itself. Some studies are thus pure investigations of flow phenomena.

The feasibility of using LES for both the flow field and the radiated sound from a high subsonic 6.5 $\times$ 10^4 Reynolds number jet has been discussed by Bogey *et al.* (2000*a*, 2001, 2003). Bogey & Bailly (2003) investigated the effects of inflow conditions on flow field and radiated sound of a high Reynolds number, Re_D =4.0 $\times$ 10^5, Mach 0.9 jet. Freund (2001) investigated sources of sound in a Mach 0.9 jet at a Reynolds number of Re_D =3.6 $\times$ 10^3 using DNS. In this work the part of the Lighthill source that may radiate to the far-field was isolated using Fourier methods. The flow field and the radiated sound of a supersonic low Reynolds number jet (Mach 1.92, Re_D=2.0 $\times$ 10^3) was predicted using DNS by Freund *et al.* (2000). DeBonis & Scott (2001) used LES to obtain the flow field of a supersonic high Reynolds number jet (Mach 1.4, Re_D =1.2 $\times$ 10^6) from which two-point space-time correlations in the jet shear layer were obtained. In this study the nozzle geometry was included in the calculation domain. Shur *et al.* (2003) made simulations of a cold Mach 0.9 jet at a Reynolds number of 1.0 $\times$ 10^4. Radiated sound was successfully predicted using Ffowcs Williams-

Hawkings surface integral formulation. The simulation was conducted using only 5.0×10^5 cells. Ribault *et al.* (1999) performed large eddy simulations of a plane jet at two Reynolds numbers, Re =3.0×10^3 and Re =3.0×10^4. Simulations were performed for both Reynolds numbers using different subgrid scale models to investigate the ability of the models to capture the jet flow physics. Boersma *et al.* (1998) used DNS to study the effect of inflow conditions on the self-similar region of a round jet. The Reynolds number in this study was 2.4×10^3. Zhao *et al.* (2001) conducted an LES of a Mach 0.9 jet at Reynolds number 3.6×10^3 and a jet at Mach 0.4 and a Reynolds number of 5.0×10^3. In this study, radiated sound was obtained both directly from the LES and by using Kirchhoff surface integration. The effect on the radiated sound of the subgrid scale model used was investigated. Rembold *et al.* (2002) investigated the flow field of a rectangular jet at Mach 0.5 and a Reynolds number of 5.0×10^3 using DNS.

1.3 Jet Noise

Investigation of jet noise was more or less initiated in 1952 when Lighthill proposed his acoustic analogy in the first of his two-part paper on aerodynamically generated sound (Lighthill, 1952, 1953). These publications focused mainly on the sound generated by turbulent jets, but the acoustic analogy presented therein has been used extensively for numerous applications in the research area of aeroacoustics. The understanding of flow-induced noise, for example jet noise, is strongly coupled to the understanding of turbulence since the sources of sound are defined by the turbulent flow itself. Fifty years ago when jet noise research was initiated, turbulence was regarded as consisting of randomly distributed small eddies. Thus the research focused on the noise generated by fine scale structures. The research focus was changed with the discovery of large turbulence structures in free shear flows in the early 1970s and it was believed that, for high speed jets, the dominant part of the sound generated was generated by these large structures. More recent analysis has shown that both the fine scales and the larger structures are responsible for the noise that is generated (Tam, 1998).

In jet flows, the sound-generating structures are convected downstream by the mean flow. It can be shown that moving sources tend to radiate more sound in the direction in which the source is transported (Tam, 1998; Ribner, 1969). Moreover, the sound generated is affected by the mean convection such that when the wave front propagates through

the jet on the way to the far-field region its path tends to bend away from the jet axis. The reason for this is that the convection velocity is highest in the centerline regions, A, and lower in the outer jet regions, B, see figure 1.2. This effect is referred to as refraction and creates a cone of relative silence downstream of the noise-generating region since less sound is radiated in this direction. The refraction effect is more noticeable for jets with a higher temperature than the surrounding fluid since the speed of sound then varies over the jet cross section (Tam, 1998).

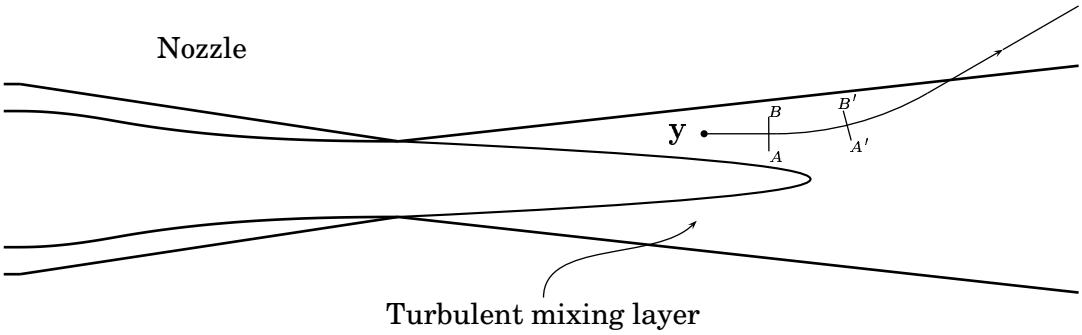

Figure 1.2: Refraction of a sound wave generated at position y in the shear layer and propagating through the jet. A wave front defined by the line AB is propagating downstream at a velocity defined by the speed of sound and the local flow velocity. The flow velocity is higher in A than in B, which results in a tilting of the wave front towards line $A'B'$.

The sound generated by a turbulent jet can be separated into two parts. These are the sound generated by interaction of turbulence fluctuations and the sheared mean flow and sound generated by turbulence fluctuations interacting with themselves; for more detail see e.g. Ribner (1969). The two sound components are often referred to as *shear noise* and *self noise*, respectively. The *self noise* is radiated equally in all directions whereas the *shear noise* gives a dipole-like contribution. Superimposed, these two contributions give an ellipsoid-shaped sound radiation pattern, with the most sound radiated along the jet axis. Adding the effect of convection, the part of the sound that is radiated downstream of the jet is significantly larger than the part radiated in the upstream direction. Refraction significantly decreases the sound radiated along the jet axis. The contribution to the overall sound from

the two components and the effect of convection and refraction on the pattern of radiated sound are depicted in figure 1.3.

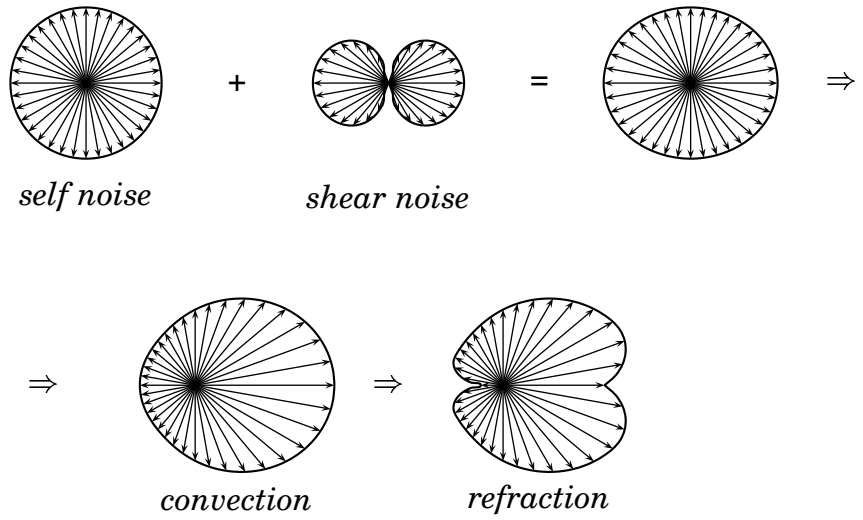

Figure 1.3: Superposition of the noise generated by the turbulence itself, *self noise*, and the noise generated by interaction of the mean shear flow and turbulence, *shear noise*, gives the upper right sound pattern. Convection and refraction affect the pattern of radiated sound, and the result is the directional sound pattern in the lower right figure.

Numerical methods based on computational fluid dynamics (CFD) used for the prediction of flow-induced sound are often referred to as computational aeroacoustics (CAA). Using a grid fine enough in the far-field regions not to introduce sound propagation errors, the sound pressure level can be obtained directly from the flow field simulation. This requires a detailed numerical compressible flow simulation, e.g. direct numerical simulation (DNS), see for example Freund (2001) and Mitchell *et al.* (1999), or large-eddy simulation (LES), as done by for example Bogey *et al.* (2000*a*) and Mankbadi *et al.* (2000).

To save computational time, a hybrid approach may be used in which the computational problem is divided into two parts. A LES or DNS can be used to obtain the non-linear near-field, which in the jet noise case corresponds to the hydrodynamic jet region. Sources of sound obtained from the flow simulation are then propagated to far-field observer locations using either a solver based on the Linearized Euler Equations (LEE), see Billson *et al.* (2002), or an integral method such as Lighthill's acoustic analogy, as done by Bogey *et al.* (2001), or Kirchhoff surface integration, see Freund *et al.* (1996). In DNS, all scales of the turbulent flow field are computed accurately, which requires a mesh

fine enough to capture even the smallest scales of the flow, whereas, in LES, only the large scales of the flow are resolved and the influence on these large scales of the smaller, unresolved scales are modeled using a subgrid scale model. With the computational resources available today, DNS is restricted to fairly simple geometries and low Reynolds number flows. Moreover, it is believed, see Mankbadi (1999), that large scales are more efficient than small ones in generating sound, which justifies the use of LES for sound predictions.

Another approach is to use a less computationally expensive RANS calculation to obtain a time-averaged flow field. Information about length and time scales in the time-averaged flow field can then be used to synthesize turbulence in the noise source regions, see Billson (2002). This method is promising since simulations of high Reynolds number flows are possible with reasonable computational efforts. In contrast to a RANS calculation, where all turbulent scales in the flow are modeled and only a time averaged flow field is obtained, DNS and LES directly provide information about turbulent quantities and sources of noise. To be able to improve existing CFD routines for more reliable results, we need a understanding of noise source mechanisms. Therefore, it is of great importance to perform more detailed calculations, such as DNS or LES, to get a more realistic picture of the flow physics. Detailed information on the statistical character of the flow can later be used to develop prediction techniques based on noise generation mechanisms. This is the main objective of the present work.

1.4 Overview of the Present Study

Large-eddy simulations of a Mach 0.75 nozzle/jet configuration were performed. The Reynolds number based on the nozzle exit diameter and the jet velocity at the nozzle exit plane, Re_D, was 5.0×10^4. The Reynolds number in the measurements by Jordan *et al.* (2002*a*,*b*) and Jordan & Gervais (2003), used for comparison and validation of the simulations, was approximately one million. Such a high Reynolds number probably means that the scales that needs to be resolved are too small. Thus the Reynolds number in our LES was decreased with the assumption that the flow is only weakly Reynolds number dependent. The nozzle used in the simulation corresponds to the last contraction of the nozzle configuration in the experimental setup.

Simulations of the Mach 0.75 jet were performed for two flow conditions: an unheated jet, i.e. a jet where the static temperature in the

nozzle exit plane, T_j, was equal to the static temperature of the ambient air, T_∞, and a heated version where the exhaust temperature was twice that of the surrounding air. The main reason for choosing the Mach 0.75 jet was that experimental data were available for both isothermal and heated conditions. This made it possible to investigate whether heating effects on both the flow field and on radiated sound could be accurately captured with the LES. Furthermore, the temperature ratio used for the heated jet is quite realistic for real jet engines. For validation of the LES results, the time-averaged flow field was compared with experimental data provided by Laboratoire d'Etude Aeródynamiques, Poitiers, France, Jordan *et al.* (2002*a*). Two-point space-time correlations were obtained for a few locations in the shear layer, and integral length and time scales and eddy convection velocities were evaluated. Two-point measurements in the jet shear layer done by Jordan & Gervais (2003) have been used for comparison. Evaluations were made of far-field sound pressure levels using Kirchhoff surface integration and Lighthill's acoustic analogy. Predicted sound pressure levels were compared with levels measured by Jordan *et al.* (2002*b*).

The predicted aerodynamic field and prediction of radiated sound for the two jets will be presented separately in sections 7.1–7.2. The effects of heating will then be discussed in section 7.3.

It is important to state that this work is not an attempt to predict radiated sound using high-order numerical schemes, sophisticated subgrid scales models and a high resolution mesh. Rather it is a test of what a numerical scheme that is state-of-the-art for flow simulations, a standard subgrid scale model and rather coarse mesh give us in terms of flow field and radiated sound.

1.5 Aerodynamic and Acoustic Measurements Used for Validation

The measurements were made by Jordan *et al.* at the MARTEL facility of CEAT (Centre d'Etudes Aeródynamiques et Thermiques), Poiters. Two-component single-point and mono-component two-point measurements were made using Laser Doppler Velocimetry (LDV). The acoustic field was sampled using an arc of microphones at 30 jet diameters and 50 jet diameters from the jet exit, respectively. For more detail on the experimental setup see Jordan *et al.* (2002*a*,*b*); Jordan & Gervais (2003).

Chapter 2

Governing Equations

The compressible form of the continuity, momentum and energy equations where the viscous stress and the heat flux have been defined using Newton's viscosity law and Fourier's heat law, respectively, are often referred to as the Navier-Stokes equations (Panton, 1995):

$$\frac{\partial \rho}{\partial t} + \frac{\partial (\rho u_i)}{\partial x_i} = 0 \tag{2.1}$$

$$\frac{\partial (\rho u_i)}{\partial t} + \frac{\partial (\rho u_i u_j)}{\partial x_j} = -\frac{\partial p}{\partial x_i} + \frac{\partial \sigma_{ij}}{\partial x_j} \tag{2.2}$$

$$\frac{\partial \left(\rho e_0\right)}{\partial t} + \frac{\partial \left(\rho e_0 u_j\right)}{\partial x_j} = -\frac{\partial p u_j}{\partial x_j} + C_p \frac{\partial}{\partial x_j}\left(\left(\frac{\mu}{Pr}\right)\frac{\partial T}{\partial x_j}\right) + \frac{\partial}{\partial x_j}\left(u_i \sigma_{ij}\right) \tag{2.3}$$

σ_{ij} in equations 2.2 and 2.3 is the viscous stress defined by

$$\sigma_{ij} = \mu\left(2S_{ij} - \frac{2}{3}S_{mm}\delta_{ij}\right) \tag{2.4}$$

where S_{ij} is the strain-rate tensor given by

$$S_{ij} = \frac{1}{2}\left(\frac{\partial u_i}{\partial x_j} + \frac{\partial u_j}{\partial x_i}\right) \tag{2.5}$$

In equation 2.3 Pr denotes the Prandtl number.

The system of governing equations, equations 2.1–2.3, is closed by making assumptions concerning the thermodynamics of the gas considered. It is assumed that the gas is a thermally perfect gas, i.e. it obeys the gas law,

$$P = \rho R T \tag{2.6}$$

where R is the gas constant. Furthermore, the gas is assumed to be calorically perfect, which implies that internal energy and enthalpy are linear functions of temperature.

$$\begin{aligned} e &= C_v T \\ h &= C_p T \\ C_v &= C_p - R \end{aligned} \tag{2.7}$$

where C_p is the specific heat at constant pressure. Moreover, the viscosity, μ, is assumed to be constant.

Chapter 3

Large-Eddy Simulation

A large-eddy simulation is a flow simulation in which the large eddies are accurately represented, that is as accurately as possible considering the numerical errors of the solver and the assumptions made. The effect on the large, resolved eddies of those not resolved is modeled using a subgrid scale model. By refining the mesh used, LES approaches DNS, where all scales of the flow should be represented accurately. However, only resolving the larger scales significantly decreases the computational effort needed, making LES more feasible for non-academic flows. The larger eddies are directly affected by the boundary conditions, carry most of the Reynolds stresses and must be computed, whereas the small-scale turbulence is weaker, contributing less to the Reynolds stresses, and is therefore less critical. Moreover, the smaller scales are more nearly isentropic and have nearly universal characteristics and are therefore more amenable to modeling (Wilcox, 1998).

3.1 Spatial Filtering

Some kind of filtering is needed to obtain a velocity field containing only the large-scale components of the total field. The filtered flow field is defined by

$$\overline{\Phi}(\mathbf{x},t) = \int_{\Omega} G(\mathbf{x}-\mathbf{x}';\Delta)\Phi(\mathbf{x}',t)d^3\mathbf{x}' \tag{3.1}$$

where $G(x,x')$, the filter kernel, is a localized function and Δ is the filter width representing the smallest turbulence scales allowed by the filter. This filter width is usually based on the size of the grid cells. The filter function, G, is normalized by requiring that

$$\int_{\Omega} G(\mathbf{x}-\mathbf{x}';\Delta)d^3\mathbf{x}' = 1 \tag{3.2}$$

As the cell size goes to zero, equation 3.1 becomes a Dirac delta sequence, i.e.

$$\lim_{\Delta\to 0}\int_{\Omega} G(\mathbf{x}-\mathbf{x}';\Delta)\Phi(\mathbf{x}',t)d^3\mathbf{x}' = \int_{\Omega}\delta(\mathbf{x}-\mathbf{x}')\Phi(\mathbf{x}',t)d^3\mathbf{x}' = \Phi(\mathbf{x},t) \tag{3.3}$$

The most common filter kernel functions are a box filter in real space or sharp Fourier cut-off filter in wave number space.

Filtering equations 2.1–2.3 results in the flow equations governing the large scales of the flow.

3.1.1 Favre Filtering

Favre filtering is a common approach for compressible flows since it results in governing equations in a convenient form. Moreover, using any other filter approach would lead to more complicated subgrid scale terms. Subgrid scale terms would also appear in the continuity equation. Using Favre filtering, the flow properties are decomposed as follows

$$\Phi = \tilde{\Phi} + \Phi'' \tag{3.4}$$

where $\tilde{\Phi}$ is a Favre-filtered, resolved, quantity and Φ'' is the unresolved part of Φ. The Favre-filtered part of Φ is obtained as follows

$$\tilde{\Phi} = \frac{\overline{\rho\Phi}}{\overline{\rho}} \tag{3.5}$$

In contrast to Favre time averaging

$$\tilde{\Phi} \neq \tilde{\tilde{\Phi}} \tag{3.6}$$

and hence

$$\widetilde{\Phi''} \neq 0 \tag{3.7}$$

The Favre-filtered continuity, momentum and energy equations are obtained by applying the filtering operation, equation 3.5, directly on the governing equations, 2.1–2.3, which implies

$$\frac{\partial\overline{\rho}}{\partial t} + \frac{\partial(\overline{\rho}\tilde{u}_i)}{\partial x_i} = 0 \tag{3.8}$$

$$\frac{\partial(\overline{\rho}\tilde{u}_i)}{\partial t} + \frac{\partial(\overline{\rho}\tilde{u}_i\tilde{u}_j)}{\partial x_j} = -\frac{\partial \overline{p}}{\partial x_i} + \frac{\partial \overline{\sigma}_{ij}}{\partial x_j} + \frac{\partial \tau_{ij}}{\partial x_j} \tag{3.9}$$

$$\begin{aligned}\frac{\partial\left(\overline{\rho}\tilde{e}_0\right)}{\partial t} + \frac{\partial\left(\overline{\rho}\tilde{e}_0\tilde{u}_j\right)}{\partial x_j} &= -\frac{\partial \overline{p}\tilde{u}_j}{\partial x_j} + \\ + \frac{\partial}{\partial x_j}\left(C_p\frac{\mu}{Pr}\frac{\partial \tilde{T}}{\partial x_j} + q_j\right) &+ \frac{\partial}{\partial x_j}\left(\tilde{u}_i\left(\overline{\sigma}_{ij} + \tau_{ij}\right)\right)\end{aligned} \tag{3.10}$$

where $\overline{\sigma}_{ij}$ and τ_{ij} are the Favre-filtered viscous stress tensor and subgrid scale viscous stress tensor, respectively. These are here defined as

$$\overline{\sigma}_{ij} = \mu\left(2\tilde{S}_{ij} - \frac{2}{3}\tilde{S}_{mm}\delta_{ij}\right) \tag{3.11}$$

$$\tau_{ij} = -\overline{\rho}\left(\widetilde{u_i u_j} - \tilde{u}_i\tilde{u}_j\right) \tag{3.12}$$

The subgrid scale stress tensor is a tensor built up of products of resolved and unresolved quantities appearing in the filtering operation.

In equation 3.11, $\tilde{S}_{ij}$ is the Favre-filtered rate of strain tensor given by

$$\tilde{S}_{ij} = \frac{1}{2}\left(\frac{\partial \tilde{u}_i}{\partial x_j} + \frac{\partial \tilde{u}_j}{\partial x_i}\right) \tag{3.13}$$

When filtering the energy equation, a term analogous to the subgrid scale stress term appears in the heat flux term. This subgrid scale heat flux, denoted by q_j in equation 3.10, reads

$$q_j = -C_p\overline{\rho}\left(\widetilde{Tu_j} - \tilde{T}\tilde{u}_j\right) \tag{3.14}$$

3.2 Subgrid Scale Model

The subgrid scale stress and heat flux defined by equations 3.11 and 3.14, respectively, both contain products including unresolved quantities, which have to be modeled. The main purpose of the subgrid scale model is to provide dissipation of the resolved scales, i.e. correctly reproduce the transfer of energy from resolved to unresolved scales.

The simplest subgrid scale models used are so called eddy-viscosity models. These are based on the equilibrium assumption, i.e. small scales have shorter time scales than large, adjust more rapidly to perturbations and reach equilibrium almost instantaneously. Using these

assumptions, the transport equation for the subgrid scale kinetic energy reduces to

$$\varepsilon_\nu = -\tau_{ij}\overline{S}_{ij} \tag{3.15}$$

where ε_ν denotes viscous dissipation. The most famous of these models is the Smagorinsky (1963) model, in which the anisotropic part of the subgrid scale stress is represented as

$$\tau_{ij} - \frac{1}{3}\tau_{mm}\delta_{ij} = -2\nu_t\overline{S}_{ij} \tag{3.16}$$

The eddy-viscosity has the dimension $\left[\frac{m^2}{s}\right]$ and can thus be represented by a length scale, l, representing the subgrid scales and a velocity scale, $\mathcal{U} = \sqrt{\tau_{mm}/\rho}$. If the viscous dissipation is said to be proportional to the length scale and the velocity scale as $\varepsilon_\nu \sim \mathcal{U}^3/l$ and the eddy-viscosity $\nu_t \sim l\mathcal{U}$, inserting this in equations 3.15–3.16 gives $\mathcal{U} \sim l\left|\overline{S}\right|$. Letting $l \sim \Delta$ gives

$$\nu_t = \left(C_s\Delta\right)^2\left|\overline{S}\right| \tag{3.17}$$

where C_s is the Smagorinsky constant.

The subgrid scale model used in this work is the Smagorinsky part of the model proposed by Erlebacher *et al.* (1992) for compressible flows. This model is based on Favre-filtered quantities, and the subgrid stress tensor is modeled as

$$\tau_{ij} = \mu_t\left(2\tilde{S}_{ij} - \frac{2}{3}\tilde{S}_{mm}\delta_{ij}\right) - \frac{2}{3}\overline{\rho}k^{SGS}\delta_{ij} \tag{3.18}$$

where k^{SGS} is the subgrid scale kinetic energy

$$k^{SGS} = C_I\Delta^2\tilde{S}_{mn}\tilde{S}_{mn} \tag{3.19}$$

and μ_t is the subgrid scale kinematic viscosity defined as

$$\mu_t = C_R\overline{\rho}\Delta^2\sqrt{\tilde{S}_{mn}\tilde{S}_{mn}} \tag{3.20}$$

The subgrid heat flux appearing in the Favre-filtered energy equation is modeled using a temperature gradient approach

$$q_j = C_p\frac{\mu_t}{Pr_t}\frac{\partial\tilde{T}}{\partial x_j} \tag{3.21}$$

The filter width used in equations 3.19 and 3.20 is the local grid cell width, i.e. $\Delta = \left(\Delta_1\Delta_2\Delta_3\right)^{1/3}$.

The Smagorinsky model constants C_R and C_I were proposed by Erlebacher *et al.* (1992) to be

$$\begin{cases} C_R &= 0.12 \\ C_I &= 0.66 \end{cases} \tag{3.22}$$

and these are the values used in this study. No work has been done thus far to investigate the effect of the subgrid scale model used on the predicted flow field.

Chapter 4

Sound Propagation

Since the compressible Navier-Stokes equations include all information on the acoustic field, solving them directly gives information about the sound pressure levels in observers locations in the far-field regions. However, such an approach is very expensive as concerns the necessary calculation efforts. It is more common to use some kind of hybrid approach where the problem is divided into two parts, i.e. obtaining the instantaneous near-field using a Navier-Stokes solver and then obtaining the far-field sound either by the use of an integral approach or by solving a set of equations, e.g. the Linear Euler Equations (LEE), with source terms obtained from the instantaneous flow field. Figure 4.1 shows different methods. The method used in this thesis is indicated with dashed lines.

4.1 Lighthill's Acoustic Analogy

Rewriting the full Navier-Stokes equations gives a scalar equation for an acoustic variable with a wave operator on the left-hand side. The sound pressure level in a far-field observer location can be estimated by integration over a volume containing all sound-generating sources. It is important to note that no interaction between the propagating sound wave and the flow field in which it is propagating is considered outside the integration volume, i.e. no refraction is taken into account and therefore all non-linearities have to be included in the integration volume.

Sir James Lighthill's introduction of his acoustic analogy, i.e. the analogy between the full non-linear flow and the linear theory of acoustics, is often referred to as the start of aeroacoustics. By combining the time derivative of the continuity equation and the divergence of the momen-

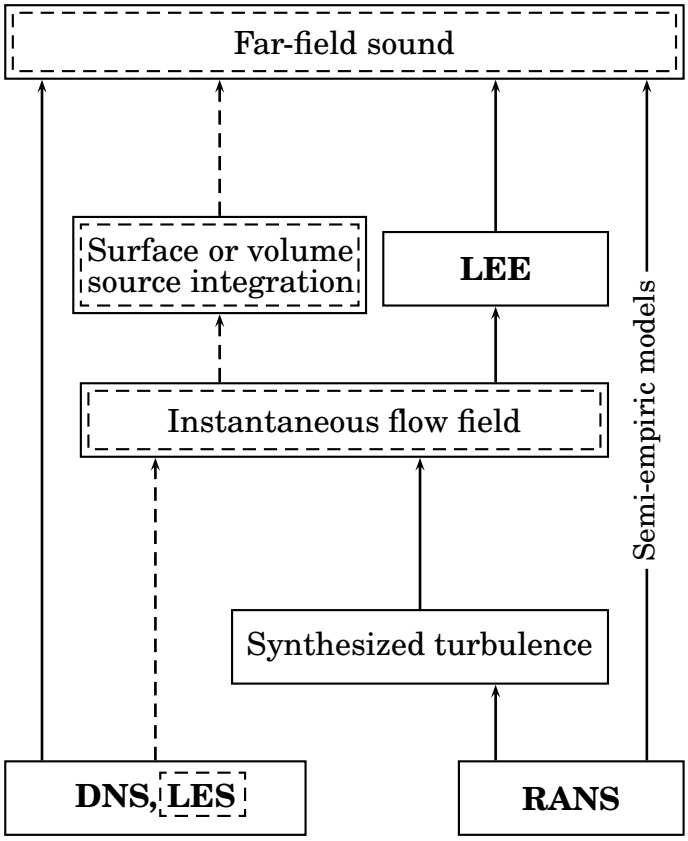

Figure 4.1: Computational aeroacoustic methods. Different approaches for obtaining acoustic pressure signals in far-field observer locations are shown. The methodology used in this work is indicated with dashed lines.

tum equation, the flow equations may be rewritten in a wave operator form, Lighthill (1952).

$$\frac{\partial^2 \rho}{\partial t^2} = \frac{\partial^2}{\partial x_i \partial x_j} \left(\rho u_i u_j + p\delta_{ij} - \sigma_{ij} \right) \tag{4.1}$$

By subtracting $c_\infty^2 \frac{\partial^2 \rho}{\partial {x_i}^2}$ on each side, equation 4.1 may be rewritten as

$$\frac{\partial^2 \rho}{\partial t^2} - c_\infty^2 \frac{\partial^2 \rho}{\partial {x_i}^2} = \frac{\partial^2 T_{ij}}{\partial x_i \partial x_j} \tag{4.2}$$

which is the famous Lighthill's equation. In equation 4.2, T_{ij} is the Lighthill stress tensor, defined by

$$T_{ij} = \rho u_i u_j + \left(p - \rho c_\infty^2 \right) \delta_{ij} - \sigma_{ij} \tag{4.3}$$

In unheated subsonic flows at high Reynolds number, the Reynolds stress is the dominating term in equation 4.3, and thus the Lighthill tensor may be reduced to $T_{ij} \simeq \rho u_i u_j$ (Lighthill, 1952). It has been confirmed by Colonius & Freund (2000) that the viscous part, σ_{ij}, contributes little to the far-field sound. The entropic part, $(p - \rho c_\infty^2)$, however, has been shown by Freund (2003) to give a non-negligible contribution. An analytic solution to equation 4.2 can be obtained by use of the free-space Green's function

$$G(\mathbf{x}, t) = \frac{1}{4\pi c_\infty^2 r} \delta(\tau_r) \tag{4.4}$$

which gives

$$\rho(\mathbf{x}, t) - \rho_\infty = \frac{1}{4\pi c_\infty^2} \int_V \frac{1}{r} \frac{\partial^2 T_{ij}}{\partial y_i \partial y_j} (\mathbf{y}, \tau_r) \, dV(\mathbf{y}) \tag{4.5}$$

where $\mathbf{x}$ is a observer location in the far-field and $\mathbf{y}$ is the source location. τ_r denotes retarded time and is related to the observer evaluation time, t, as

$$\tau_r = t - \frac{r}{c_\infty} \tag{4.6}$$

where $r = |\mathbf{x} - \mathbf{y}|$ is the distance between a source location and an observer and c_∞ is the speed of sound in the far-field region. More detailed discussions can be found in for example Lighthill (1952) and Larsson (2002). A more often used version of equation 4.5 is one where the second-order spatial derivatives have been converted to temporal ones. According to Larsson (2002) and Larsson *et al.* (2003), this conversion can be accomplished using the following relation

$$\frac{\partial T_{ij}(\tau_r)}{\partial x_i} = \frac{\partial T_{ij}(\tau_r)}{\partial \tau_r} \frac{\partial \tau_r}{\partial x_i} = -\frac{1}{c_\infty} \frac{\partial r}{\partial x_i} \frac{\partial T_{ij}(\tau_r)}{\partial \tau_r} \tag{4.7}$$

where

$$\begin{aligned} \frac{\partial r}{\partial x_i} &= \frac{\partial \left[(x_j - y_j)(x_j - y_j) \right]^{1/2}}{\partial x_i} \\ &= \frac{(x_i - y_i)}{\left[(x_j - y_j)(x_j - y_j) \right]^{1/2}} = \frac{r_i}{r} \end{aligned} \tag{4.8}$$

which implies

$$\rho(\mathbf{x}, t) - \rho_\infty \approx \frac{1}{4\pi c_\infty^4} \int_V \frac{r_i r_j}{r^3} \frac{\partial^2 T_{ij}}{\partial t^2} (\mathbf{y}, \tau_r) \, dV(\mathbf{y}) \tag{4.9}$$

The left-hand side in equations 4.5 and 4.9 is a far-field density fluctuation

$$\rho'(\mathbf{x},t) = \rho(\mathbf{x},t) - \rho_\infty \tag{4.10}$$

which is related to the pressure fluctuation as

$$p'(\mathbf{x},t) = \rho'(\mathbf{x},t)\, c_\infty^2 \tag{4.11}$$

assuming that the acoustic compression-expansion processes in the flow are adiabatic.

4.2 Kirchhoff Surface Integration

Kirchhoff integration is a method for predicting the value of a property, Φ, governed by the wave equation in a point outside a surface enclosing all generating structures (Lyrintzis, 1994). The method was originally used in the theory of diffraction of light and in other problems of an electromagnetic nature but has recently been used extensively for aeroacoustic applications.

$$\Phi(\mathbf{x},t) = \frac{1}{4\pi}\int_S \left[\frac{\Phi}{r^2}\frac{\partial r}{\partial n} - \frac{1}{r}\frac{\partial \Phi}{\partial n} + \frac{1}{c_\infty r}\frac{\partial r}{\partial n}\frac{\partial \Phi}{\partial t}\right]_{\tau_r} dS(\mathbf{y}) \tag{4.12}$$

τ_r denotes that the expression within brackets is to be evaluated at retarded time, i.e. emission time. τ_r is related to the observer evaluation time by the distance from the surface to the observer and the speed of sound in the observer location, see equation 4.6. c_∞ is again the speed of sound in the far-field region. The variable, Φ, to be evaluated is in this case the surface pressure. S denotes the surface enclosing all sound generating structures and n denotes the direction normal to the surface. The surface, S, must be placed in a region where the flow is completely governed by a homogeneous linear wave equation with constant coefficients, (Freund *et al.*, 1996). More detail on the Kirchhoff surface integration method can be found in e.g. Freund *et al.* (1996) and Lyrintzis (1994).

Since the hydrodynamic source region decays slowly downstream, it is not possible to use a surface enclosing the entire source region without entering this non-linear region, see figure 4.2. It is thus common practice to use Kirchhoff surfaces not closed in the upstream and downstream ends. It was shown by Freund *et al.* (1996) that the errors introduced by using such surfaces are small if the main portion of the

sound sources are within the axial extent of the surface and if lines connecting observer locations with locations in the hydrodynamic region, representing the main sources of sound, intersect with the surface.

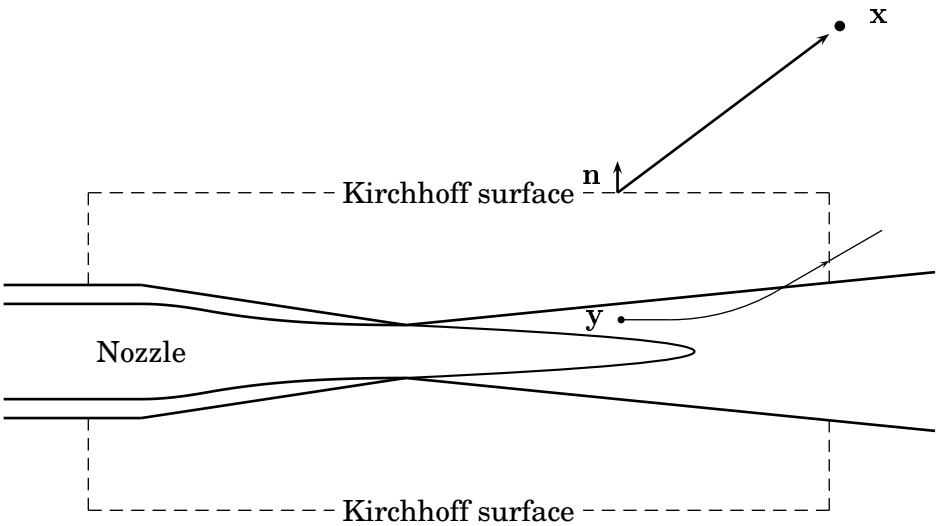

Figure 4.2: The Kirchhoff surface does not intersect with the hydrodynamic jet region. Sound generated in the shear layer, y, is propagated in the solver and extracted from the Kirchhoff surface to the far-field observer, x.

In this work a Kirchhoff surface closed in the upstream end and open in the downstream end was used, see figure 4.3.

The Kirchhoff surface integral method is less computationally expensive and storage demanding than Lighthill's acoustic analogy since only surface data must be stored and evaluated. Moreover, the integrand includes only first-order derivatives, whereas the integrand in Lighthill's acoustic analogy contains second-order derivatives in time or space.

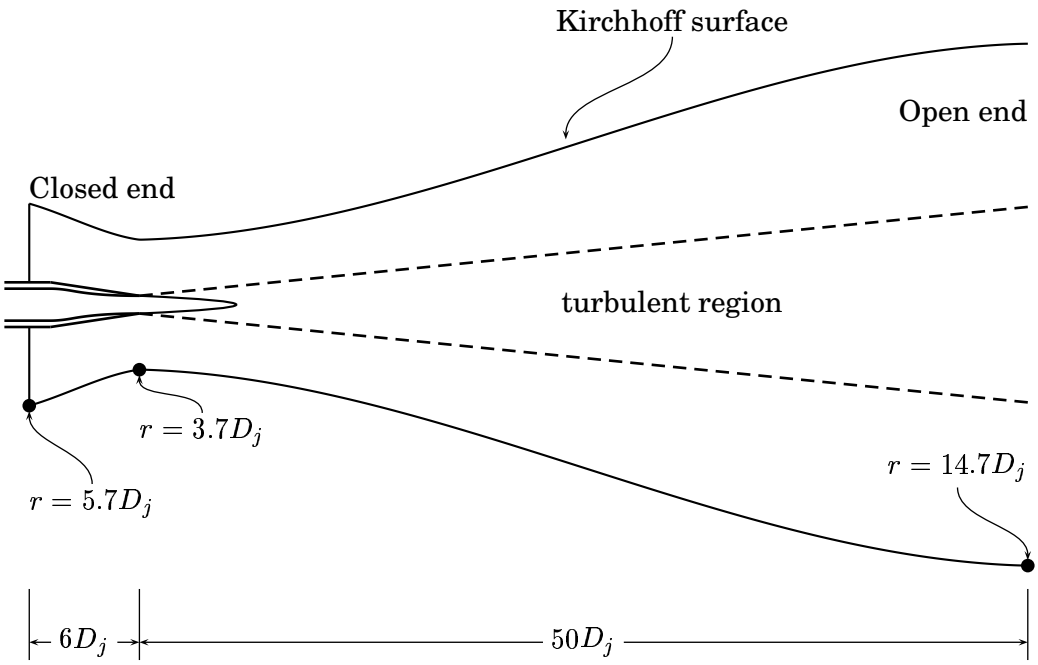

Figure 4.3: Kirchhoff surface with closed upstream end and open downstream end.

Chapter 5

Numerical Method

The code used for the large-eddy simulations is one of the codes in the G3D family of finite volume method, block structured codes developed by Eriksson (1995). To enhance calculation performance and enable the use of a large number of cells, routines for parallel computations have been introduced in the code. These routines are based on the MPI[1] libraries.

This chapter gives an overview of the numerical scheme and boundary conditions used. More detail on these subjects can be found in Eriksson (1995) and Eriksson (2003).

For convenience, the Favre-filtered Navier-Stokes equations 3.8–3.10 are written in a more compact form:

$$\frac{\partial Q}{\partial t} + \frac{\partial \mathcal{F}_j}{\partial x_j} = 0 \tag{5.1}$$

where

$$Q = \begin{bmatrix} \overline{\rho} \\ \overline{\rho}\tilde{u}_i \\ \overline{\rho}\tilde{e}_0 \end{bmatrix} \tag{5.2}$$

and

$$\mathcal{F}_j = \begin{bmatrix} \overline{\rho}\tilde{u}_j \\ \overline{\rho}\tilde{u}_i\tilde{u}_j + \overline{p}\delta_{ij} - \overline{\sigma}_{ij} - \tau_{ij} \\ \overline{\rho}\tilde{e}_0\tilde{u}_j + \overline{p}\tilde{u}_j - C_p\left(\left(\frac{\mu}{Pr} + \frac{\mu_t}{Pr_t}\right)\frac{\partial \tilde{T}}{\partial x_j}\right) - \tilde{u}_i\left(\overline{\sigma}_{ij} + \tau_{ij}\right) \end{bmatrix} \tag{5.3}$$

[1] Message Passing Interface

The stress tensors, $\overline{\sigma}_{ij}$ and τ_{ij}, in equation 5.3 are defined by equation 3.11 and equation 3.18, respectively. Equation 5.1 is discretized on a structured non-orthogonal boundary fitted mesh. Integrating equation 5.1 over an arbitrary volume Ω gives

$$\int_\Omega \frac{\partial Q}{\partial t} dV + \int_\Omega \frac{\partial \mathcal{F}_j}{\partial x_j} dV = 0 \tag{5.4}$$

Using Gauss theorem to rewrite the second volume integral to a surface integral and introducing $\mathbf{Q}$ as the cell average of Q over Ω implies

$$\frac{\partial \mathbf{Q}}{\partial t} V + \int_{\partial\Omega} \mathcal{F}_j \cdot d\mathcal{S}_j = 0 \tag{5.5}$$

In equation 5.5, $\mathcal{S}_j = n_j \mathcal{S}$ is the face area normal vector, i.e. an area with direction. The integral of the fluxes is approximated using the area of cell faces and the face average flux

$$\int_{\partial\Omega} \mathcal{F}_j \cdot d\mathcal{S}_j = \sum_{i=1}^{allfaces} \mathcal{F}_j^i \cdot \mathcal{S}_j^i \tag{5.6}$$

Equation 5.4 can now be rewritten as

$$\frac{\partial \mathbf{Q}}{\partial t} V + \sum_{i=1}^{allfaces} \mathcal{F}_j^i \cdot \mathcal{S}_j^i = 0 \tag{5.7}$$

The total flux, $\mathcal{F}_j$, is divided into a convective part and a diffusive part in the following way:

$$\mathcal{F}_j = \begin{bmatrix} \overline{\rho}\tilde{u}_j \\ \overline{\rho}\tilde{u}_i\tilde{u}_j + \overline{p}\delta_{ij} \\ \overline{\rho}\tilde{e}_0\tilde{u}_j + \overline{p}\tilde{u}_j \end{bmatrix} + \begin{bmatrix} 0 \\ -\overline{\sigma}_{ij} - \tau_{ij} \\ -C_p\left(\left(\frac{\mu}{Pr} + \frac{\mu_t}{Pr_t}\right)\frac{\partial \tilde{T}}{\partial x_j}\right) - \tilde{u}_i\left(\overline{\sigma}_{ij} + \tau_{ij}\right) \end{bmatrix} \tag{5.8}$$

where the first part is the convective, inviscid part and the second the diffusive, viscous part.

5.1 Spatial Discretization

5.1.1 Convective Fluxes

The convective flux across a given cell face is calculated with a user-defined upwind scheme based on the propagation direction of the characteristic variables at the cell face. In this work, a low-dissipative third order upwind scheme has been used. The analysis of characteristic

variables is performed using the solution variables on primitive form, q, which can be estimated from the variables on conservative form with second-order accuracy.

$$q = \begin{bmatrix} \overline{\rho} \\ \tilde{u}_i \\ \overline{p} \end{bmatrix} \tag{5.9}$$

Linearizing the governing equations written on primitive form around a point located on the cell face and considering only plane waves parallel to the cell face gives a one-dimensional system of hyperbolic equations. This equation system can be decoupled by transformation to characteristic variables, see Appendix A. Estimates of the characteristic speeds are computed using face values of the state vector obtained as averages of the values in the neighboring cells, equation 5.10.

$$q^A = \frac{1}{2}\left(\mathbf{q}_2 + \mathbf{q}_3\right) \tag{5.10}$$

Superscript A in equation 5.10 denotes average and subscript 2, and 3 denotes the cells on each side of the face, see figure 5.1.

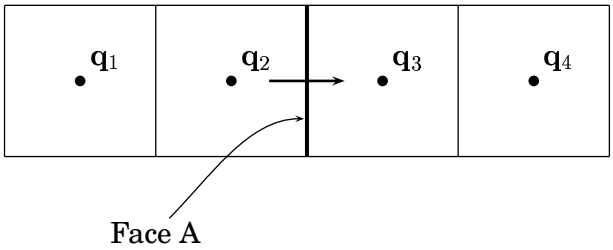

Figure 5.1: Two cells on each side of face A are needed to obtain an estimate of the flux across the face.

Using the cell face values in equation 5.10, the characteristic speeds are obtained as

$$\begin{aligned} \lambda_1 &= u_i^A \mathcal{S}_i \\ \lambda_2 &= \lambda_1 \\ \lambda_3 &= \lambda_1 \\ \lambda_4 &= \lambda_1 + c^A\sqrt{\mathcal{S}_i\mathcal{S}_i} \\ \lambda_5 &= \lambda_1 - c^A\sqrt{\mathcal{S}_i\mathcal{S}_i} \end{aligned} \tag{5.11}$$

The characteristic variables on the face are obtained using upwinded face values of the primitive variables. Two versions of q on the cell

face are calculated, one obtained by upwinding from the left and one obtained by upwinding from the right

$$\begin{aligned} q^L &= C_1\mathbf{q}_1 + C_2\mathbf{q}_2 + C_3\mathbf{q}_3 + C_4\mathbf{q}_4 \\ q^R &= C_4\mathbf{q}_1 + C_3\mathbf{q}_2 + C_2\mathbf{q}_3 + C_1\mathbf{q}_4 \end{aligned} \tag{5.12}$$

where superscripts L and R denote left and right, respectively. C_1,C_2,C_3 and C_4 are constants defining the upwinding scheme for a four-point stencil. These are defined as

$$(C_1, C_2, C_3, C_4) = \left(\frac{-1}{12} - \varepsilon, \frac{7}{12} + 3\varepsilon, \frac{7}{12} - 3\varepsilon, \frac{-1}{12} + \varepsilon\right) \tag{5.13}$$

Inserting $\varepsilon = \frac{1}{96}$ in equation 5.13 gives the third-order low dissipative scheme used in this work. The sign of the characteristic speeds tells us the direction in which local waves in the vicinity of the cell face are traveling in relation to the cell face normal vector. Each of the five characteristic variables are calculated using state vector values upwinded in the direction of the corresponding characteristic speed, i.e. either the left upwinded version of q or the right upwinded version is used. The characteristic variables are obtained as follows

$$\begin{aligned} W_1 &= \rho^{L,R} - \frac{p^{L,R}}{\left(c^A\right)^2} \\ W_2 &= \frac{\mathcal{S}_1 u_2^{L,R} - \mathcal{S}_2 u_1^{L,R}}{\sqrt{\mathcal{S}_1\mathcal{S}_1 + \mathcal{S}_2\mathcal{S}_2}} \\ W_3 &= \frac{1}{\sqrt{\mathcal{S}_i\mathcal{S}_i}}\left[\sqrt{\mathcal{S}_1\mathcal{S}_1 + \mathcal{S}_2\mathcal{S}_2}u_3^{L,R} - \mathcal{S}_3\left(\frac{\mathcal{S}_1 u_1^{L,R} + \mathcal{S}_2 u_2^{L,R}}{\sqrt{\mathcal{S}_1\mathcal{S}_1 + \mathcal{S}_2\mathcal{S}_2}}\right)\right] \\ W_4 &= \frac{1}{2}\left[\frac{\rho^A}{c^A}\frac{\mathcal{S}_i u_i^{L,R}}{\sqrt{\mathcal{S}_j\mathcal{S}_j}} + \frac{p^{L,R}}{\left(c^A\right)^2}\right] \\ W_5 &= \frac{1}{2}\left[\frac{-\rho^A}{c^A}\frac{\mathcal{S}_i u_i^{L,R}}{\sqrt{\mathcal{S}_j\mathcal{S}_j}} + \frac{p^{L,R}}{\left(c^A\right)^2}\right] \end{aligned} \tag{5.14}$$

where again superscripts L and R denote left and right, respectively. The characteristic variables are then transformed back to solution variables on primitive form using equation 5.15. The convective flux over the cell face can then be estimated by inserting the face values obtained into the inviscid part of equation 5.8.

$$
\begin{aligned}
\rho &= W_1 + W_2 + W_3 \\
u_1 &= \frac{-\mathcal{S}_2 W_2}{\sqrt{\mathcal{S}_1\mathcal{S}_1 + \mathcal{S}_2\mathcal{S}_2}} - \frac{\mathcal{S}_1}{\sqrt{\mathcal{S}_j\mathcal{S}_j}}\left[\frac{\mathcal{S}_3 W_3}{\sqrt{\mathcal{S}_1\mathcal{S}_1 + \mathcal{S}_2\mathcal{S}_2}} - \frac{c^A}{\rho^A}\left(W_4 + W_5\right)\right] \\
u_2 &= \frac{\mathcal{S}_2 W_2}{\sqrt{\mathcal{S}_1\mathcal{S}_1 + \mathcal{S}_2\mathcal{S}_2}} - \frac{\mathcal{S}_1}{\sqrt{\mathcal{S}_j\mathcal{S}_j}}\left[\frac{\mathcal{S}_3 W_3}{\sqrt{\mathcal{S}_1\mathcal{S}_1 + \mathcal{S}_2\mathcal{S}_2}} - \frac{c^A}{\rho^A}\left(W_4 + W_5\right)\right] \\
u_3 &= \frac{1}{\sqrt{\mathcal{S}_j\mathcal{S}_j}}\left[\frac{W_3}{\sqrt{\mathcal{S}_1\mathcal{S}_1 + \mathcal{S}_2\mathcal{S}_2}} + \frac{\mathcal{S}_3 c^A}{\rho^A}\left(W_4 + W_5\right)\right] \\
p &= \left(c^A\right)^2\left(W_4 + W_5\right)
\end{aligned}
\tag{5.15}
$$

5.1.2 Diffusive Fluxes

For the viscous fluxes estimates of spatial derivatives of the primitive variables on the cell face, is needed. Derivatives of the primitive variables in computational space are obtained using a centered difference approach. These derivatives are then translated to derivatives in physical space using a chain rule relation given by

$$
\frac{\partial \mathbf{q}}{\partial x_i} = \frac{\partial \xi_j}{\partial x_i}\frac{\partial \mathbf{q}}{\partial \xi_j} \tag{5.16}
$$

where ξ_i denotes the coordinates in computational space. This procedure is described in more detail in Appendix B. The derivatives in computational space are calculated as follows

$$
\begin{aligned}
\frac{\partial \mathbf{q}}{\partial \xi_1} &= \mathbf{q}_{i+1,j,k} - \mathbf{q}_{i,j,k} \\
\frac{\partial \mathbf{q}}{\partial \xi_2} &= \frac{1}{4}\left(\mathbf{q}_{i,j+1,k} - \mathbf{q}_{i,j-1,k}\right) + \frac{1}{4}\left(\mathbf{q}_{i+1,j+1,k} - \mathbf{q}_{i+1,j-1,k}\right) \\
\frac{\partial \mathbf{q}}{\partial \xi_3} &= \frac{1}{4}\left(\mathbf{q}_{i,j,k+1} - \mathbf{q}_{i,j,k-1}\right) + \frac{1}{4}\left(\mathbf{q}_{i+1,j,k+1} - \mathbf{q}_{i+1,j,k-1}\right)
\end{aligned}
\tag{5.17}
$$

where again ξ_i represents the coordinates in computational space and subscripts i, j and k denote the cell index in three directions, see figure 5.2. Using these estimates of spatial derivatives, the viscous flux contribution may be calculated using the diffusive part of equation 5.8.

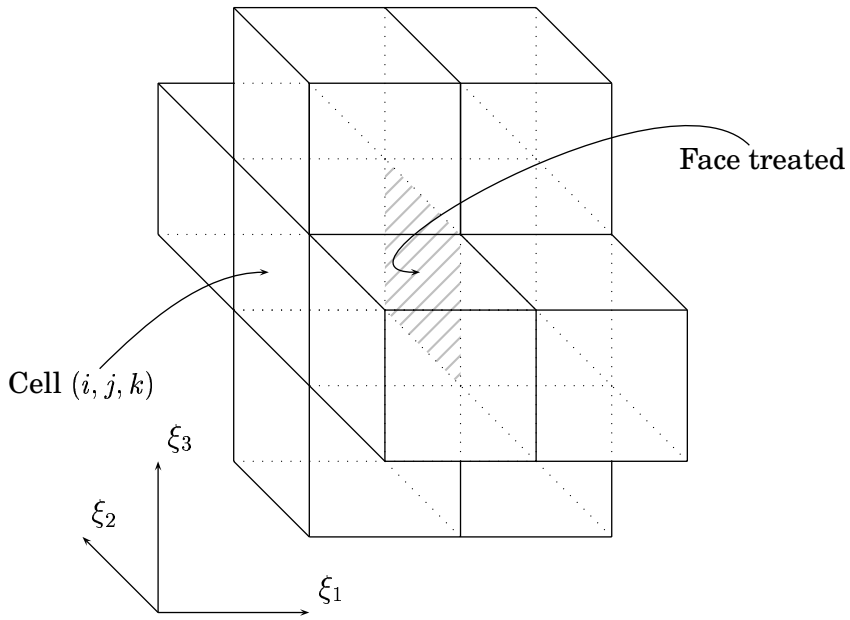

Figure 5.2: Spatial derivatives on a cell face in computational space are estimated using ten neighboring cells.

5.2 Time Marching

A three-stage Runge-Kutta method is used to march the solution in time. When all convective flux and diffusive flux contributions have been calculated as described in the previous sections, the temporal derivative of the flow variables in a certain cell can be estimated as the net flux, i.e.

$$\frac{\partial \mathbf{Q}^n}{\partial t} = \mathcal{F}^n \tag{5.18}$$

The time marching is done in three stages by calculating the state vector, $\mathbf{Q}$, for two intermediate sub-time steps. The time marching algorithm is as follows

$$\begin{aligned} \mathbf{Q}^* &= \mathbf{Q}^n + \Delta t\ \mathcal{F}^n \\ \mathbf{Q}^{**} &= \frac{1}{2}\left[\mathbf{Q}^n + \mathbf{Q}^* + \Delta t\ \mathcal{F}^*\right] \\ \mathbf{Q}^{n+1} &= \frac{1}{2}\left[\mathbf{Q}^n + \mathbf{Q}^* + \Delta t\ \mathcal{F}^{**}\right] \end{aligned} \tag{5.19}$$

where superscript n denotes the previous time step and $n+1$ the next time step. Superscript $*$ and $**$ denotes sub time steps. Δt is the time step, i.e. the time between stage n and $n+1$.

5.3 Boundary Conditions

At the inlet of the nozzle, the nozzle plenum, total pressure and total enthalpy are specified. All free boundaries, i.e. upstream and entrainment boundaries, are defined using absorbing boundary conditions based on characteristic variables. Static pressure is specified at the domain outlet. Figure 5.3 shows the main boundary condition locations.

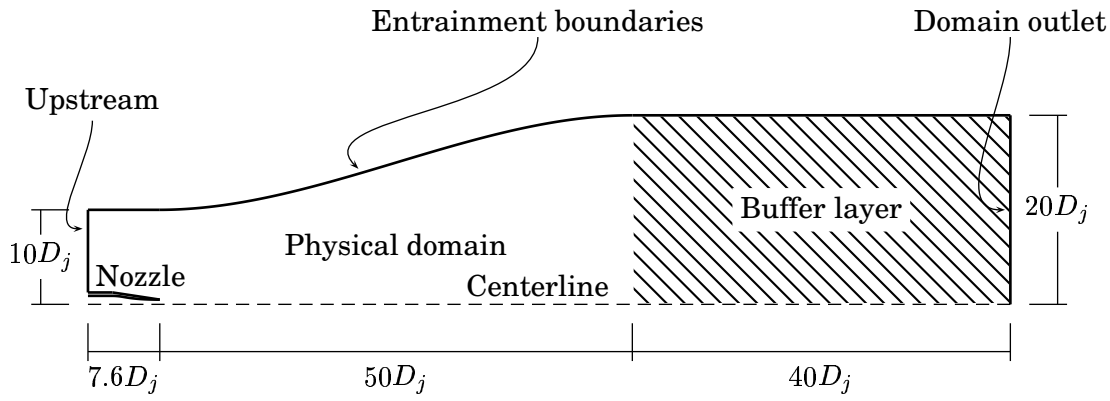

Figure 5.3: Computational setup

5.3.1 Method of Characteristics

A well-posed, non-reflecting, zero-order boundary condition may be specified by analyzing the behavior of local planer waves in the vicinity of the boundary. Close to the boundary, all planar waves can be described by the five characteristic variables, see Appendix A. These five characteristic variables are interpreted physically as one entropy wave, two vorticity waves and two acoustic waves. By obtaining the characteristic speed corresponding to each of the characteristic variables, a well-posed inflow/outflow condition can be specified. The sign of a characteristic speed indicates the direction in which information is transported over the boundary. Negative speed means that information is traveling into the domain and information about the exterior state has to

be specified for the corresponding characteristic variable. A positive sign for the characteristic speed indicates that information is traveling through the boundary out from the domain, which means that exterior information can not be specified but must be extrapolated from the interior.

For outgoing waves to be totally absorbed, i.e. no reflection of the wave at the boundary, the transport direction has to be totally aligned with the direction of analysis, i.e. usually aligned with the boundary normal vector. A wave reaching the boundary with an incident angle of transport will be partly reflected by the boundary, see figure 5.4.

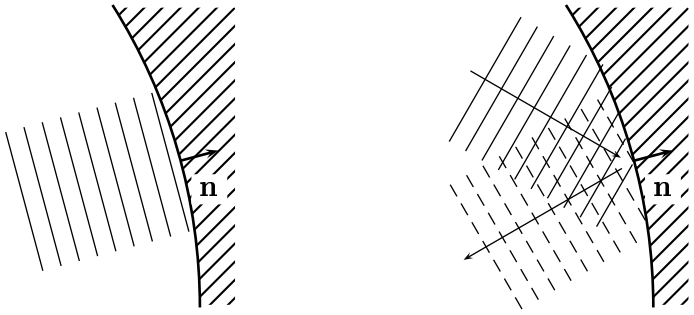

Figure 5.4: A plane wave reaching the boundary with the transport direction aligned with the surface normal is perfectly absorbed (left) whereas a wave not aligned will be partly reflected (right).

5.3.2 Special Treatment of Outlet Boundaries

Defining proper boundary conditions is an issue of great importance, especially in aeroacoustic applications, since acoustic pressure fluctuations are small and spurious waves generated at the boundaries might contaminate the acoustic field. Definitions of boundary conditions for free shear flows are particularly difficult since there are, by definition, no bounding surfaces. The difficulties in defining boundary conditions for free shear flows have been discussed in several publications (e.g. Colonius *et al.*, 1993; Bogey *et al.*, 2000*b*; Mankbadi *et al.*, 2000; Rembold *et al.*, 2002).

At a finite distance downstream the jet, boundary conditions that mimic the jet behavior at infinity are to be specified. Energetic vorticity and

entropy waves traveling out of the domain reaching the outlet boundary will, if not damped out, generate strong acoustic waves traveling back into the domain. These acoustic reflections can be diminished by in some way decreasing the amplitude of fluctuations of vorticity and entropy waves approaching the boundary. Inward traveling acoustic waves may still be generated but will be weaker than for a boundary where no special treatment of the boundary region is utilized. Moreover, these weaker acoustic waves are additionally damped when traveling through the outlet region on their way back into the calculation domain and, hopefully, the waves are so weak when reaching the jet region that they do not affect the results. Therefore, an extra outlet zone has been added to the calculation domain, figure 5.3, where a damping term defined by

$$\varepsilon \left(Q - \langle Q \rangle \right) \tag{5.20}$$

has been added to the equation system. ε is defined by a constant, ε_{max}, and the axial location, x, in the damping zone as

$$\varepsilon = \varepsilon_{max} \left(\frac{x - x_{min}}{x_{max} - x_{min}} \right)^2 \tag{5.21}$$

In equation 5.20, Q represents the flow variables and the time average of Q is calculated as

$$\langle Q \rangle = \frac{\sum_{i=1}^{n} Q_i t_i}{\sum_{i=1}^{n} t_i} \tag{5.22}$$

where subscript i denotes time step. The weighted time average defined by equation 5.22 gives the recent flow property values higher weight than older values but at the same time gives a good estimate of the time-averaged flow field. The fluctuations of the flow field are damped in the boundary zone by forcing the flow properties towards the time-averaged flow field. Furthermore, the cells in this part of the calculation domain are more stretched than cells in the physical part of the calculation domain, which increases the numerical dissipation and thereby further damps flow field fluctuations. The boundary zone consists of roughly 5.0×10^5 cells, which is about 14% of the total calculation domain, and has an axial extent of two meters, see figure 5.3.

5.3.3 Entrainment Boundaries

The entrainment boundaries proved to be rather troublesome as well. The problem is to get enough fluid entrainment into the domain. The effect of not getting the entrained mass flow correct is that a deficit of mass is compensated with an inflow of fluid from the domain outlet. This back flow results in a recirculation zone surrounding the jet

and prevents it from spreading. Approximate values of the velocities specified at the entrainment boundaries were obtained from RANS calculations (Eriksson, 2002) with $U_\infty = 0$. These RANS calculations were performed using a significantly larger calculation domain than in the LES and therefore give reliable information on the entrainment effect at the boundary of the LES domain, see figure 5.5. Furthermore, these RANS calculations have been extensively validated against experimental data (Jordan *et al.*, 2002*a*). Two RANS flow fields have been used, one for the unheated jet and one for the heated.

The fact that the boundary values at the entrainment boundaries have been obtained from RANS results does, to a certain degree, determine the time-averaged flow field. However, since this work is not an attempt to prove that large-eddy simulation predicts the flow of a jet properly but rather to obtain a database of flow properties for jets and to get input for calculations of the acoustic field, this is no severe disadvantage.

5.4 Implementation of Sound Propagation Techniques

5.4.1 Source Term Evaluation

Fourth-order accurate derivatives were used for evaluation of the temporal derivatives in both the Kirchhoff surface integration and in Lighthill's acoustic analogy. Spatial derivatives were evaluated using second-order accurate derivatives. Damping functions were applied to the Lighthill source volume in order to diminish cut-off effects at the volume boundaries. The surface of the Lighthill source volume coincides with the Kirchhoff surface, see figure 4.3.

5.4.2 Retarded Time

Evaluation at retarded time of the integrals is utilized in both the implementation of Kirchhoff surface integration and Lighthill volume integration. The relation between the observer time, t, and retarded time, τ_r, is defined in equation 4.6. The concept of retarded time evaluation is shown in figure 5.6. The upper row of cells in the figure represents the observer pressure signal and the others the history of sound sources for four surface or volume elements. Each cell denotes an instant in time. The lower of these four sources is located farthest away

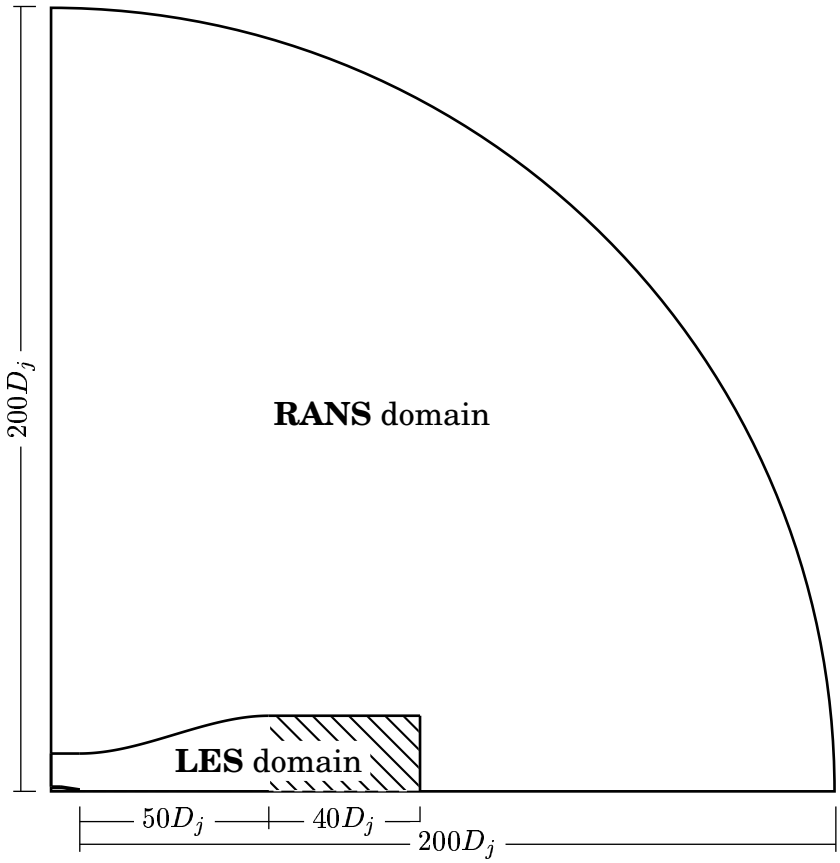

Figure 5.5: Computational domain used for the LES and RANS respectively. The RANS domain is sufficiently large to ensure that no disturbances caused by the outlet boundary have reached the location of the LES boundaries when a converged RANS solution has been obtained.

from the observer. This is the source location, which will define the starting point of the observer pressure signal. The first observer pressure sample that gets a contribution from the source location farthest away from the observer will be the first complete sample. Cells marked with a black point do not contribute to the observer pressure signal. In the same way, the source location closest to the observer defines the temporal extent of the complete pressure signal since this source will give the last contribution to the signal, see figure 5.6. The cells filled with gray indicate the time steps for which data have to be stored in the solver. Five time steps are needed since fourth-order temporal derivatives are used. This means that the source derivatives are evaluated two increments in time from the current solver time. The acoustic source terms do not have to be evaluated each time step and thus each time cell represents a mean of a number of solver time steps. In the results presented in chapters 7.1.6 and 7.2.7, acoustic source terms have

been evaluated every tenth time step. This means that each time cell in figure 5.6, in this case, represents an average over ten time steps. The observer pressure signal is composed of a number of pressure samples separated in time by a predefined time increment. The arrival time of sound waves generated in the turbulent region is defined by the generation time and the distance to the observer. It is most unlikely that the arrival time will match the predefined discrete instants representing the pressure signal. Thus each surface or volume element contributes to the pressure signal at two discrete times in the observer pressure signal, i.e. the two instants in time closest to the arrival time. The contribution to each of these is obtained by interpolation.

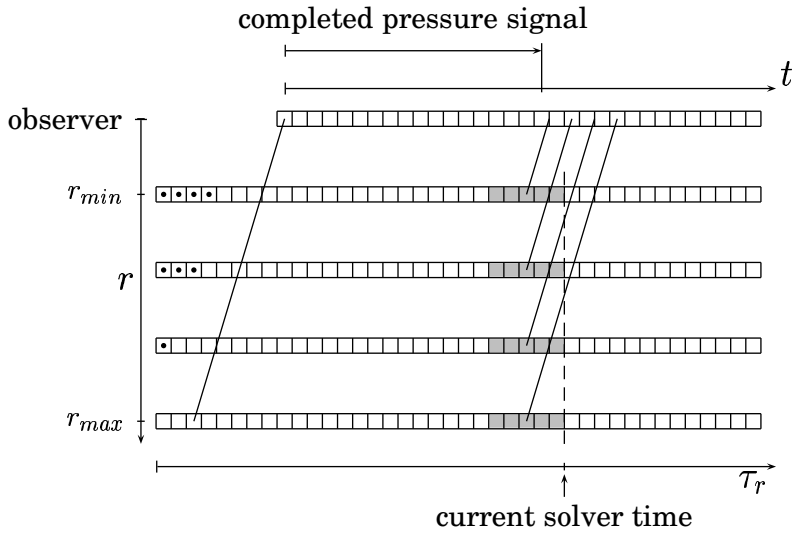

Figure 5.6: The upper row of cells represents the observer pressure signal and the lower ones the time series of sound source parameters for four surface or volume elements. τ_r denotes retarded time.

Chapter 6

Computational Setup

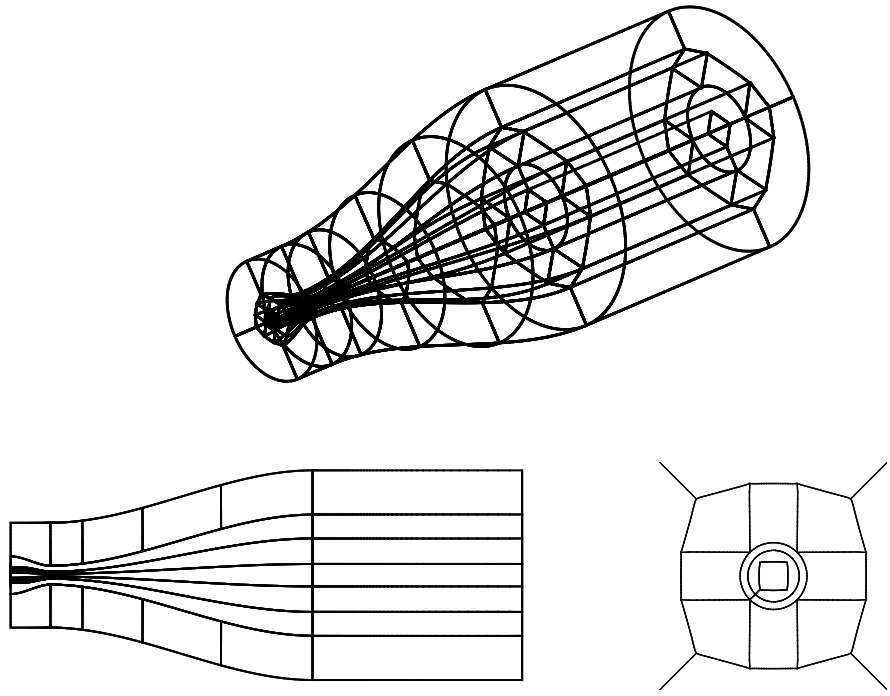

Figure 6.1: The upper figure shows all block boundaries in the domain. The lower left figure shows block boundaries in an xz-plane and the lower right block boundaries in a yz-plane located at the nozzle lip.

6.1 Computational Domain

The computational domain consists of a boundary-fitted block structured mesh with 50 blocks and a total of about 3.0×10^6 cells, fig-

ures 6.1–6.4. The grid cells are concentrated to the shear layer area. To establish mesh homogeneity, a combination of polar and cartesian blocks has been used, see figures 6.1 and 6.4. The grid cells are stretched in the downstream direction and radially towards the boundaries using cubic Hermite grid point distribution. The last contraction of the JEAN project nozzle is included in the calculation domain. The axial extent of the physical part of the domain is 2.5 meters, which is equal to 50 nozzle diameters ($D_j = 50\ [mm]$). The radial extent is 10 nozzle diameters at the nozzle exit plane and 20 diameters at the domain outlet, see figure 5.3.

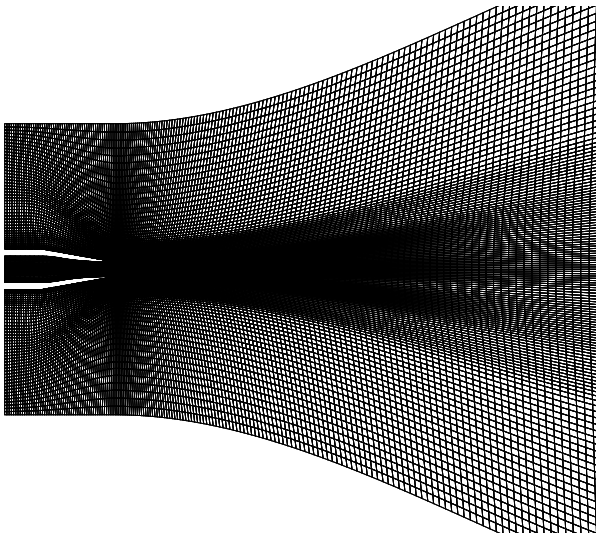

Figure 6.2: A slice through the calculation domain made at $z = 0$, i.e. an xy-plane, is depicted. The figure shows the domain inlet including the nozzle and the outer boundaries in the radial direction. The axial extent of the computational domain is roughly twice that of the mesh slice shown in this figure.

6.2 Flow Parameters

Two jets were simulated in this work: an unheated jet at Mach 0.75 and Reynolds number 5.0×10^4 and a heated jet at the same Mach number and Reynolds number. In the unheated case, the static exhaust temperature, T_j, is equal to the static temperature of the ambient air, T_∞. In the latter case, the exhaust temperature is twice that of the air surrounding the jet. These two jets will from now on be referred to as *Jet I* and *Jet II*, respectively. Properties defining the flow fields of these two jets are specified in table 6.1.

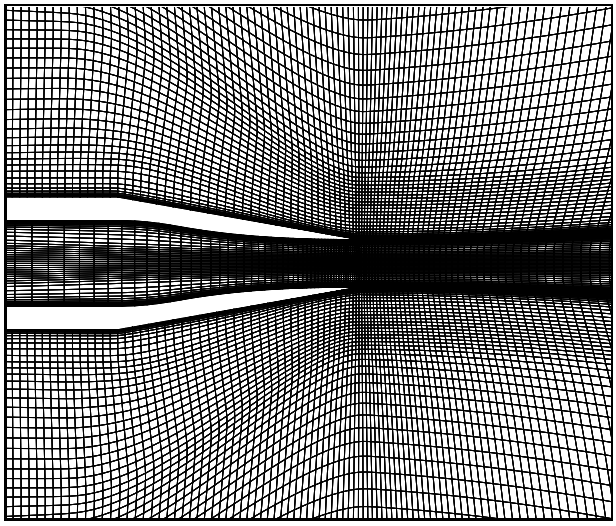

Figure 6.3: A slice of the calculation domain in the nozzle region is shown. Cells are concentrated to the shear layer area.

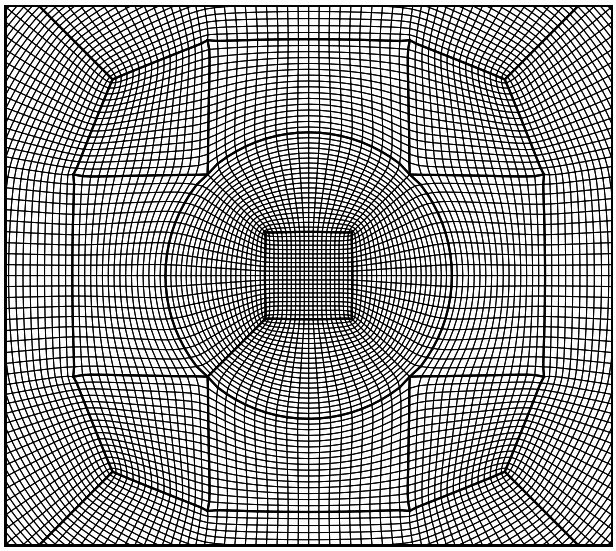

Figure 6.4: A slice through the calculation domain at constant x, i.e. a yz-plane, is depicted. Combining cartesian and polar grid blocks enhances the radial direction grid homogeneity throughout the domain.

6.3 Far-field Observers

Time series of acoustic pressure were obtained in a number of observer locations in the far-field regions of the jet, i.e. outside the regions where hydrodynamic fluctuations dominate and the flow is governed by linear transport equations. Far-field sound pressure levels were evaluated in

	Jet I	*Jet II*
U_j/c_∞	0.75	0.75
T_j/T_∞	**1.0**	**2.0**
$P_\infty\ [Pa]$	101300	101300
$\rho_\infty\ [kg/m^3]$	1.2256	1.2256
$c_\infty\ [m/s]$	340.174	340.174
$U_\infty\ [m/s]$	0.0	0.0
$T_\infty\ [K]$	288	288
$T_{0_j}\ [K]$	**320.4**	**608.4**

Table 6.1: Flow properties of the unheated and heated Mach 0.75 jet, *Jet I* and *Jet II*, respectively. Differences are highlighted using bold face numbers.

25 observer locations. These are situated on two arcs, both with an origin at the nozzle exit, see figure 6.5. On the inner of these two arcs, having a radius of $30D_j$, 14 observers are equally distributed between 20 and 150 degrees from the x-axis. The outer arc has a radius of $r = 50D_j$ and spans from 50 to 150 degrees from the x-axis. Figure 6.5 depicts the observer locations in relation to the calculation domain boundaries and the Kirchhoff surface used. The observer locations coincide with the microphone locations in the experimental setup (Jordan & Gervais, 2003; Jordan *et al.*, 2002*b*). It should be mentioned that the observer at 20° on the lower arc is very close to the Kirchhoff surface, see figure 6.5. This will probably be a source of error. On the other hand, placing the surface closer to the hydrodynamic region might lead to errors for all observers.

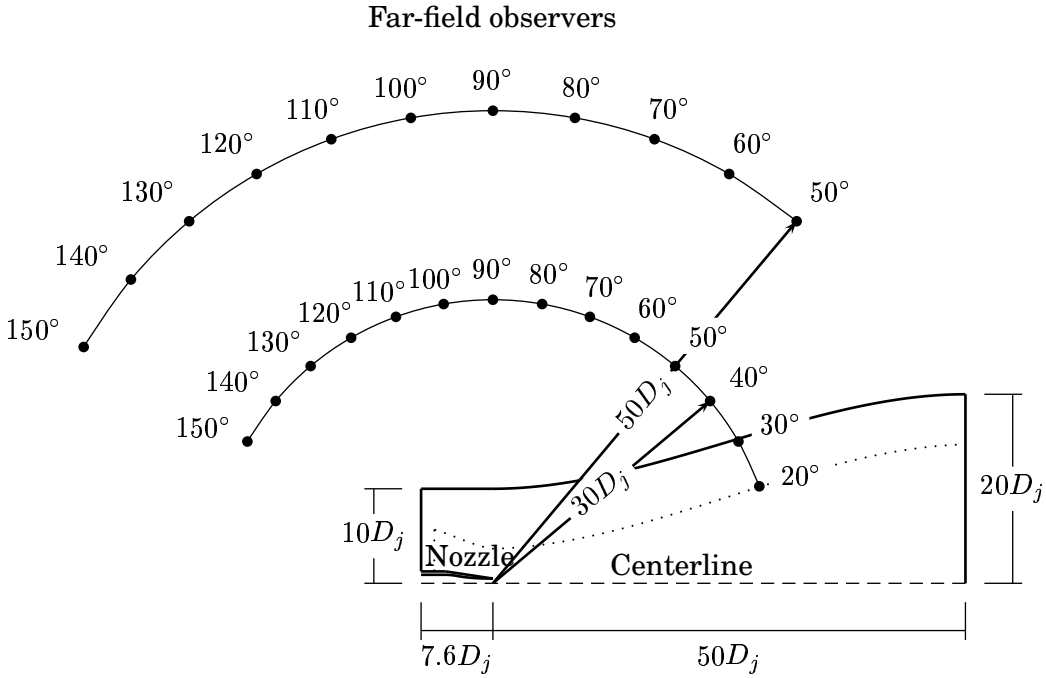

Figure 6.5: In the experiments of Jordan *et al.* (2002*b*), acoustic pressure fluctuations were measured using 25 microphones situated on two arcs in the far-field regions of the jet. The microphone locations are represented by black dots in the figure. Using Kirchhoff surface integration, time series of far-field pressure fluctuations were calculated in the same locations. The dotted line indicates the location of the Kirchhoff surface.

Chapter 7

Results

This chapter gives predictions of near-field aerodynamics of a Mach 0.75 jet and its radiated sound. Section 7.1 shows results for an isothermal jet, *Jet I*, and section 7.2 reports the results for a heated jet, *Jet II*. In section 7.3 the results of these two jets will be compared and the effects of heating on the near-field and the radiated sound will be discussed. The calculations were started up using initial solutions interpolated from 2D RANS calculations.

For *Jet I*, the simulation ran for about 1.0×10^5 time steps before sampling was initiated. This corresponds to 0.025 seconds of simulated time using a time step of 0.25 $[\mu s]$ or roughly 3.5 acoustic through-flows, i.e. the time required for an acoustic wave to travel through the calculation domain, not including the outlet buffer layer, based on the speed of sound at ambient conditions. Sampling of statistical data was then continued for another 20 acoustic through-flows. Each acoustic through-flow corresponds to roughly 32 hours of computer wall-time using 14 AMD 1700^+ processors of our Linux cluster.

For *Jet II*, as for jet *Jet I*, about 3.5 acoustic through-flows were completed before sampling of data was initiated which in this case corresponds to roughly 1.7×10^5 time steps, (Δt =0.15 $[\mu s]$). Sampling of statistical data was then continued for about 14 acoustic through-flows. In this case, due to the shorter time step, each acoustic through-flow corresponds to roughly 54 hours of computer wall time.

The time steps were chosen such that the CFL number was not larger than 0.5 any where.

$$CFL = \frac{(|u| + c)\,\Delta t}{\Delta x} \tag{7.1}$$

Profiles of statistical quantities to be presented in the following sections are obtained from flow field data that were averaged in both time and the azimuthal direction to establish improved statistical convergence. The profiles are made non-dimensional using the jet velocity at the nozzle exit, U_j, and the nozzle outlet diameter, D_j.

7.1 Mach 0.75, Unheated Jet (*Jet I*)

7.1.1 Instantaneous Flow Field

Figure 7.1 shows isosurfaces of negative second eigenvalues of the second-order tensor $(S_{ik}S_{kj} + \Omega_{ik}\Omega_{kj})$. S_{ij} and Ω_{ij} are the strain-rate tensor and rotation tensor, respectively, i.e. the symmetric and antisymmetric part of the velocity gradient tensor. This is a criterion for the vortex core proposed by Jeong & Hussain (1995) and can be interpreted physically as a local pressure minima caused by vortical motion. This method was developed for incompressible flows but has been used here as a visualization tool for a compressible flow. Even if the method is not correctly used, the development of flow structures is probably physical. It can be seen from the upper picture in figure 7.1 how small structures generated at the nozzle lip region when the high velocity exhaust meets the stagnant ambient surroundings grow in size as they move downstream. In the lower picture, the magnitude of the eigenvalue is increased by a factor of ten and only the smallest structures in the vicinity of the nozzle are shown. This picture shows how the fluid rolls up when it comes out of the nozzle, forming vortex rings, and how these structures quickly break up as they move downstream. Figure 7.2 shows instantaneous contours of axial velocity in two planes. The left figure is an xz-plane showing the development of the shear layer and the right figure shows the three-dimensionality of the jet in a yz-plane cutting through the jet at $x = 3.0D_j$.

7.1.2 Time-averaged Profiles

Figure 7.3 depicts the development of radial profiles of axial velocity downstream of the nozzle exit. Comparisons of profiles obtained from LES and experiments are presented in figures 7.5–7.11. The radial profiles have been staggered corresponding to the axial position, i.e. 1.0, 2.5 and 5.0 jet diameters respectively, to show downstream development. Furthermore, it should be noted that, in order to obtain similar scales for all the radial profile figures, root-mean-square values and uv correlations have been multiplied by a factor 4 and 70, respectively.

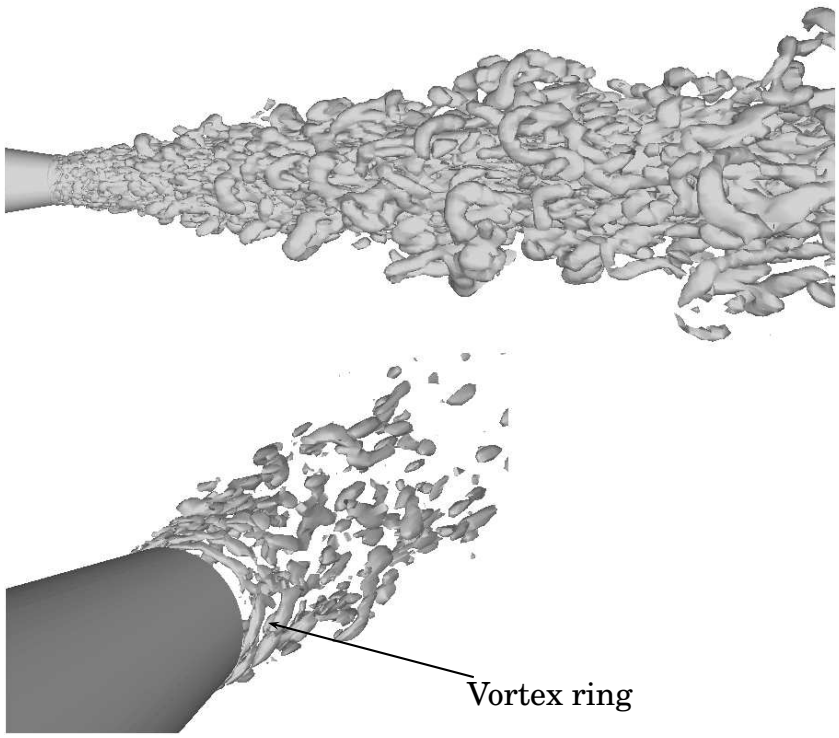

Figure 7.1: Isosurface of negative second eigenvalues of $A_{ij} = (S_{ik}S_{kj} + \Omega_{ik}\Omega_{kj})$. The upper picture shows the development of vortical structures moving downstream the jet. The lower figure shows the break-up of vortical structures generated in the initial regions of the shear layer.

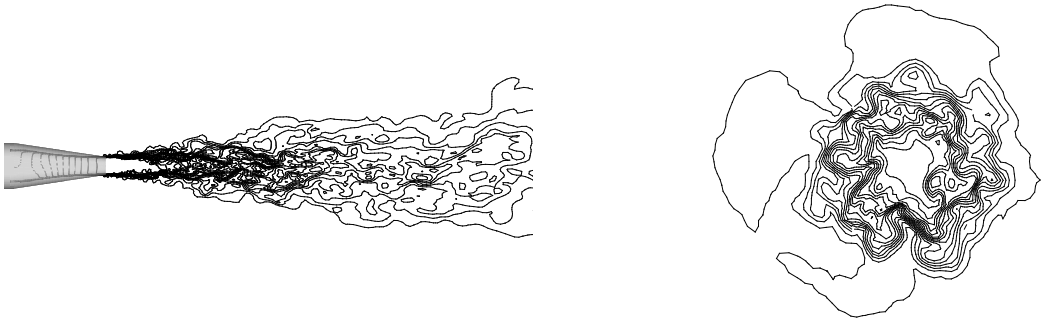

Figure 7.2: Contours of instantaneous axial velocity. The left picture shows contours in the plane $y = 0.0$ and the right picture in the plane $x = 0.15$, i.e. 3 jet diameters downstream of the nozzle exit.

The location of the lines along which axial and radial profiles have been extracted is shown in figure 7.4.

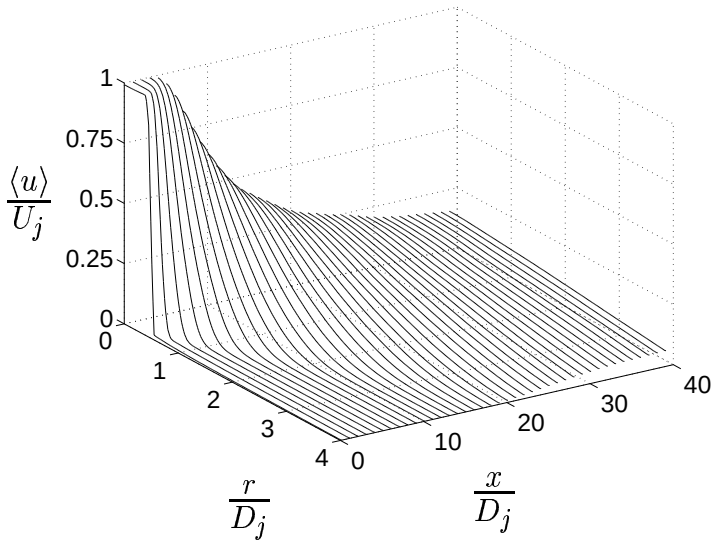

Figure 7.3: Downstream development of radial profiles of axial velocity.

Although the LES results are in good agreement with experiments, there are some deviations. The main discrepancy is that the LES fails to predict the length of the jet potential core, figure 7.5, and thereby the location of maximum turbulence intensity, figure 7.7. It has been mentioned by DeBonis & Scott (2001) that this is generally not the case in earlier studies of jets; rather, the length of the potential core is usually over predicted. Although the location of the potential core closure is not accurately predicted, the rate of decay of the centerline axial velocity is. Moreover, it is seen from figure 7.6 that the initial jet spreading is slightly underpredicted. This is probably an effect of the entrainment boundary conditions used. Furthermore, it has been mentioned by Morris *et al.* (2000) that a change in the subgrid scale model constants affects the potential core length and the initial growth of the jet. These subgrid scale effects can, since the grid used for the simulation is rather coarse, probably be diminished by grid refinement or by the use of a more sophisticated subgrid scale model. Large deviations from experimental data in root-mean-square values of radial velocity near the centerline, figures 7.9–7.10, might be caused by low frequency flutter of the potential core found in the experiments, see Jordan *et al.* (2002*a*). Centerline profiles of root-mean-square profiles of axial and radial velocity are shown in figure 7.7 and figure 7.9, respectively. The maximum level is in both cases somewhat underpredicted but, as can be seen by comparing the two figures, the turbulence anisotropy of the jet has been correctly predicted.

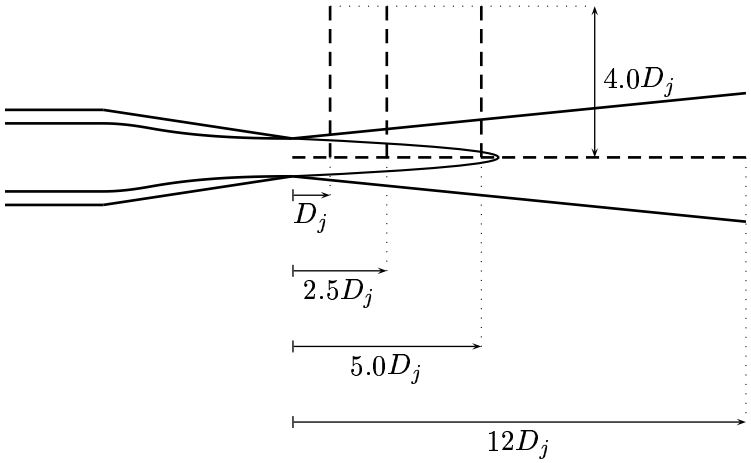

Figure 7.4: Profiles of axial velocity and second-order moments are obtained along the centerline and along three radial lines.

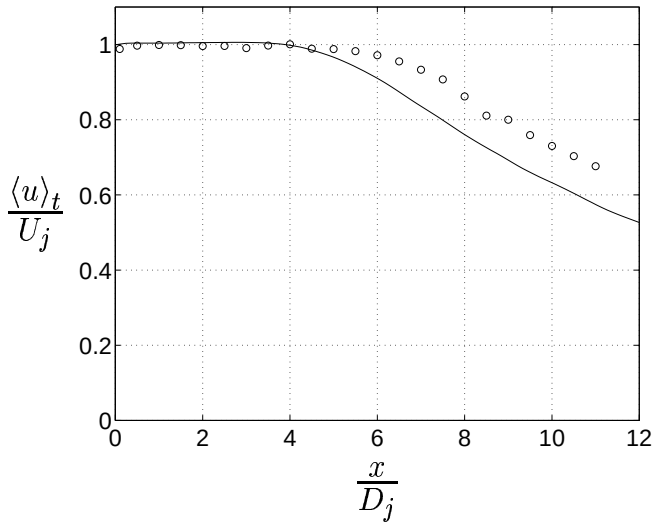

Figure 7.5: Centerline velocity: the solid line, $'-'$, corresponds to LES results and the circles, $'o'$, to experimental data (Jordan *et al.*, 2002*a*).

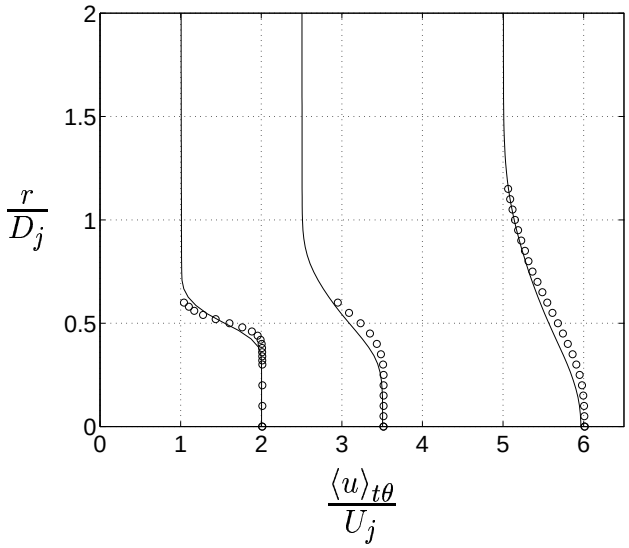

Figure 7.6: Radial profiles of axial velocity at the axial positions $x/D_j = 1.0$, $x/D_j = 2.5$ and $x/Dj = 5.0$: $'-'$ corresponds to LES results and $'o'$ to experimental data (Jordan *et al.*, 2002*a*). The profiles have been staggered corresponding to their axial position.

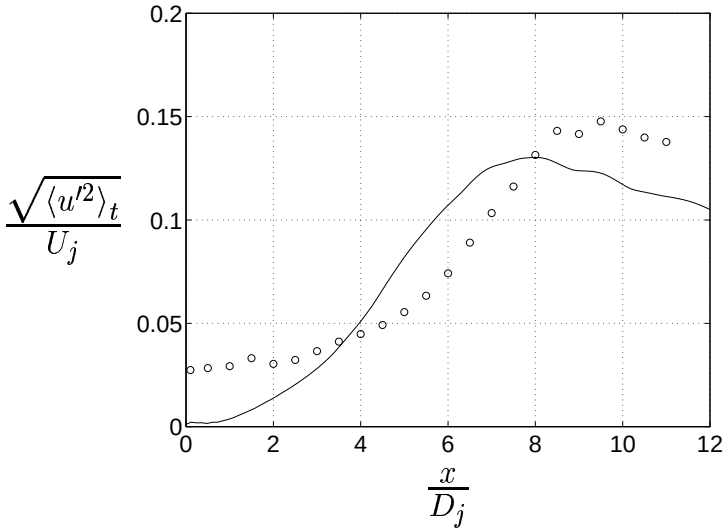

Figure 7.7: Axial profile of $\sqrt{\langle u'^2 \rangle_t}$: $'-'$ corresponds to LES results and $'o'$ to experimental data (Jordan *et al.*, 2002*a*).

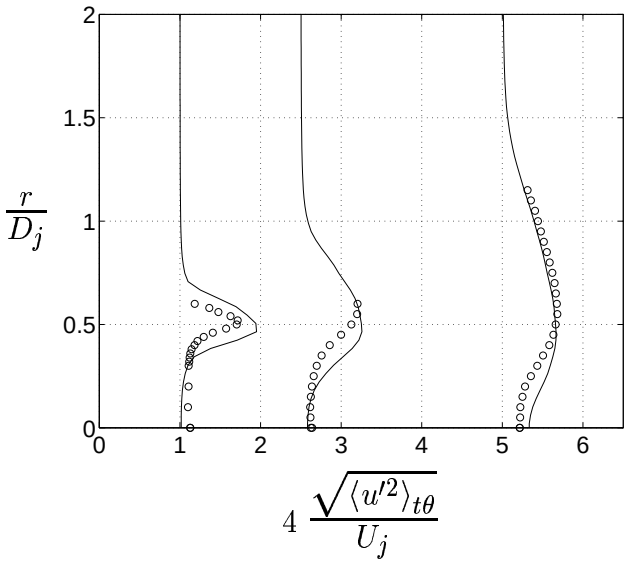

Figure 7.8: Radial profiles of $\sqrt{\langle u'^2\rangle_{t\theta}}$ at $x/D_j = 1.0$, $x/D_j = 2.5$ and $x/D_j = 5.0$: $'-'$ corresponds to LES results and $'o'$ to experimental data (Jordan *et al.*, 2002*a*). The profiles have been staggered corresponding to their axial position.

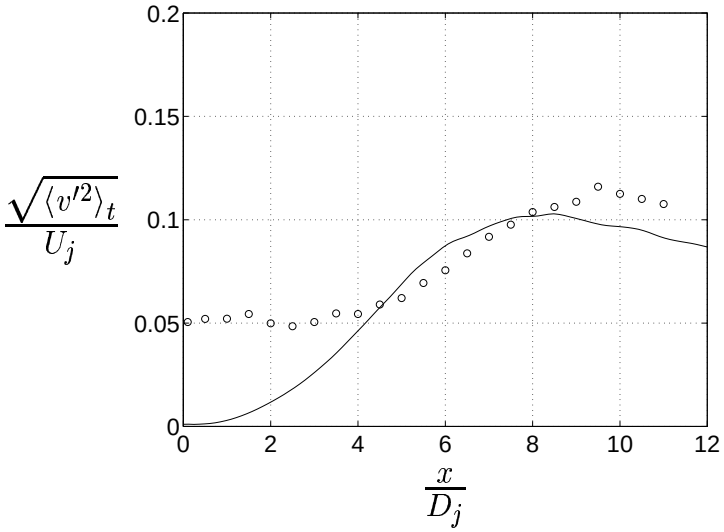

Figure 7.9: Axial profile of $\sqrt{\langle v'^2\rangle_t}$: $'-'$ corresponds to LES results and $'o'$ to experimental data (Jordan *et al.*, 2002*a*).

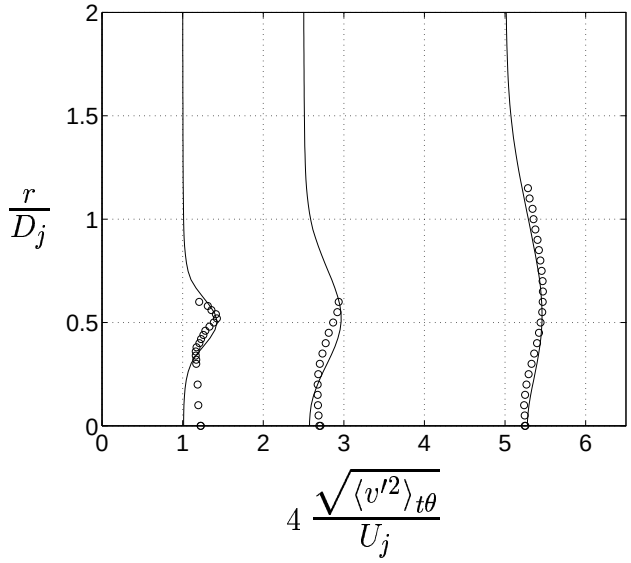

Figure 7.10: Radial profiles of $\sqrt{\langle v'^2\rangle_{t\theta}}$ at $x/D_j = 1.0$, $x/D_j = 2.5$ and $x/D_j = 5.0$: $'-'$ corresponds to LES and $'o'$ to experimental data (Jordan *et al.*, 2002*a*). The profiles have been staggered corresponding to their axial position.

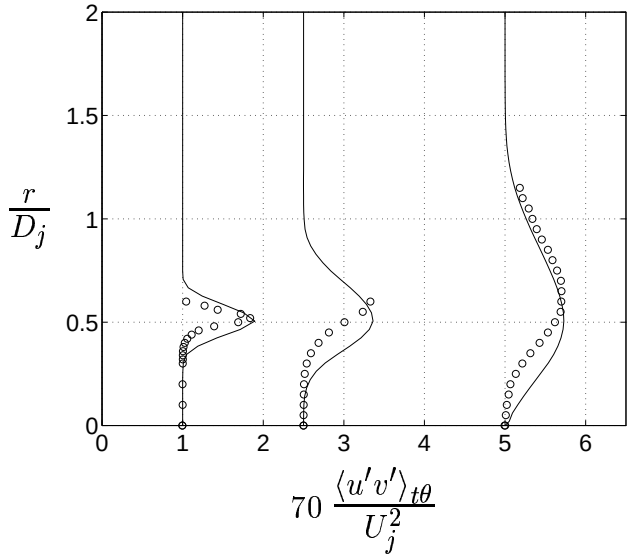

Figure 7.11: Radial profiles of $\langle u'v'\rangle_{t\theta}$ at $x/D_j = 1.0$, $x/D_j = 2.5$ and $x/D_j = 5.0$: $'-'$ corresponds to LES and $'o'$ to experimental data (Jordan *et al.*, 2002*a*). The profiles have been staggered corresponding to their axial position.

7.1.3 Self-preservation

Radial profiles of axial velocity and second-order moments were normalized by centerline velocity and plotted versus a non-dimensional radial coordinate to investigate whether or not self-preservation has been established. These profiles are obtained using statistical flow field data averaged in time and the azimuthal direction. The constant, x_0, used to collapse the profiles is a virtual origin obtained from the least square fit of data points in figure 7.12, i.e. the axial position for which $U_j/\langle u_c \rangle_t = 0$. In this case $x_0 = 0.11 D_j$. As seen in figure 7.12, a non-negligible deviation from the linear relation occurs for centerline points located between $20D_j$ and $35D_j$ downstream of the nozzle exit. This behavior is probably due to the boundary conditions used. However, since this occurs far downstream, the effect on the flow field in the region near the jet exit ($x < 20D_j$) is probably negligible. Figure 7.13 shows collapsed radial profiles of axial velocity. Five radial profiles equally spaced between $19D_j$ and $39D_j$ were used. The jet-spreading rate can be estimated to be roughly 0.09 based on the curve fitted to the LES data. Figures 7.14–7.17 depict normalized profiles of second-order moments. For these figures, radial profiles in six axial positions from $29D_j$ to $39D_j$ downstream of the nozzle were used. The distance between each profile is, in this case, two jet diameters. As can be seen in the figures 7.13–7.17, self-preservation of axial velocity has been well established within 39 jet diameters downstream of the nozzle whereas, for self-preservation of second-order moments to be obtained, data would have to be extracted further downstream. For example, Hussein *et al.* (1994) and Wygnanski & Fiedler (1969) found that profiles of second and higher-order moments displayed self-similar behavior when evaluated at axial positions more than $70D_j$ downstream of the virtual origin. However, this would require the use of a larger computational domain. Comparing the profiles of turbulence intensities it seems to be easier to obtain self-preserving behavior for those not including fluctuations of axial velocity.

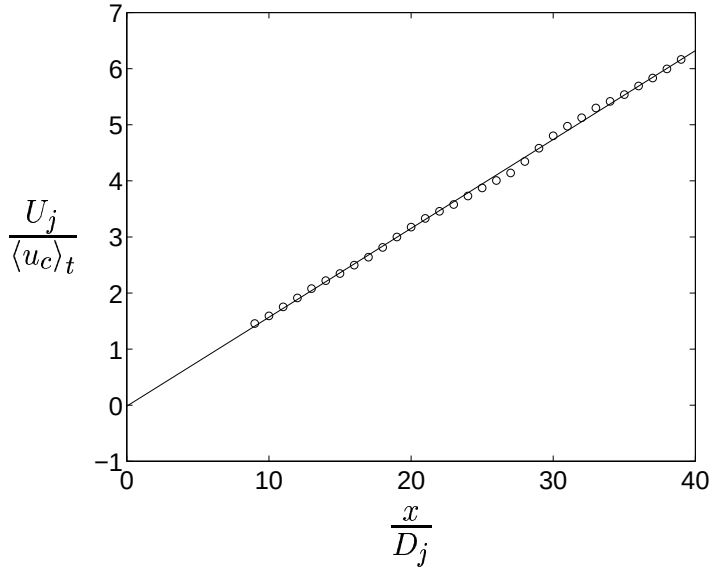

Figure 7.12: Predicted centerline velocity. The solid line corresponds to a curve fit to the LES data. The x-value for which the line intersects the x-axis, x_0, is used to collapse the radial profiles in figures 7.13–7.17.

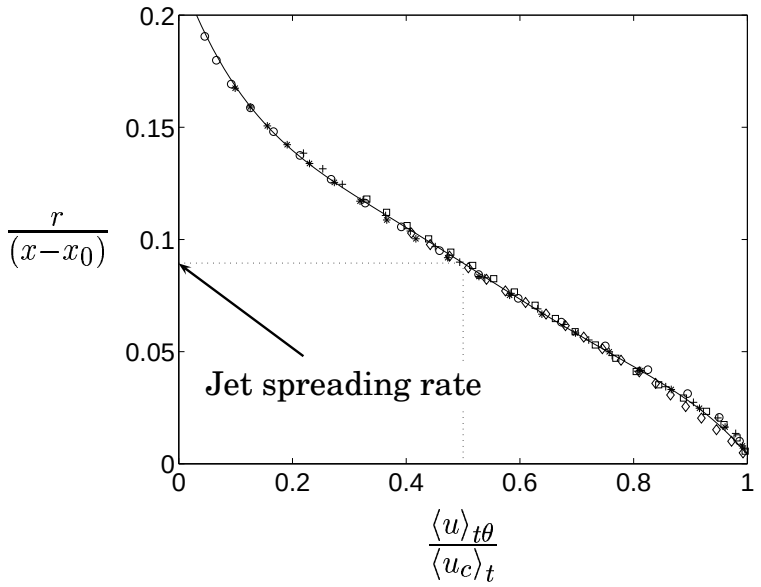

Figure 7.13: Radial profiles of axial velocity normalized by centerline mean velocity. The solid line corresponds to a curve fit to the LES data. The profiles are labeled as follows: $' \circ ' = 19D_j$, $' * ' = 24D_j$, $' + ' = 29D_j$, $' \Box ' = 34D_j$ and $' \diamond ' = 39D_j$.

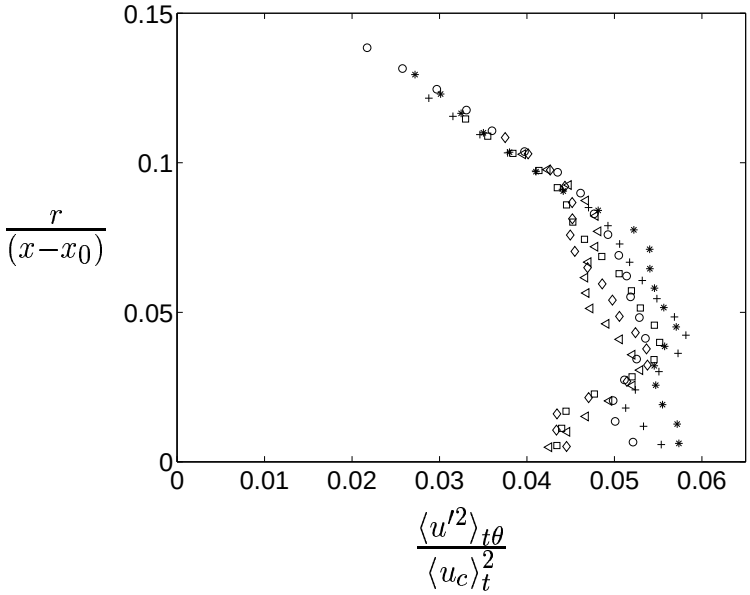

Figure 7.14: Radial profiles of $\langle u'u' \rangle_{t\theta}$ normalized by centerline mean velocity. Radial profiles at six axial locations are represented. The profiles are labeled as follows: $' \circ ' = 29D_j, ' * ' = 31D_j, ' + ' = 33D_j$, $' \square ' = 35D_j, ' \diamond ' = 37D_j$ and finally $' \triangleleft ' = 39D_j$.

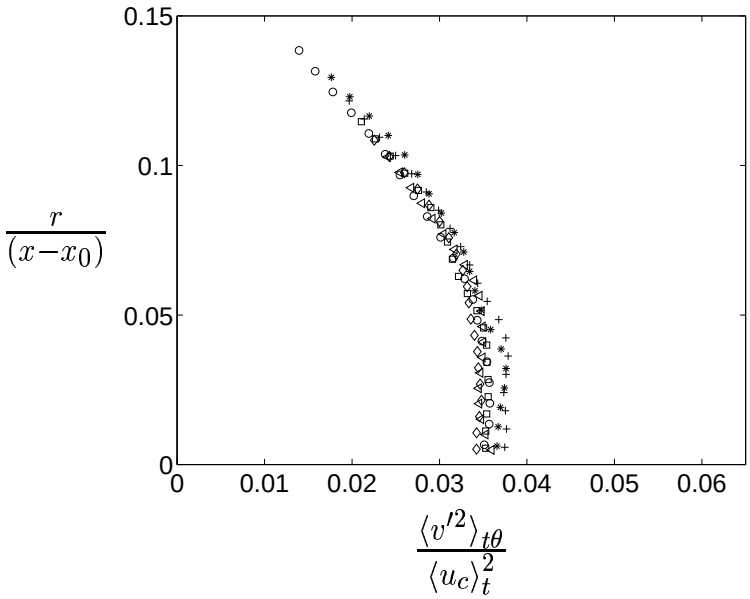

Figure 7.15: Radial profiles of $\langle v'v' \rangle_{t\theta}$ normalized by centerline mean velocity. For legend see figure 7.14.

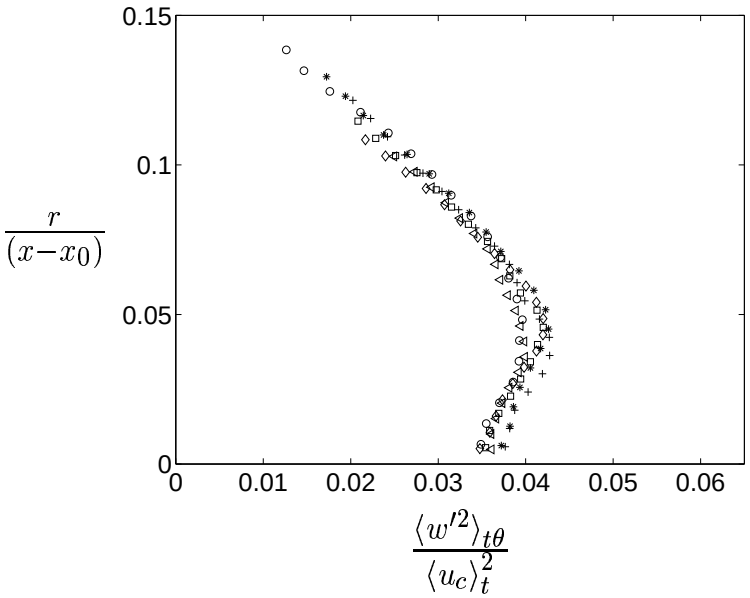

Figure 7.16: Radial profiles of $\langle w'w' \rangle_{t\theta}$ normalized by centerline mean velocity. For legend see figure 7.14.

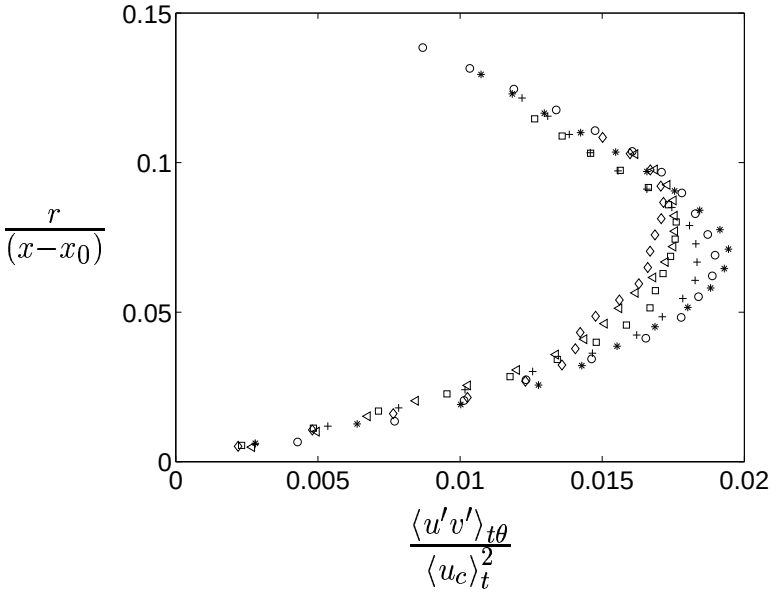

Figure 7.17: Radial profiles of $\langle u'v' \rangle_{t\theta}$ normalized by centerline mean velocity. For legend see figure 7.14.

7.1.4 Two-point Space-time Correlations

Two-point space-time correlations were obtained for axial velocity in a few points in the shear layer region downstream of the nozzle exit. The time series used is 0.0725 seconds. Spatial separations, ξ, are in this case downstream in the axial direction. The two-point space-time correlation of axial velocity for a certain spatial separation, ξ, and separation in time, τ, is given by

$$R_{uu}\left(\mathbf{x},\xi,\tau\right)=\frac{\left\langle u'\left(\mathbf{x},t\right)u'\left(\mathbf{x}+\xi,t+\tau\right)\right\rangle_t}{\sqrt{\left\langle u'^2\left(\mathbf{x}\right)\right\rangle_t}\sqrt{\left\langle u'^2\left(\mathbf{x}+\xi\right)\right\rangle_t}} \tag{7.2}$$

where u' denotes fluctuation of axial velocity and x is the position in the flow field where the two-point correlation is evaluated, see figure 7.18.

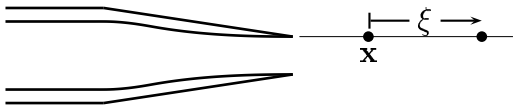

Figure 7.18: Two-point space-time correlations in the shear layer are obtained for location, x, using a spatial separation, ξ.

Figures 7.19–7.21 show two-point correlations in points located on the nozzle lip-line 2.5, 5.0 and 10.0 nozzle diameters downstream of the nozzle exit. Each figure contains the autocorrelation of axial velocity fluctuations, i.e. no spatial separation, and 30 two-point space-time correlations obtained with increased spatial separation. Each consecutive correlation curve corresponds to an increase in spatial separation by $0.1D_j$. The integral of the envelope built up of the two-point correlation curves corresponds to the Lagrangian time scale in the current position in the flow. Comparing figures 7.19–7.21, the amplitude for a given spatial separation, ξ, increases downstream the jet, which indicates that the turbulence becomes more and more frozen in character, i.e. the turbulence length scale increases as the jet develops. A comparison was made with two-point measurements in the shear layer at the end of the potential core, $x = L_c$. Here the potential core length is defined as the axial location where the centerline mean velocity equals $0.95U_j$. For the LES, this gives $L_c = 5.4545D_j$ and, for the measured data, $L_c = 6.50D_j$. For more detail on the two-point measurements see Jordan & Gervais (2003). In figure 7.22, correlation peak locations of the two-point space-time correlations obtained from LES data are compared with those from the two-point measurements. Figure 7.23 shows a comparison of

predicted autocorrelation and two-point correlation envelope with the corresponding curves obtained from measured data. These are again obtained in the shear layer at the potential core closure. The autocorrelation and the envelope represent the Eulerian and Lagrangian time scales, respectively. Figure 7.24 shows the spatial correlations of axial velocity in three locations and figure 7.25 shows a comparison of the predicted and measured spatial correlations at $(x = L_c, r = 0.5D_j)$.

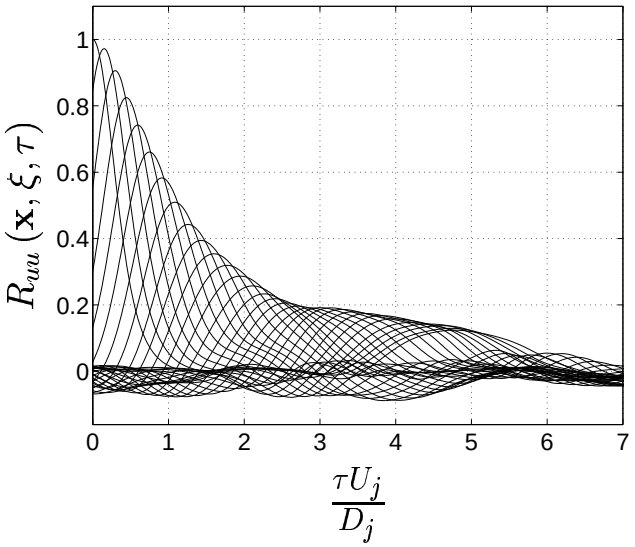

Figure 7.19: Two-point space-time correlation of axial velocity at a location, x, in the shear layer $r = 0.5D_j,\ x = 2.5D_j$. Each curve corresponds to a two-point space-time correlation obtained using a certain spatial separation, ξ. Starting with no separation in space, i.e. the autocorrelation, the spatial separation is increased by $0.1D_j$ per curve.

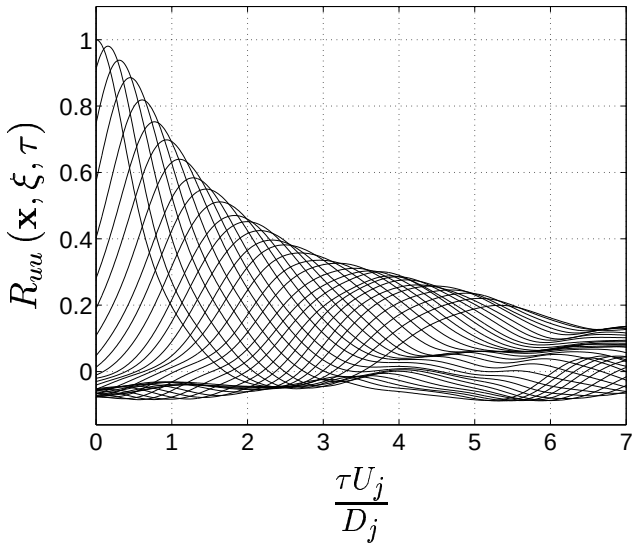

Figure 7.20: Two-point space-time correlation of axial velocity at a location, x, in the shear layer $r = 0.5D_j,\ x = 5.0D_j$. See also legend to figure 7.19.

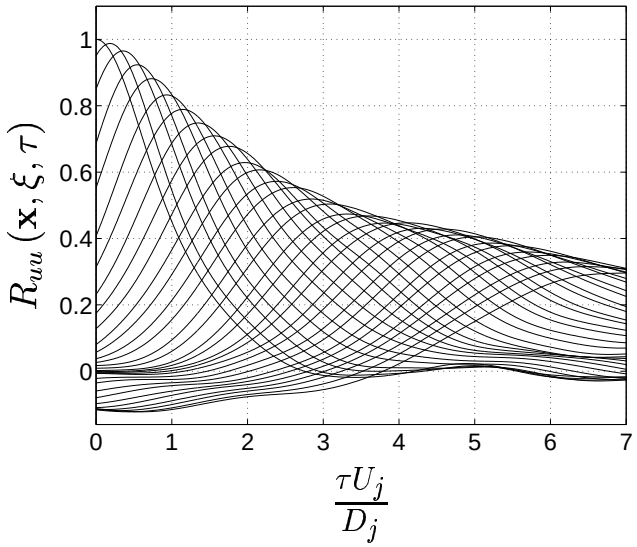

Figure 7.21: Two-point space-time correlation of axial velocity at a location, x, in the shear layer $r = 0.5D_j,\ x = 10.0D_j$. See also legend to figure 7.19.

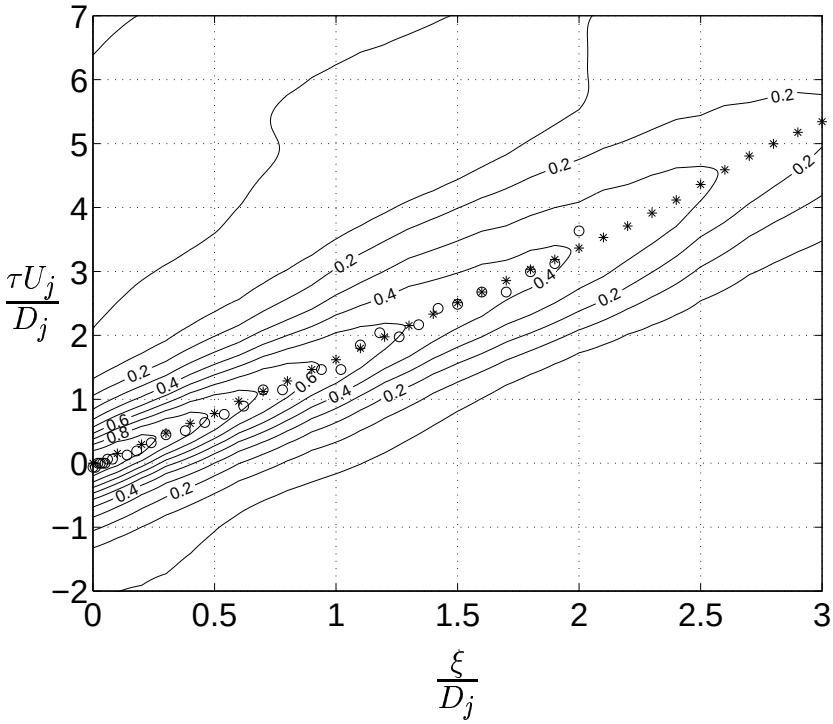

Figure 7.22: Contours of $R_{uu}(\mathbf{x}, \xi, \tau)$ obtained in the shear layer, $r = 0.5D_j$, at the end of the potential core, $x = L_c = 5.5D_j$. The contours corresponds to LES data, $'\ *\ '$ corresponds to the correlation peaks of these two-point space-time correlations and $'\ \circ\ '$ to the peaks of the correlations obtained from the velocity data measured by Jordan & Gervais (2003).

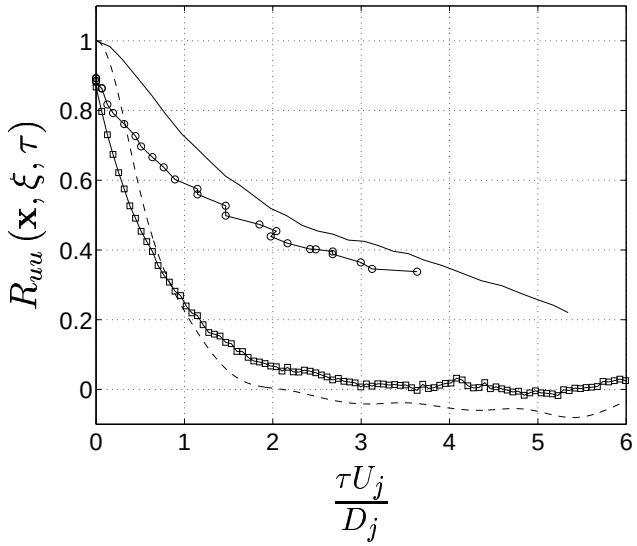

Figure 7.23: Comparison of the autocorrelation and the two-point space-time correlation envelope for the LES data and the measured data. The data are in both cases obtained in the shear layer at the potential core closure ($x = L_c$). The solid line denotes the envelope of the LES data and the solid line with circles the corresponding measured data. The dashed line corresponds to the autocorrelation of the LES data and the solid line with squares denotes the autocorrelation of the data measured by Jordan & Gervais (2003).

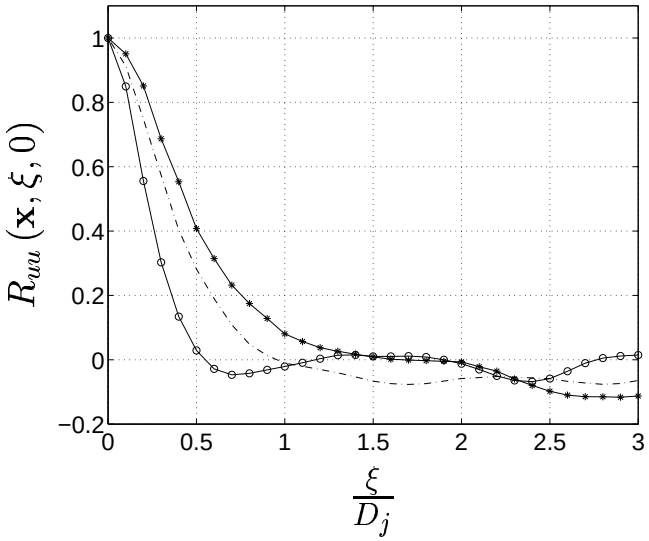

Figure 7.24: Predicted two-point correlation of axial velocity at three different locations, x, in the shear layer: $'-o'$ corresponds to a location $x = 2.5D_j$ downstream of the nozzle exit, $'-\cdot'$ to $x = 5.0D_j$ and $'-*'$ to $x = 10D_j$. All points are located at $r = 0.5D_j$.

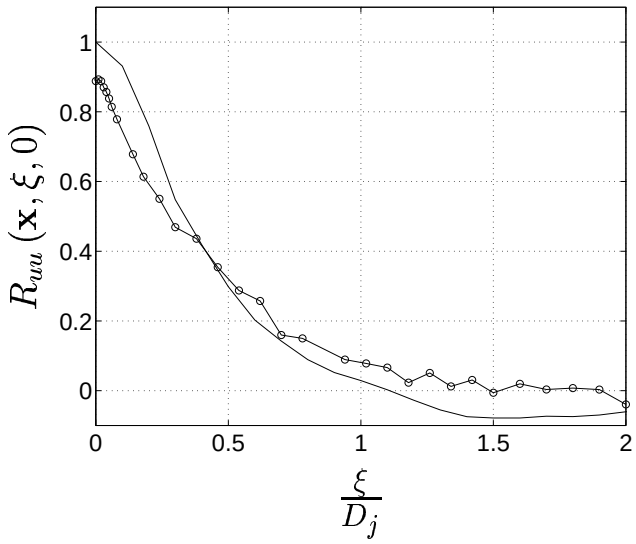

Figure 7.25: Comparison of spatial correlation in the shear layer at the potential core closure. The solid line denotes LES data and the solid line with circles data measured by Jordan & Gervais (2003).

7.1.5 Length and Time Scales of Turbulence Structures

Length and time scales of turbulence quantities were obtained using the two-point space-time correlations presented in the previous section. Estimates of convection velocity of turbulence structures were also obtained for a number of axial locations in the shear layer. The separation in time between the peak of the autocorrelation curve and the peak of the first following two-point correlation curve was used. This time delay corresponds to a spatial separation of $0.1D_j$, as mentioned previously, and thus gives an estimate of the convection velocity, see figure 7.26.

$$U^c = \frac{\xi}{\tau_{R_{max}}} \tag{7.3}$$

A more correct way would be not to use the temporal separation for the peak but rather the time for which the two-point space-time correlation envelope is a tangent to the correlation curve (Fisher & Davies, 1963). However, the result would not differ a great deal. Predicted convection velocities for a few axial locations are presented in table 7.1. In the middle column, the convection velocities have been normalized by the jet velocity, U_j, and, in the right column, by the local mean velocity. As shown in table 7.1, the eddy convection velocity is everywhere higher than the local mean velocity. This might be a nonintuitive result but is a phenomenon observed in experiments (Fisher & Davies, 1963; Wygnanski & Fiedler, 1969) and is caused by skewness of the velocity distribution. In shear layer locations close to the high velocity potential core, the convection velocity is likely to be larger than the local mean velocity and lower in the outer parts of the shear layer (Fisher & Davies, 1963). Moreover, a turbulence convection velocity equal to the local mean velocity would indicate frozen turbulence (Hinze, 1975). The increasing deviation from unity of the correlation peaks for increasing spatial separation shows that the turbulence in this case can not be considered frozen, see figures 7.19–7.21. In the outer part of the jet, i.e. in the region of the interface between the turbulent jet flow and the irrotational outer flow, the skewness is directly attributable to the flow intermittancy.

Local integral length and time scales are estimated by integration of the corresponding autocorrelation and spatial correlation, respectively. The first crossing of the coordinate axis is used as the upper limit for the integration. The Lagrangian time scale, $\mathcal{T}_L$, corresponds to the integral of the correlation envelope. Since the envelope does not intersect

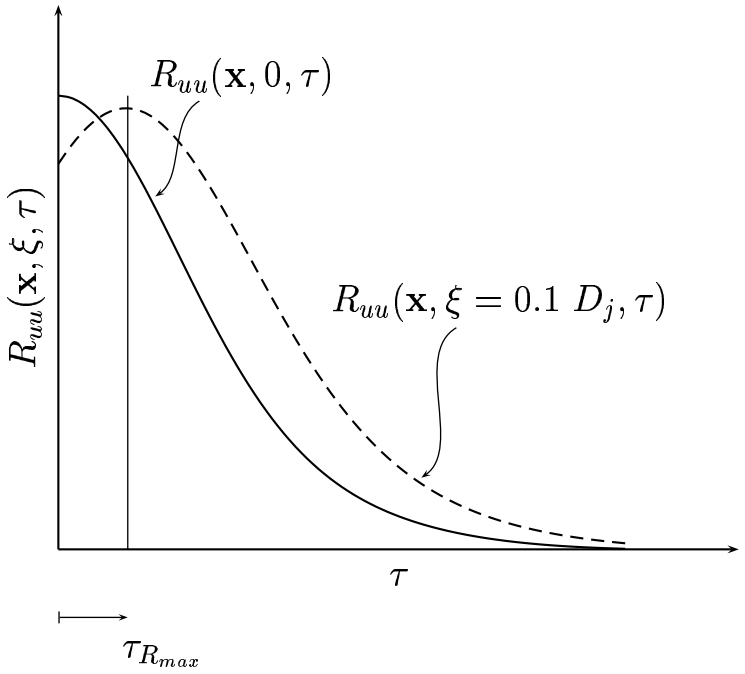

Figure 7.26: The eddy convection velocity is calculated using the temporal separation corresponding to the maximum correlation of a space-time correlation obtained for a spatial separation of $0.1D_j$.

the τ-axis for the range of temporal separation used, an analytic function representing the enveloped must be used to obtain the time scale.

$$R_{uu}\left(\mathbf{x}, \xi, \tau\right) = e^{-|\tau|/\mathcal{T}_L} \tag{7.4}$$

The axial development of integral length and time scales are shown in figures 7.27–7.29. In these figures, scales obtained from measured data are represented by circles.

x/D_j	U^c/U_j	$U^c/\langle u \rangle_t$
2.50	0.65	1.09
3.00	0.71	1.19
3.50	0.71	1.21
4.00	0.71	1.23
4.50	0.71	1.24
5.00	0.65	1.15
5.50	0.65	1.16
6.00	0.60	1.09
6.50	0.65	1.20
7.00	0.71	1.31
7.50	0.65	1.22
8.00	0.65	1.24
8.50	0.60	1.16
9.00	0.65	1.28
9.50	0.60	1.22
10.00	0.56	1.16

Table 7.1: Predicted convection velocity of turbulence structures in the shear layer, $r = 0.5D_j$.

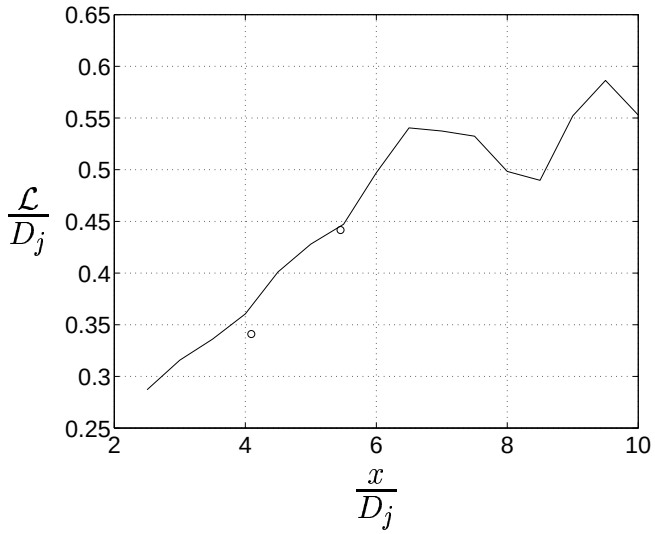

Figure 7.27: Axial development of the integral length scale in the shear layer, i.e. $r = 0.5D_j$. $' \circ '$ denotes experiments (Jordan & Gervais, 2003).

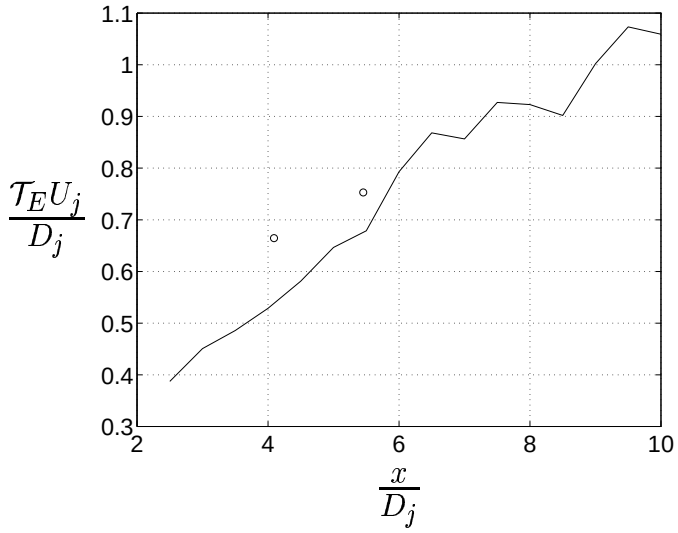

Figure 7.28: Axial development of the Eulerian integral time scale in the shear layer, i.e. $r = 0.5D_j$. For legend see figure 7.27.

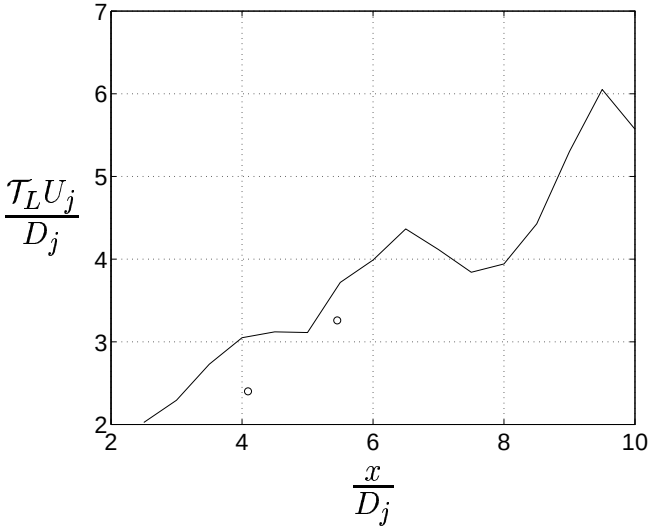

Figure 7.29: Axial development of the Lagrangian integral time scale in the shear layer, i.e. $r = 0.5D_j$. For legend see figure 7.27.

7.1.6 Far-field Sound Pressure Levels

Comparisons of predicted far-field sound pressure levels (SPL) and levels measured by Jordan *et al.* (2002*b*) are shown in figures 7.30 and 7.31. The time series of far-field pressure fluctuations used for the evaluation contains about 1.5×10^4 samples and is roughly $0.038\ [s]$. The observer locations for which sound pressure levels are presented in figure 7.30 are located on a $30D_j$ radius arc and those in figure 7.31 on a $50D_j$ radius arc. The observer locations in relation to the Kirchhoff surface used are shown in figure 4.3. The sound pressure level is here defined as

$$SPL = 20\log_{10}\left(\frac{\sqrt{\langle (p')^2 \rangle_t}}{p_{ref}}\right) \tag{7.5}$$

where

$$p_{ref} = \sqrt{\rho_\infty c_\infty 10^{-12}} = 2.0 \times 10^{-5}\ [Pa] \tag{7.6}$$

corresponds to the threshold of human hearing at a frequency of 1000 Hz. Sound pressure levels obtained using all spectral information available are often referred to as overall sound pressure levels (OASPL). The time history of pressure in the observer locations was obtained numerically using instantaneous flow data from the LES in combination with Kirchhoff surface integration. This procedure was described in more detail in section 5.4. As can be seen in the figures, predicted levels agree very well with experimental data. The predicted levels are not as good for angles below $40°$ and higher than $120°$ as for those in between. This is especially noticeable for the lower arc. In this case the fact that the observer locations are very close to the Kirchhoff surface might affect the levels obtained. Furthermore, Shur *et al.* (2003) states that the downstream closing surface might be important for the sound pressure levels obtained at low angles. Still, the slightly overpredicted sound pressure levels for high angles must be explained.

Figure 7.32 shows a comparison of the power spectrum of predicted pressure fluctuations in a couple of observer locations with the corresponding spectra obtained for the measured data (Jordan *et al.*, 2002*b*). For low and high angles, the predicted levels are in good agreement with the experimental data up to at least Strouhal number $St = 1.5$, see figure 7.32(a). For the intermediate angles on the other hand, the predicted amplitude decreases rapidly above $St = 1.0$. This is due to the fact that the grid is not fine enough to support high frequency acoustic waves in the radial direction. Assuming that it is sufficient to have four cells per wavelength to be able to capture a propagating wave of

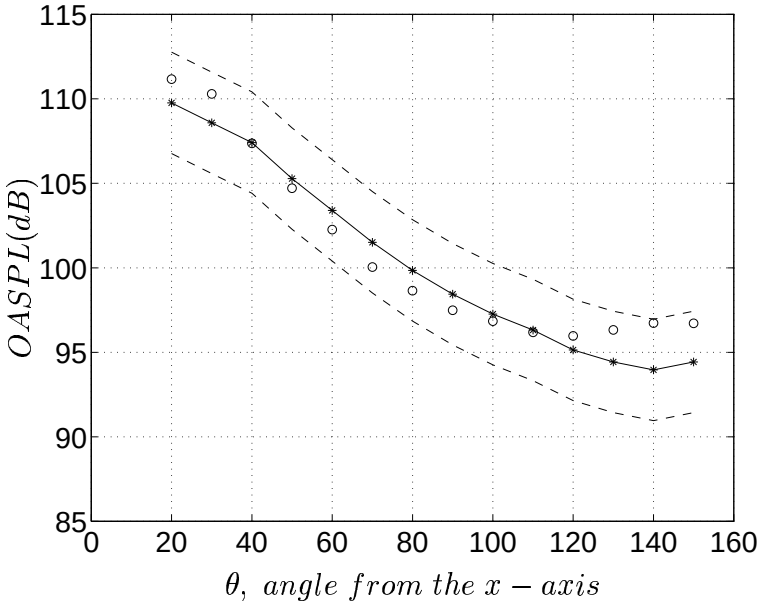

Figure 7.30: Far-field sound pressure levels in microphone locations $30D_j$ from the nozzle exit: $'-*'$ corresponds to sound pressure levels measured by Jordan *et al.* (2002*b*) and the dashed lines $'--'$ to the measured levels $\pm$ 3dB. $'o'$ denotes calculated sound pressure levels using Kirchhoff surface integration.

a certain frequency, the cells in the area where the Kirchhoff surface is located would support propagating waves of Strouhal numbers up to $St \simeq 1.2$. The filtering of acoustic waves caused by the coarseness of the mesh might be an explanation for the overpredicted sound pressure levels at high angles, see figure 7.30. This overprediction might be caused by unphysical, high frequency acoustic waves generated in the hydrodynamic jet region. An indication of such pollution of high frequencies by the presence of spurious noise was found when Lighthill's acoustic analogy was used for sound propagation. This will be discussed in more detail in section 7.4. These high frequency waves will, for most observers, be damped out by numerical dissipation. However, in the upstream direction, the resolution is significantly finer relative to the downstream direction, see figure 6.2. This means that some of these non-physical waves might reach the Kirchhoff surface and contribute to the overall sound pressure levels for the upstream observers. By band-pass filtering the observer pressure signal, these effects can be diminished, as shown in figures 7.33–7.34. The pressure signals were filtered with a lower cut-off frequency corresponding to $St = 0.05$ and

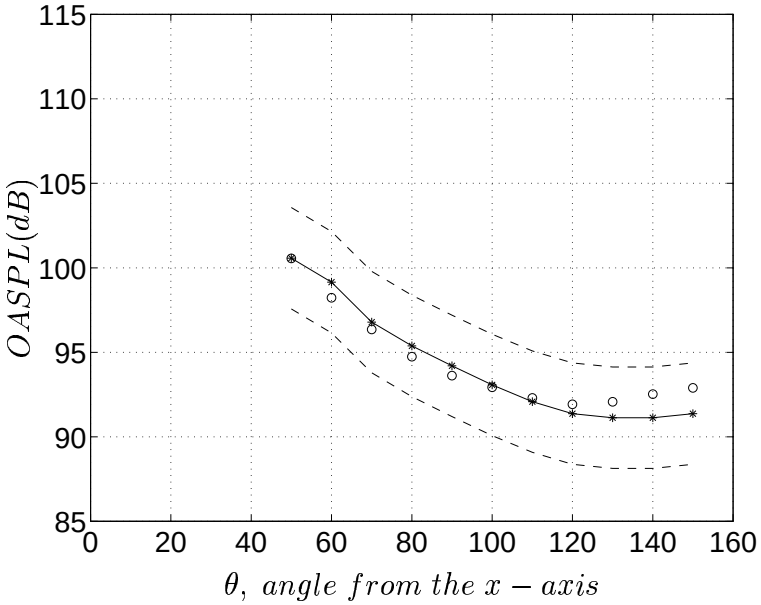

Figure 7.31: Far-field sound pressure levels in microphone locations $50D_j$ from the nozzle exit. See also legend in figure 7.30.

upper cut-off corresponding to $St = 1.0$. The reason for using a band-pass filter instead of a low-pass filter is that this approach removes some of the high amplitudes obtained for very low Strouhal numbers, see figure 7.32.

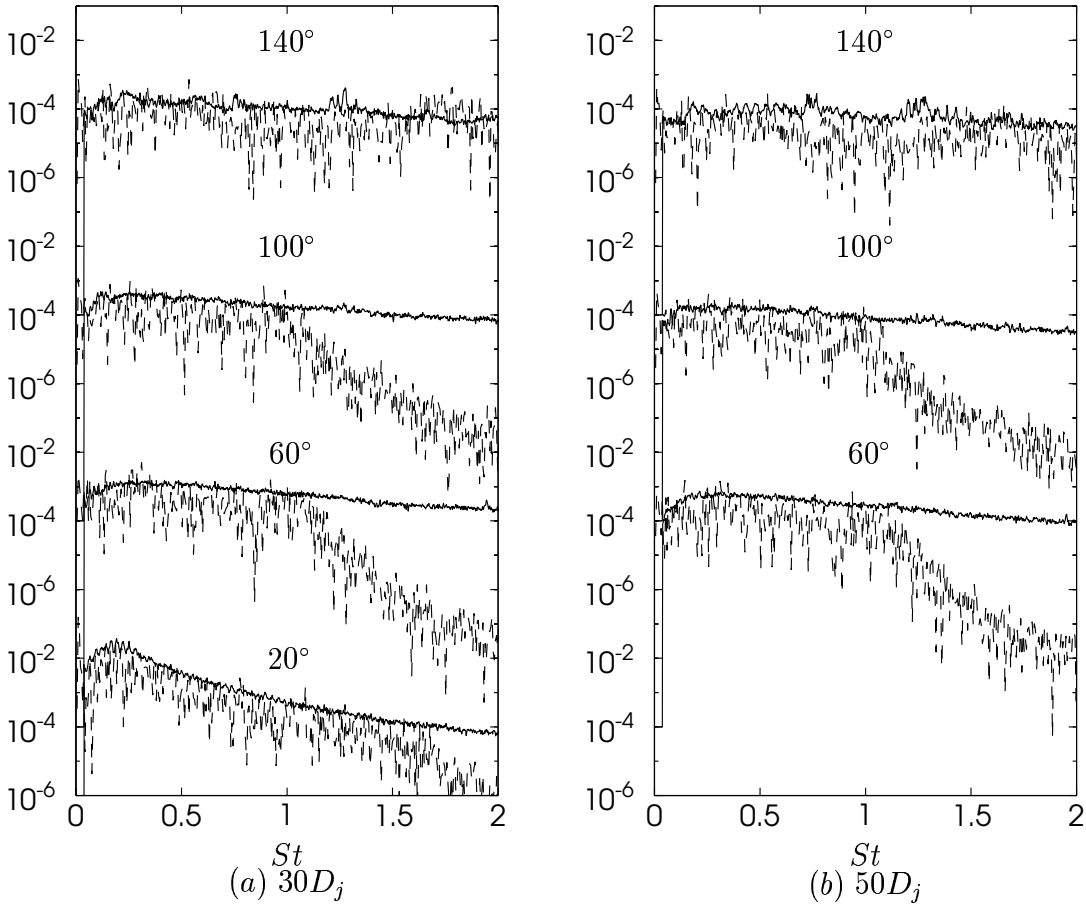

Figure 7.32: Power spectrum of far-field pressure fluctuations versus Strouhal number, $St = fD_j/U_j$. The dashed line, $' \; - - \; '$, corresponds to data obtained using Kirchhoff integration and the solid line corresponds to experimental data measured by Jordan *et al.* (2002*b*). In figure (a), four observer locations are represented. Starting at a location 20° from the x-axis, the angle is increased by an increment of 40° per spectrum. In figure (b) the first spectrum from below is obtained for an observer location 60° from the x-axis, i.e. it should be compared with the second spectrum from below in figure (a). Note that the spectra have been staggered and the scale on the y-axis is therefore repeated.

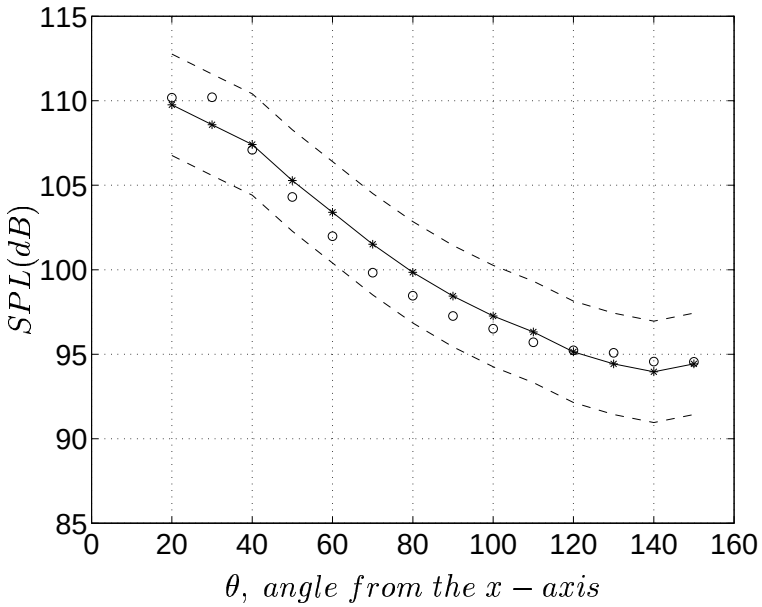

Figure 7.33: Far-field sound pressure levels in microphone locations $30D_j$ from the nozzle exit. The sound pressure levels were obtained using band-pass filtered pressure signals. The upper cut-off frequency corresponds to $St = 1.0$ and the lower to $St = 0.05$. See also legend to figure 7.30.

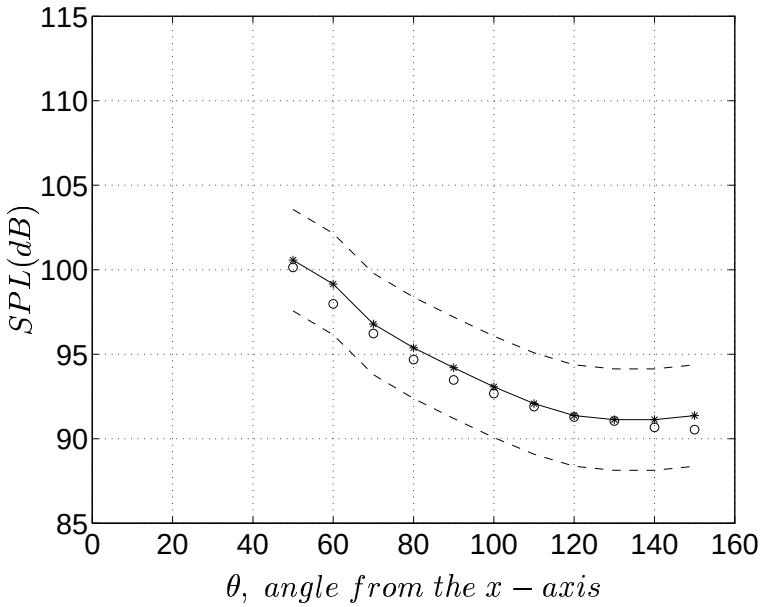

Figure 7.34: Far-field sound pressure levels in microphone locations $50D_j$ from the nozzle exit. The sound pressure levels were obtained using band-pass filtered pressure signals. The upper cut-off frequency corresponds to $St = 1.0$ and the lower to $St = 0.05$. See also legend to figure 7.30.

7.2 Mach 0.75, Heated Jet (*Jet II*)

A heated version of the jet presented in the previous section was simulated in order to investigate whether the methods used predict jet aerodynamics and radiated sound within satisfying ranges when temperature effects are present. The static temperature of the jet exhaust was in this case twice that of the surrounding ambient air in which the jet is developed.

7.2.1 Instantaneous Flow Field

As in chapter 7.1.1, vorticity was visualized by isosurfaces of negative second eigenvalues of $(S_{ik}S_{kj} + \Omega_{ik}\Omega_{kj})$, see figure 7.35. The same isosurface values as in figure 7.1 were used. By comparing the figures of *Jet I* and those of *Jet II* it seems that heating the jet results in more small-scale structures in the initial jet region. Moreover, the break-up of the jet is faster than in the unheated case. This results in a shorter potential core region, which will be shown in the time-averaged profiles later. Figure 7.36 shows contours of axial velocity in a in the xz-plane

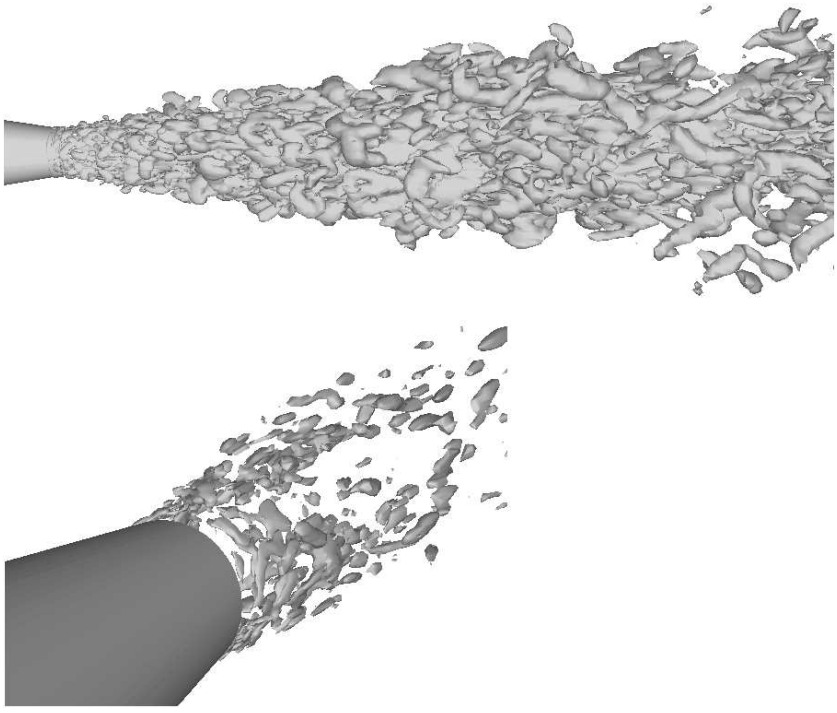

Figure 7.35: Isosurface of negative second eigenvalues of $A_{ij} = (S_{ik}S_{kj} + \Omega_{ik}\Omega_{kj})$.

and in the yz-plane. The three-dimensionality of the jet flow is clearly visualized in the right figure.

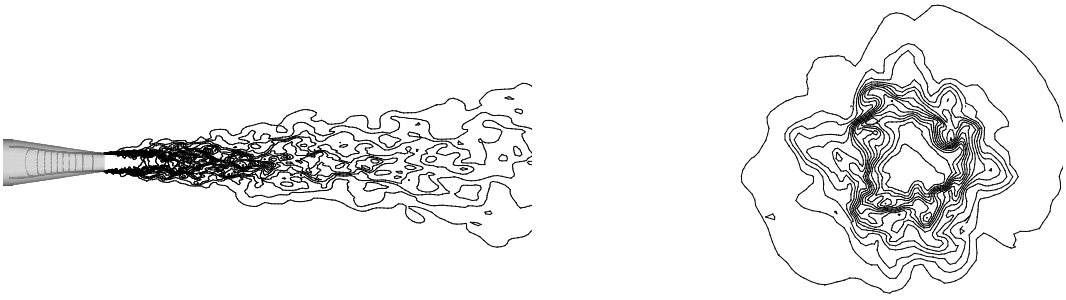

Figure 7.36: Contours of instantaneous axial velocity. The left picture shows contours in the plane $y = 0.0$ and the right picture in the plane $x = 0.15$.

7.2.2 Time-averaged Velocity Profiles

Figure 7.37 shows how radial profiles of axial velocity develop downstream. Figures 7.38–7.44 are comparisons of the predicted time-averaged initial flow field, i.e. the flow in vicinity of the nozzle, of *Jet II* with experimental data (Jordan *et al.*, 2002*a*). Profiles of mean velocity and turbulence intensities were extracted along the radial and axial lines depicted in figure 7.4. Note that all radial profiles have been staggered corresponding to their axial position in order to visualize the downstream jet development. As for *Jet I*, the predicted jet flow field is in very good agreement with the measured flow field.

It is obvious from figure 7.38 that, for the heated jet, as for the cold jet discussed in the previous section, the potential core is shorter than that obtained in the experiments. Using the criterion presented in section 7.1.2, the potential core is 4.0 D_j for the LES data and 5.0 D_j for the experimental data. However, the trend is correctly predicted, i.e. heating the jet results in a shorter core region.

The fact that the potential core is shorter makes the radial velocity profiles obtained from the LES flatter than those obtained in the experiments, downstream of the predicted potential core closure, see figure 7.39. The initial jet spreading is slightly overpredicted, which can be seen in figure 7.39.

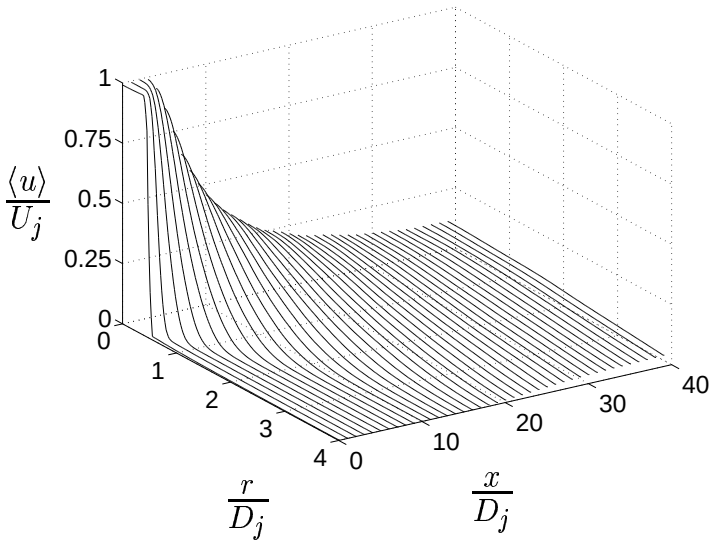

Figure 7.37: Downstream development of radial profiles of axial velocity.

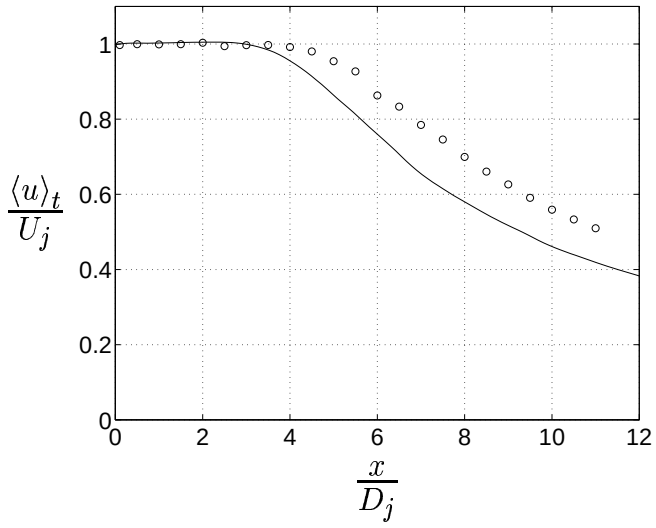

Figure 7.38: Centerline velocity: the solid line, $'-'$, corresponds to LES results and the circles, $'o'$, to experimental data (Jordan *et al.*, 2002*a*).

The maximum level of the root-mean-square of axial velocity is in good agreement with experiments. The location of the maximum is shifted towards the nozzle, however, since this maximum occurs at the potential core closure, see figure 7.40. The radial profiles of the root-mean-square of axial velocity depicted in figure 7.41 show the overprediction of the initial mixing of the jet. The profile of LES data closest to the nozzle outlet is wider than the corresponding measured profile.

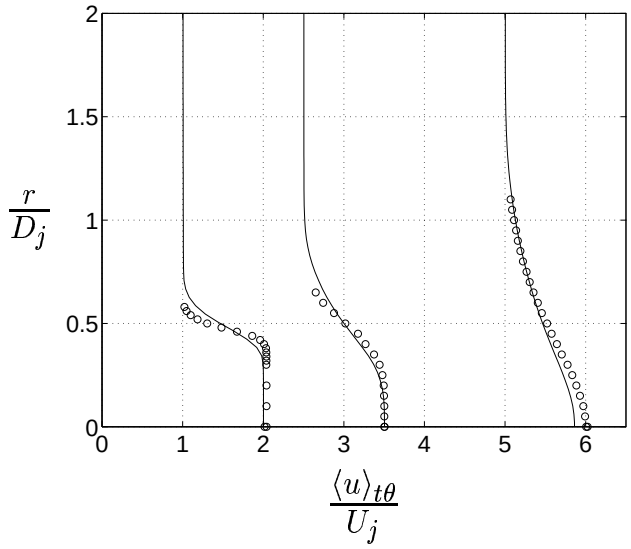

Figure 7.39: Radial profiles of axial velocity at axial positions $x/D_j = 1.0$, $x/D_j = 2.5$ and $x/Dj = 5.0$: $'-'$ correspond to LES results and $'o'$ to experimental data (Jordan *et al.*, 2002*a*). The profiles have been staggered corresponding to their axial position.

Furthermore, the maximum level, located in the center of the shear layer, is higher for the LES profile. Moving downstream, the difference in peak value decreases and, for the profile farthest downstream, i.e. $x = 5.0D_j$, the peak value is even underpredicted.

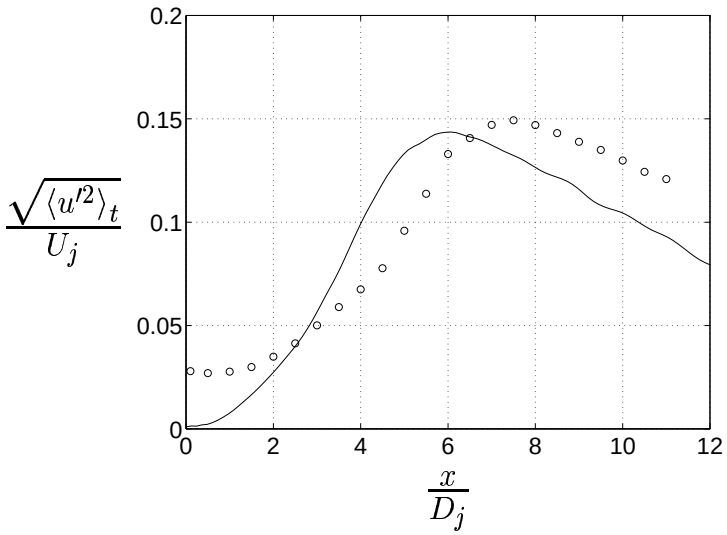

Figure 7.40: Axial profile of $\sqrt{\langle u'^2 \rangle_t}$: $'-'$ corresponds to LES results and $'o'$ to experimental data (Jordan *et al.*, 2002*a*).

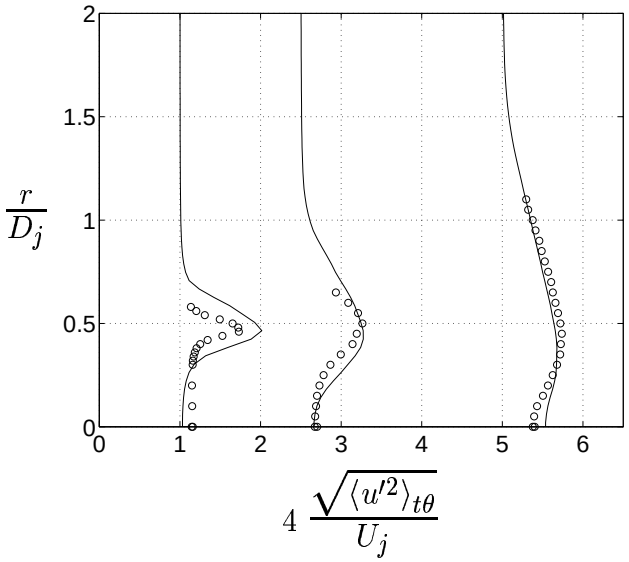

Figure 7.41: Radial profiles of $\sqrt{\langle u'^2\rangle_{t\theta}}$ at $x/D_j = 1.0$, $x/D_j = 2.5$ and $x/D_j = 5.0$: $'-'$ corresponds to LES results and $'o'$ to experimental data (Jordan *et al.*, 2002*a*). The profiles have been staggered corresponding to their axial position.

The peak level of the root-mean-square of radial velocity is, as the axial velocity, in good agreement with measurements but shifted upstream, see figure 7.42. The turbulence anisotropy of the jet is well captured in the LES, which can be seen if the profiles of the root-mean-square of axial velocity are compared with the corresponding profiles for the radial velocity component. As for the cold jet, the root-mean-square of measured radial velocity is rather high close to the nozzle, which is probably caused by potential core flutter in the experiments. These high levels can also be seen in the first radial profile in figure 7.43. These profiles are, despite the differences close to the nozzle, in rather good agreement with experiments.

In figure 7.44, predicted radial profiles of the uv correlation are compared with experiments. The uv correlation gives an estimate of the mixing in the jet flow. Since previous figures have shown that the potential core is shorter in the LES than in experiments, and hence the rate of mixing is higher, it is natural that the uv correlation in this region is overpredicted. Moving downstream, the predicted values are to a higher degree aligned with the measurement data. However, the location of maximum shear is somewhat shifted towards the centerline.

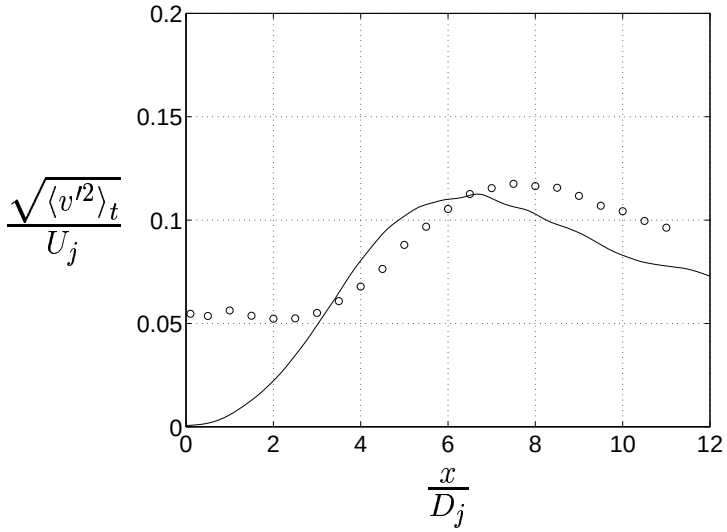

Figure 7.42: Axial profile of $\sqrt{\langle v'^2\rangle_t}$: $'-'$ corresponds to LES results and $'o'$ to experimental data (Jordan *et al.*, 2002*a*).

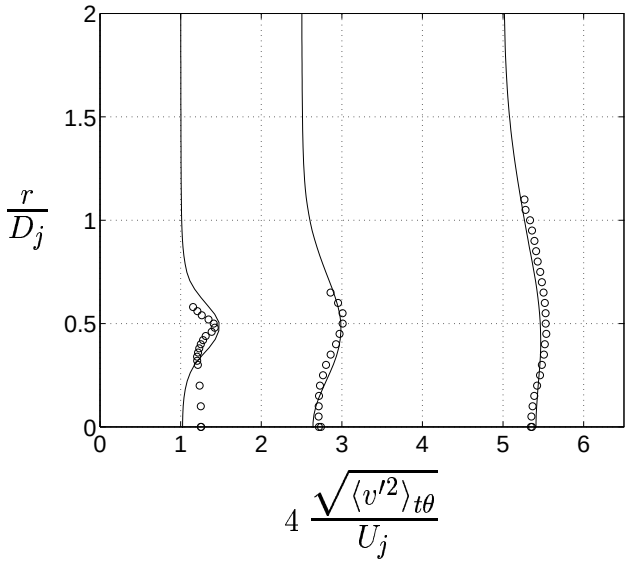

Figure 7.43: Radial profiles of $\sqrt{\langle v'^2\rangle_{t\theta}}$ at $x/D_j = 1.0$, $x/D_j = 2.5$ and $x/D_j = 5.0$: $'-'$ corresponds to LES and $'o'$ to experimental data (Jordan *et al.*, 2002*a*). The profiles have been staggered corresponding to their axial position.

7.2.3 Temperature Profiles

No measurements of temperature were conducted, which means that no experimental data are available for validation of LES results. However, it is most likely that the results obtained from the LES agree to

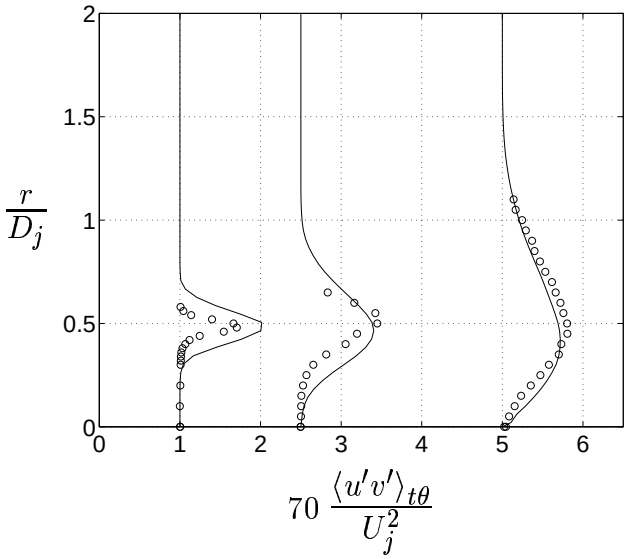

Figure 7.44: Radial profiles of $\langle u'v' \rangle_{t\theta}$ at $x/D_j = 1.0$, $x/D_j = 2.5$ and $x/D_j = 5.0$: $'-'$ corresponds to LES and $'o'$ to experimental data (Jordan *et al.*, 2002*a*). The profiles have been staggered corresponding to their axial position.

the same extent with the real jet as the velocity data did. Profiles of time-averaged temperature were obtained in the same locations as the velocity profiles presented in previous section. The radial profiles have, again, been staggered according to their axial position. The profiles in figures 7.45–7.48 have been non-dimensionalized using the jet exhaust temperature, T_j, and velocity, U_j, and the temperature of the surrounding fluid, T_∞.

Figure 7.45 shows the centerline temperature decay and, for comparison, the decay of axial velocity at the centerline is included. The decrease in temperature starts earlier than that of the axial velocity. Furthermore, the temperature decay initially follows a steeper curve than the axial velocity does. These observations have also been made in experiments; see for example Hinze (1975). The axial distribution of the intensity of temperature fluctuations is depicted in figure 7.46. For comparison, the intensity of the axial velocity fluctuations is included. Radial profiles of time-averaged temperature and temperature fluctuation intensity are depicted in figures 7.47 and 7.48, respectively. As for the axial profiles, the corresponding profiles of axial velocity are included for comparison.

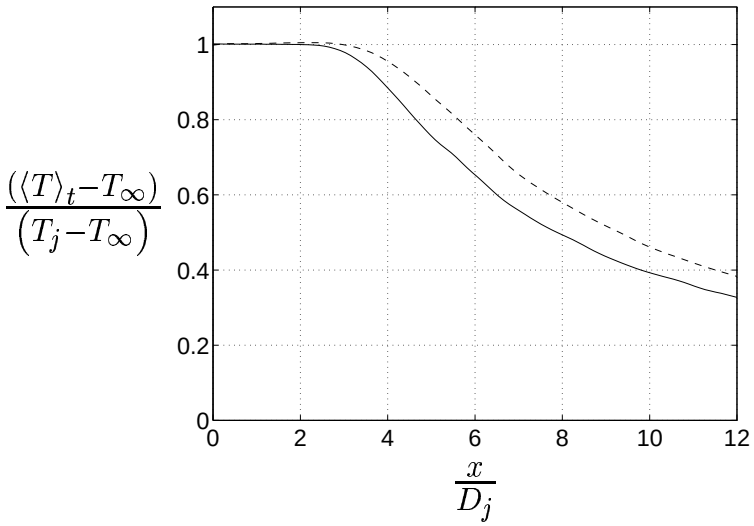

Figure 7.45: Axial profile of time-averaged temperature. For comparison, a profile of axial velocity is included. The solid line denotes temperature and the dashed line axial velocity.

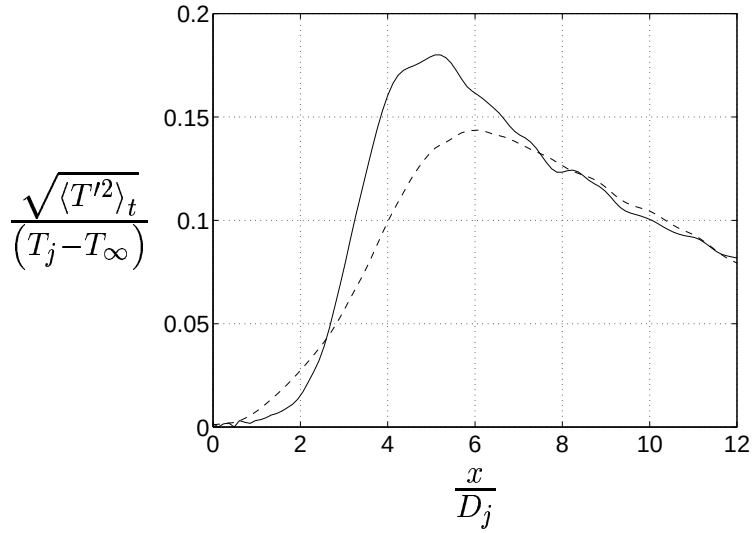

Figure 7.46: Axial distribution of the temperature fluctuation intensity. A profile of the intensity of the axial velocity fluctuation is included for comparison (dashed line).

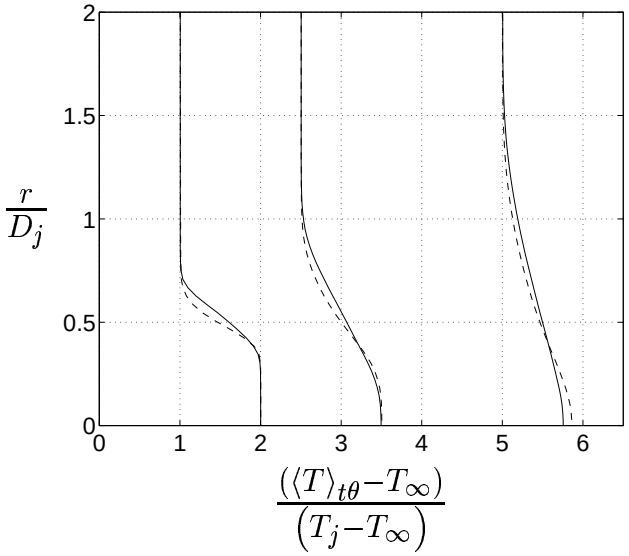

Figure 7.47: Radial profiles of time and azimuthally averaged temperature. For legend see figure 7.45.

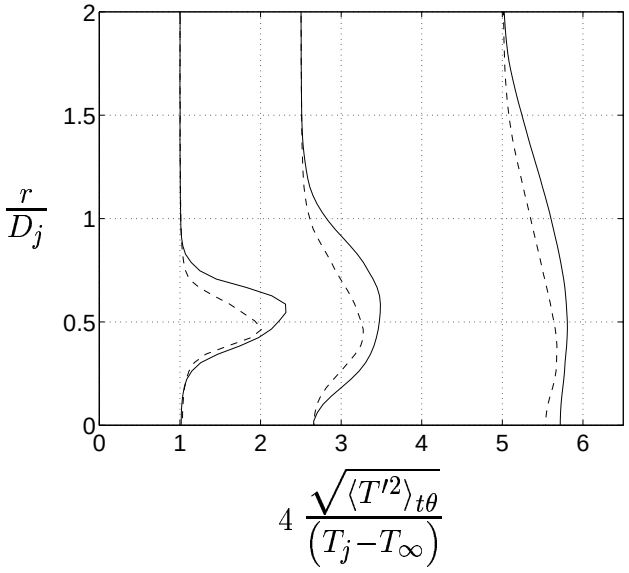

Figure 7.48: Radial distribution of temperature fluctuation intensity. For legend see figure 7.46.

7.2.4 Self-preservation

An investigation of whether the velocity profiles and second-order moments show self-preserving behavior was made in the same manner as for the unheated jet, see section 7.1.3. In figure 7.49, the inverse of time-averaged centerline velocity normalized by the jet exit velocity is plotted verses the axial coordinate normalized by the nozzle diameter. The intersection of a line fitted to the LES data and the x-axis, i.e. the axial location from which the self-preserving jet seems to originate, x_0 =1.05 D_j, is used to collapse radial profiles of axial velocity and second-order moments, see figures 7.50–7.54. As discussed in section 7.1.3, the axial extent of the domain is too short to fully obtain self-similar behavior of second-order moments. However, the axial velocity becomes self-similar within the two-meter domain used for evaluation. As for *Jet I*, it seems that self-similar behavior of correlations including axial velocity components is more difficult to obtain than for those only including radial and tangential velocity components. The jet spreading rate was estimated from a curve fitted to the collapsed profiles of axial velocity to be roughly 0.095, see figure 7.50.

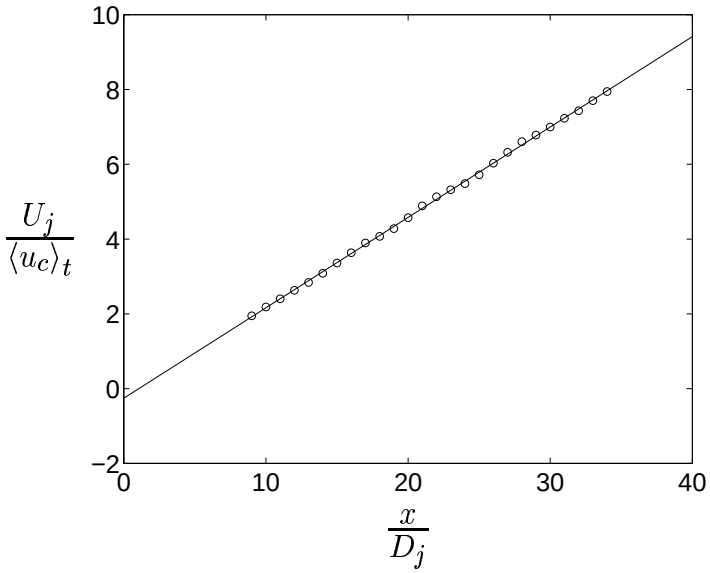

Figure 7.49: Predicted centerline velocity. The solid line corresponds to a curve fit to the LES data. The x-value at which the line intersects the x-axis, x_0, is used to collapse the radial profiles in figures 7.50–7.54.

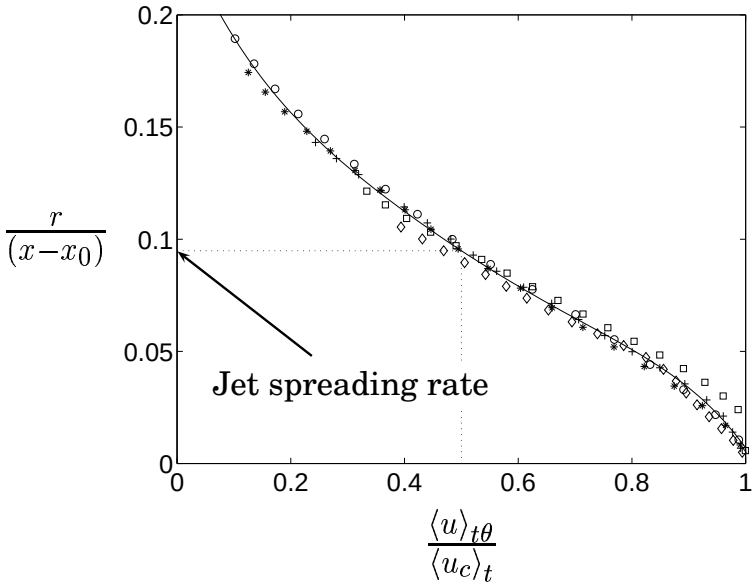

Figure 7.50: Radial profiles of axial velocity normalized by centerline mean velocity. The solid line corresponds to a curve fit to the LES data. The profiles are labeled as follows: $' \circ ' = 19D_j$, $' * ' = 24D_j$, $' + ' = 29D_j$, $' \square ' = 34D_j$ and $' \diamond ' = 39D_j$.

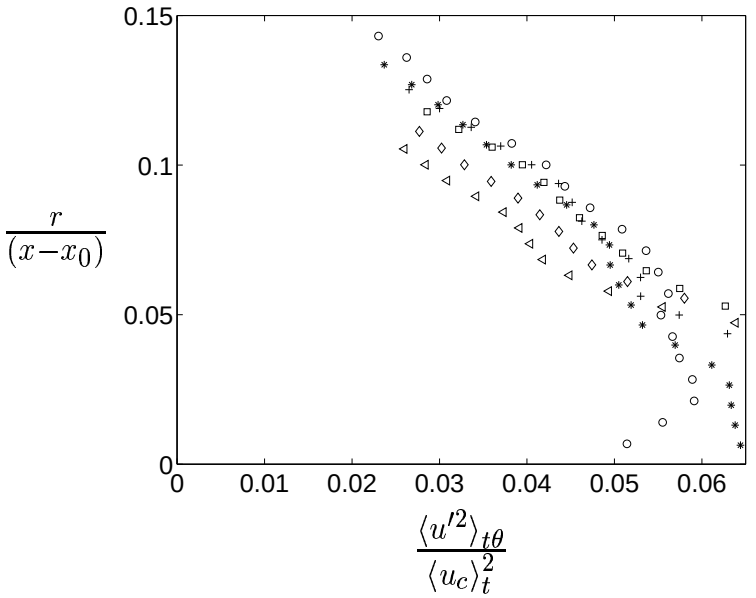

Figure 7.51: Radial profiles of $\langle u'u' \rangle_{t\theta}$ normalized by centerline mean velocity. Radial profiles at six axial locations are represented. The profiles are labeled as follows: $' \circ ' = 29D_j$, $' * ' = 31D_j$, $' + ' = 33D_j$, $' \square ' = 35D_j$, $' \diamond ' = 37D_j$ and finally $' \triangleleft ' = 39D_j$.

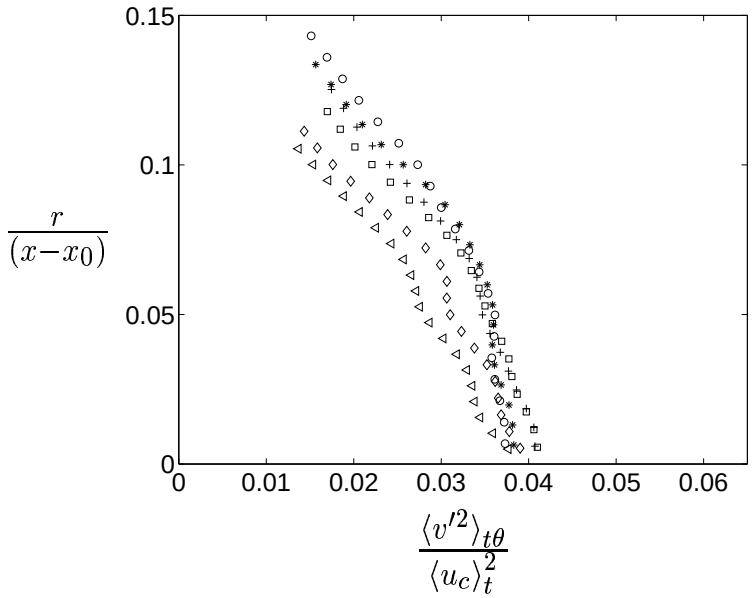

Figure 7.52: Radial profiles of $\langle v'v'\rangle_{t\theta}$ normalized by centerline mean velocity. For legend see figure 7.51.

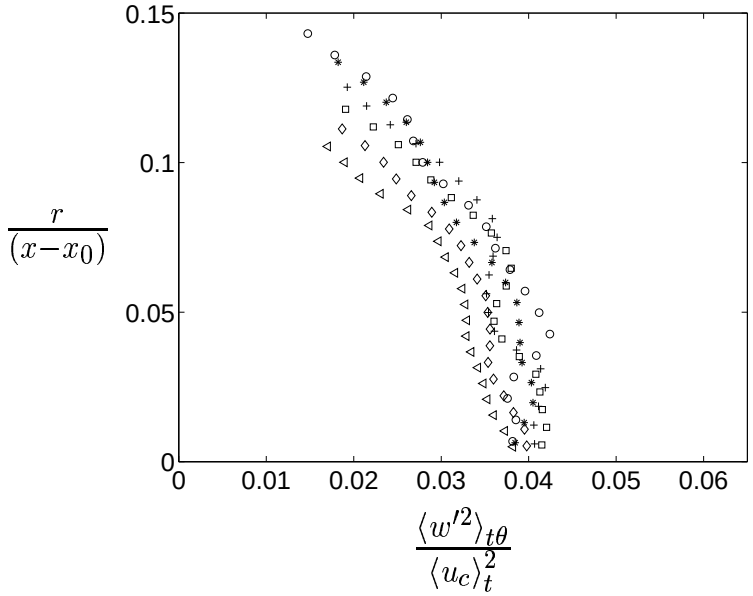

Figure 7.53: Radial profiles of $\langle w'w'\rangle_{t\theta}$ normalized by centerline mean velocity. For legend see figure 7.51.

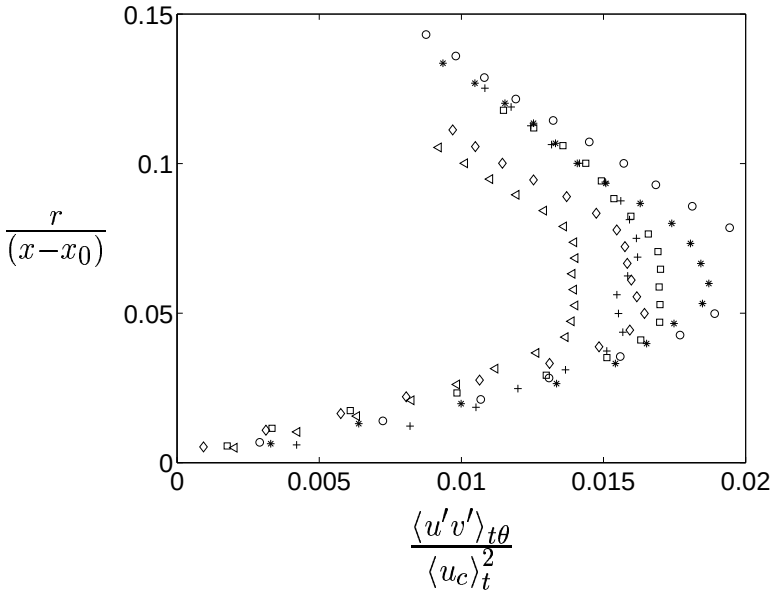

Figure 7.54: Radial profiles of $\langle u'v' \rangle_{t\theta}$ normalized by centerline mean velocity. For legend see figure 7.51.

7.2.5 Two-point Space-time Correlations

Two-point space-time correlations were obtained for a number of shear layer locations at $r = 0.5D_j$. The methodology used was the same as for the unheated jet, see section 7.1.4. The correlations are obtained for the axial velocity component, and the correlation amplitude, R_{uu}, is defined by equation 7.2. The data series used for this evaluation is roughly 7.5×10^{-2} $[s]$. Figures 7.55–7.57 show correlation curves obtained in three axial locations along the nozzle lip line. The increase in spatial separation, ξ, for each curve in the figures is $0.1D_j$. The correlations were obtained using an increment in temporal separation, $\Delta\tau$, of 1.5×10^{-6} $[s]$. Figure 7.58 shows contours of correlation amplitude

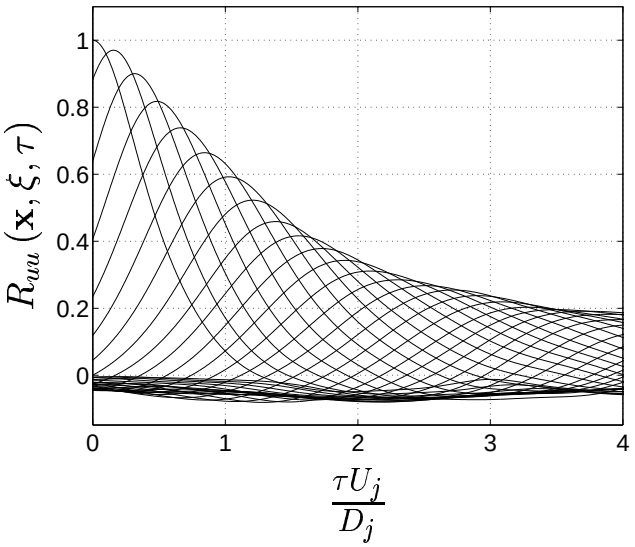

Figure 7.55: Two-point space-time correlation of axial velocity at a location, x, in the shear layer $r = 0.5D_j$, $x = 2.5D_j$. Each curve corresponds to a two-point space-time correlation obtained using a certain spatial separation, ξ. Starting with no separation in space, i.e. the autocorrelation, the spatial separation is increased by $0.1D_j$ per curve.

in the $\xi\tau$-plane. The correlations presented in this figure are obtained in the shear layer, $r = 0.5D_j$, at an axial location corresponding to the potential core closure, $x = L_c = 4.0D_j$. The correlation peak for each spatial separation of the predicted correlations is indicated with a circle in the figure. Peaks of correlations obtained from data measured by Jordan (2003) are represented by stars. The envelope of predicted two-point space-time correlation curves and the predicted autocorrelation in the shear layer location corresponding to the end of the potential core are compared with the corresponding correlations of measured data in figure 7.59. Spatial correlations obtained in the same three

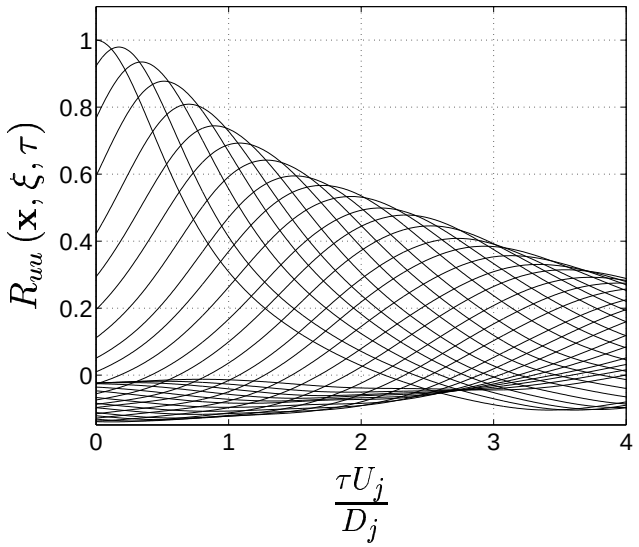

Figure 7.56: Two-point space-time correlation of axial velocity at a location, x, in the shear layer $r = 0.5D_j,\ x = 5.0D_j$. See also legend to figure 7.55.

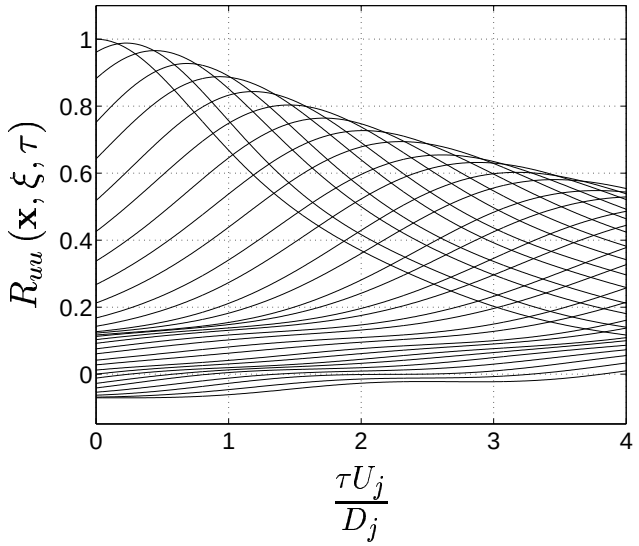

Figure 7.57: Two-point space-time correlation of axial velocity at a location, x, in the shear layer $r = 0.5D_j,\ x = 10.0D_j$. See also legend to figure 7.55.

axial locations as the space-time correlations presented earlier are depicted in figure 7.60. In figure 7.61, predicted spatial correlations in location ($x = L_c$, $r = 0.5D_j$) are compared with the spatial correlations of measured data obtained for the corresponding location.

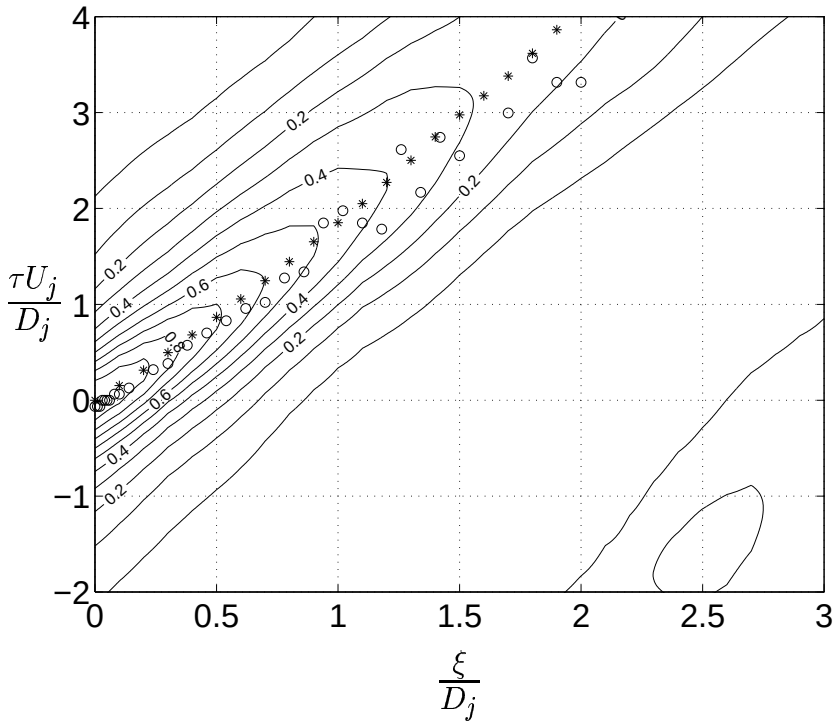

Figure 7.58: Contours of $R_{uu}(\mathbf{x}, \xi, \tau)$ obtained in the shear layer, $r = 0.5D_j$, at the end of the potential core, $x = L_c = 4.0D_j$. The contours corresponds to LES data. $' * '$ corresponds to the correlation peaks of these two-point space-time correlations and $' \circ '$ to the peaks of the correlations of the velocity data measured by Jordan (2003).

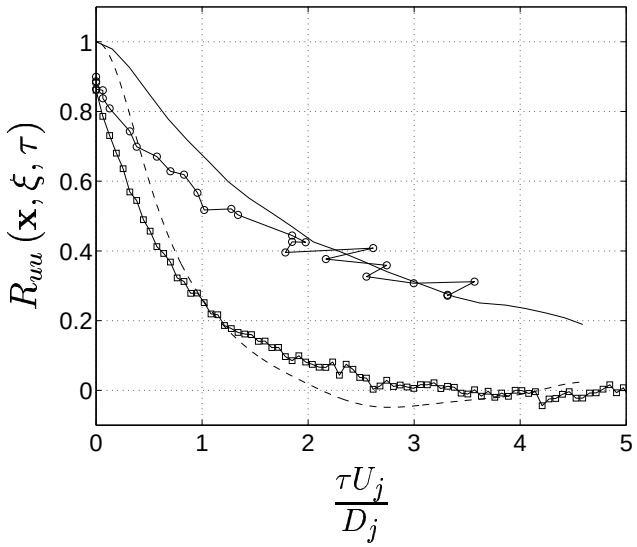

Figure 7.59: Comparison of the autocorrelation and correlation envelope for the LES data and the measured data. The data are in both cases obtained in the shear layer at the potential core closure ($x = L_c$). The solid line denotes the envelope of the LES data and the solid line with circles the corresponding measured data. The dashed line corresponds to the autocorrelation of the LES data and the solid line with squares denotes the autocorrelation of the data measured by Jordan (2003).

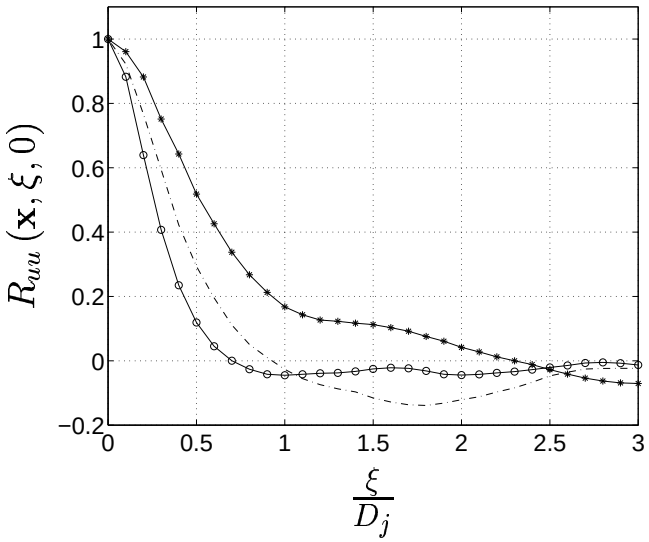

Figure 7.60: Predicted two-point correlation of axial velocity at three different locations, x, in the shear layer: $'-o'$ corresponds to a location $x = 2.5D_j$ downstream of the nozzle exit, $'-\cdot'$ to $x = 5.0D_j$ and $'-*'$ to $x = 10D_j$. All points are located at $r = 0.5D_j$.

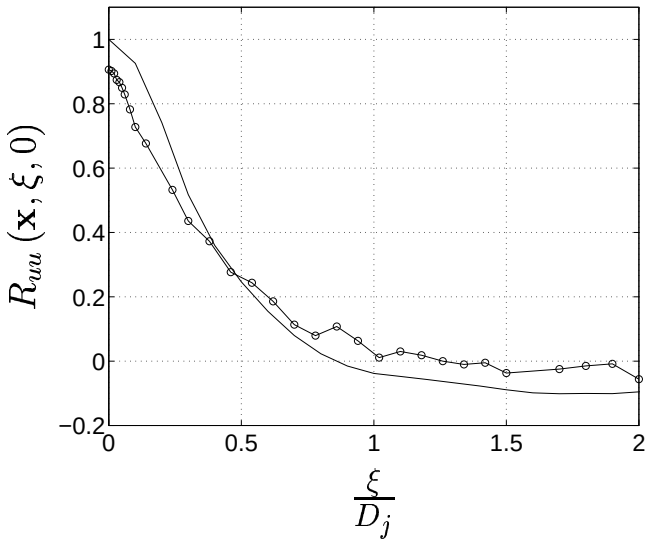

Figure 7.61: Comparison of spatial correlation in the shear layer at the potential core closure. The solid line denotes LES data and the solid line with circles data measured by Jordan (2003).

7.2.6 Length and Time Scales of Turbulence Structures

Integral length and time scales and convection velocity of turbulence structures were obtained from the two-point space-time correlations presented in the previous section. The first crossing of the ξ-axis for the spatial correlations and of the τ-axis for the autocorrelations were used as the upper limit for the integration when obtaining the integral scales. Figures 7.62–7.64 show the axial development of predicted integral length and time scales in the shear layer along the nozzle lip line. For comparison, the corresponding scales obtained from measured data for a few axial locations are included.

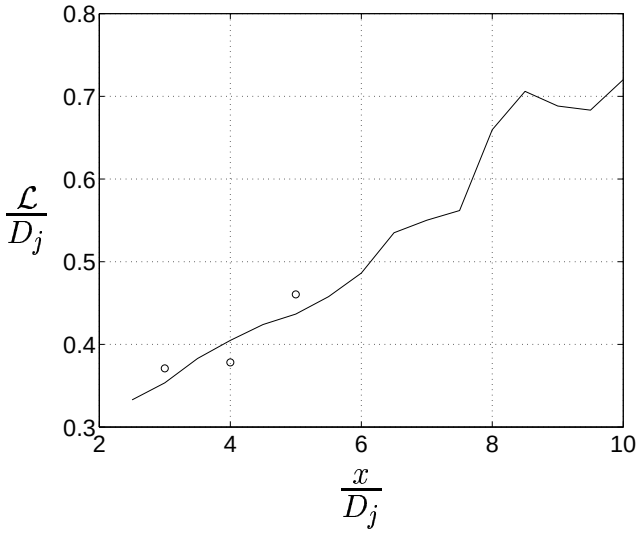

Figure 7.62: Axial development of the integral length scale in the shear layer, i.e. $r = 0.5D_j$. $'\circ'$ denotes experiments (Jordan, 2003).

Estimates of turbulence convection velocity were obtained using the temporal separation corresponding to the peak of the correlation curve obtained for a spatial separation of $\xi = 0.1D_j$, see figure 7.26. The predicted velocities for a few axial locations are presented in table 7.2. In the middle column, the convection velocities have been normalized by the jet exit velocity. These values are, for most of the locations, close to the value of 0.6 often referred to in the literature as the correct convection velocity. In the right column, the velocities are normalized by the local mean velocity. The eddy velocity is everywhere slightly higher than the local mean velocity, which was also found for the unheated jet. For a more detailed discussion of whether this could be considered

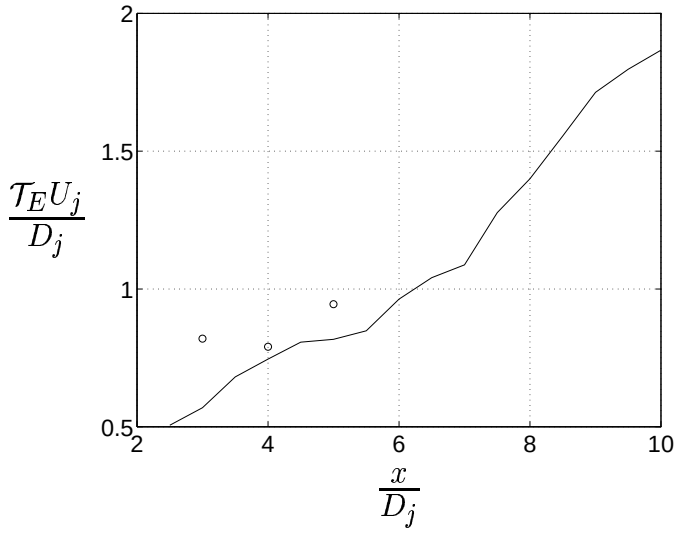

Figure 7.63: Axial development of the Eulerian integral time scale in the shear layer, i.e. $r = 0.5D_j$. For legend see figure 7.62.

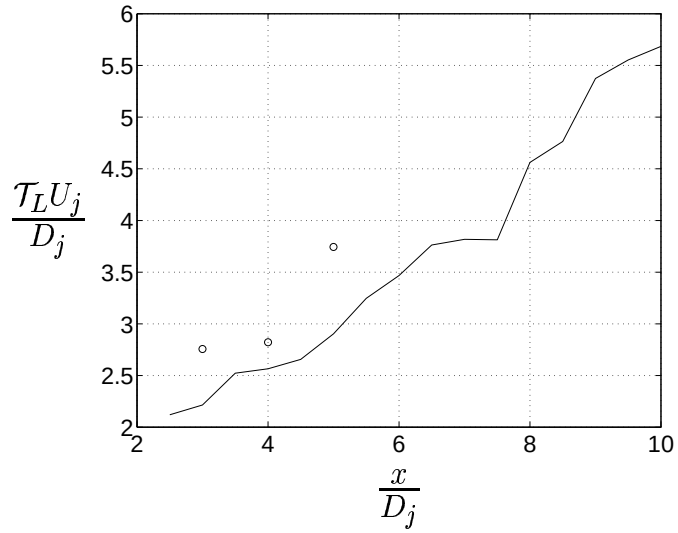

Figure 7.64: Axial development of the Lagrangian integral time scale in the shear layer, i.e. $r = 0.5D_j$. For legend see figure 7.62.

a reasonable result, see section 7.1.5.

x/D_j	U^c/U_j	$U^c/\langle u \rangle_t$
2.50	0.65	1.27
3.00	0.65	1.28
3.50	0.65	1.30
4.00	0.65	1.32
4.50	0.65	1.36
5.00	0.59	1.25
5.50	0.62	1.34
6.00	0.57	1.24
6.50	0.62	1.39
7.00	0.59	1.36
7.50	0.54	1.27
8.00	0.54	1.32
8.50	0.54	1.36
9.00	0.52	1.34
9.50	0.50	1.33
10.00	0.44	1.20

Table 7.2: Convection velocity of turbulence structures in the shear layer, $r = 0.5D_j$.

7.2.7 Far-field Sound Pressure Levels

Levels of radiated sound in the far-field microphone locations depicted in figure 6.5 were obtained from the LES and validated against experimental data. The predicted pressure signal used for the evaluation is roughly 2.30×10^{-2} $[s]$. The observer pressure signals were obtained using Kirchhoff surface integration. Predicted overall sound pressure levels (OASPL) are presented in figures 7.65–7.66. The predicted levels are for all angles within the 3dB deviation from the measured levels indicated by the dashed lines in the figures. This is a very satisfying result but can be further improved by filtering the data to remove frequencies that are non-physical or can not be represented by the mesh and the numerical method used. As discussed in section 7.1.6, the deviations for low angles for the lower arc are probably due to the fact that the Kirchhoff surface used, for these angles, is very close to the observers. Power spectra of far-field pressure fluctuations are presented

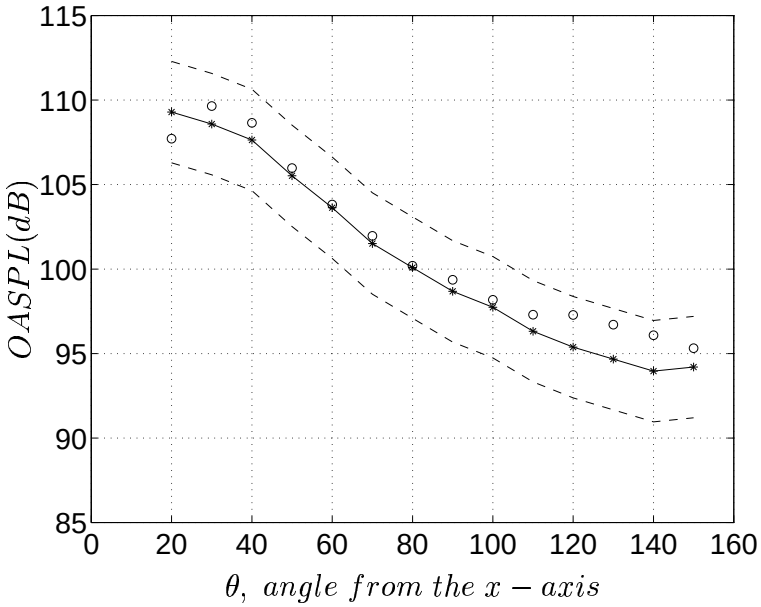

Figure 7.65: Far-field sound pressure levels in microphone locations $30D_j$ from the nozzle exit: $'-*'$ corresponds to sound pressure levels measured by Jordan *et al.* (2002*b*) and the dashed lines, $'--'$, to the measured levels $\pm$ 3dB. $'o'$ denotes calculated sound pressure levels using Kirchhoff surface integration.

in figure 7.67. For low frequencies, the spectra are well captured by the LES whereas, for higher frequencies ($St > 1.0$), the predicted am-

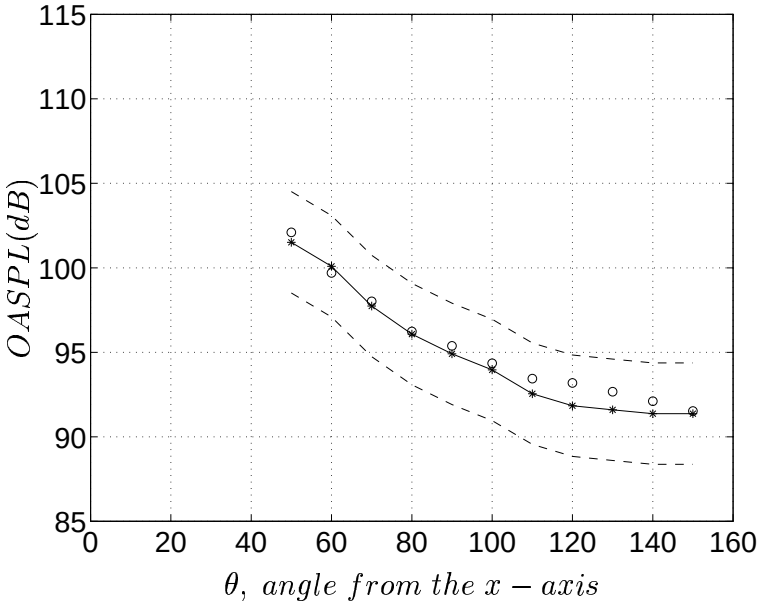

Figure 7.66: Far-field sound pressure levels in microphone locations $50D_j$ from the nozzle exit. See also legend to figure 7.65.

plitudes fall off rapidly and are far below the measured ones. This is an effect of having too poor grid resolution in the surface region to be able to support acoustic waves of higher frequencies. This means that the mesh itself acts as a low-pass filter as the acoustic waves propagate through the domain. This effect is especially noticeable for the intermediate angles, where the mesh, due to the resolution demands at the jet exit, is very coarse, see figure 6.3. Furthermore, as can be seen from figure 7.67, the spectrum peak for the 20° observer is not captured. This leads to an underprediction of the sound pressure level for this observer, which can be seen in figure 7.65. The reason for this underprediction might be the location of the Kirchhoff surface.

As was done for *Jet I*, see section 7.2.7, the observer pressure signals was band-pass filtered to investigate the possibility of decreasing the deviation in SPL for upstream observers by removing high frequencies. The overprediction of high frequencies might be caused by non-physical waves that to some extent propagate upstream since the mesh in this region is significantly finer than in the downstream direction. As can be seen in figures 7.68–7.69, filtering gives sound pressure levels closer to the measured levels for the upstream observers. For the 20° observer, removing high frequencies does not improve the sound pressure level

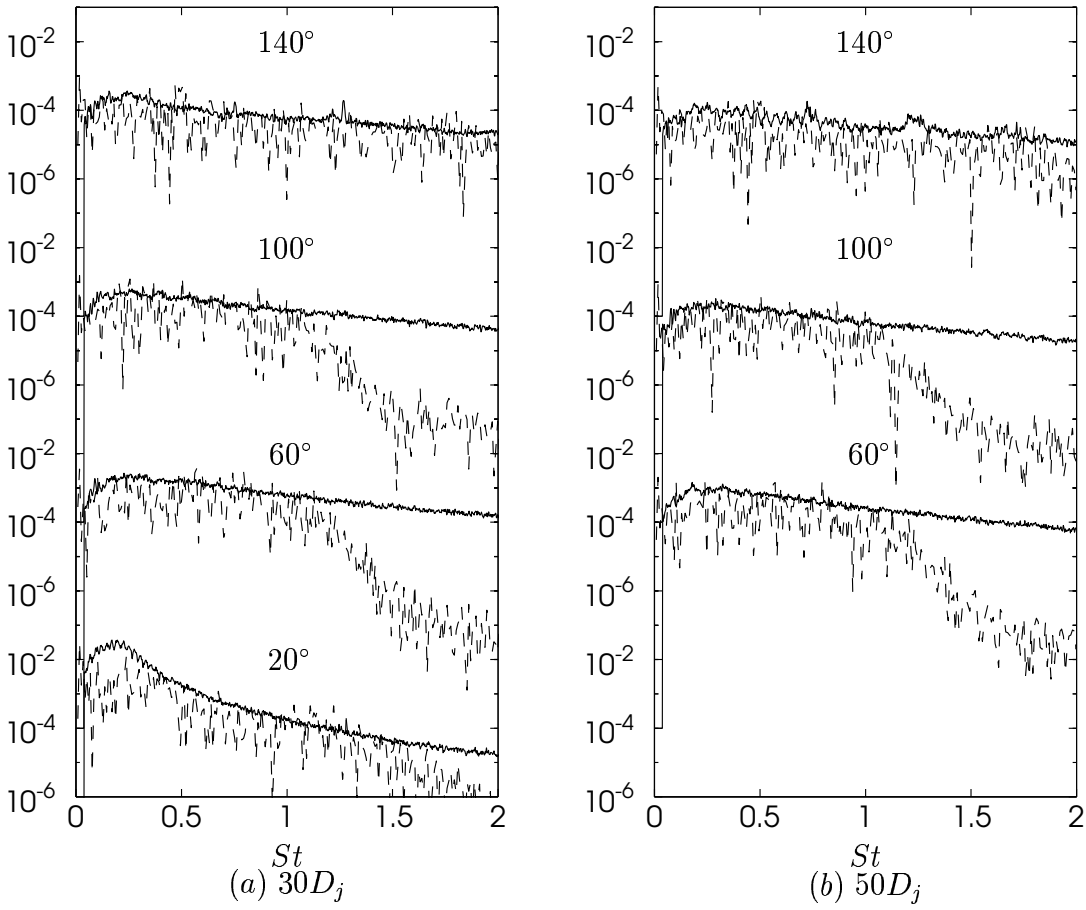

Figure 7.67: Power spectrum of far-field pressure fluctuations versus Strouhal number, $St = fD_j/U_j$. The dashed line, $' \; - - \; '$, corresponds to data obtained using Kirchhoff integration and the solid line corresponds to experimental data measured by Jordan *et al.* (2002*b*). In figure (a), four observer locations are represented. Starting at a location 20° from the x-axis, the angle is increased by an increment of 40° per spectrum. In figure (b), the first spectrum from below is obtained for an observer location 60° from the x-axis, i.e. it should be compared with the second spectrum from below in figure (a). Note that the spectra have been staggered and the scale on the y-axis is therefore repeated.

due to the underprediction of low frequencies.

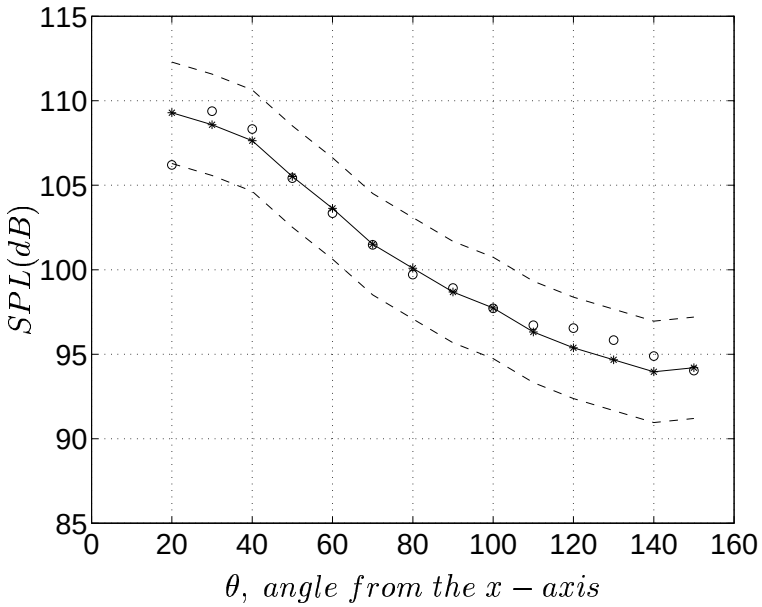

Figure 7.68: Far-field sound pressure levels in microphone locations $30D_j$ from the nozzle exit. The sound pressure levels were obtained using band-pass filtered pressure signals. The upper cut-off frequency corresponds to $St = 1.0$ and the lower to $St = 0.05$. See also legend to figure 7.65.

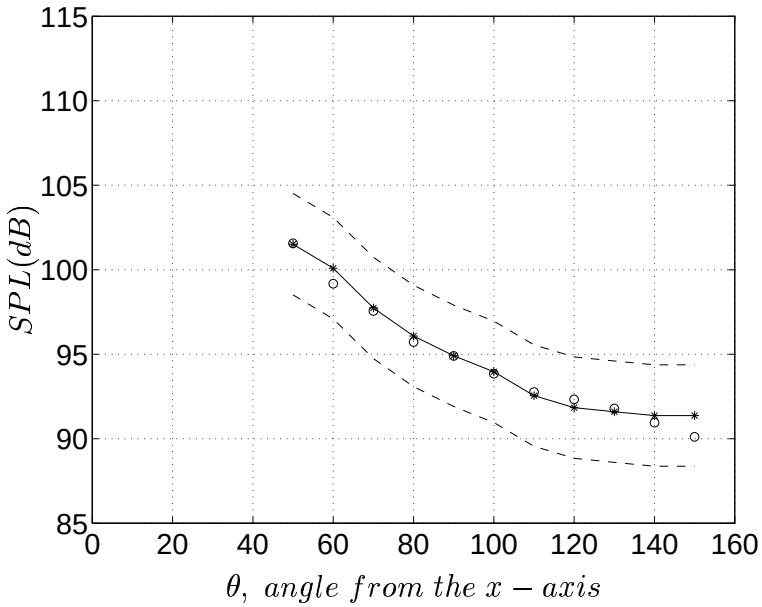

Figure 7.69: Far-field sound pressure levels in microphone locations $50D_j$ from the nozzle exit. The sound pressure levels were obtained using band-pass filtered pressure signals. The upper cut-off frequency corresponds to $St = 1.0$ and the lower to $St = 0.05$. See also legend to figure 7.65.

7.3 Heating Effects on Jet Flow and Radiated Sound

This section discusses the effects of the temperature ratio T_j/T_∞ on the jet flow and sound generation. Starting with a comparison of the instantaneous flow field of the two jets, see section 7.1.1 and section 7.2.1, it seems that the heated jet contains more small-scale structures than the unheated jet in the initial region. Figures 7.1 and 7.35 also show that the heated jet breaks up earlier but does not spread radially to the same extent as the unheated jet. According to Hinze (1975), experiments have indicated that an increasing temperature ratio gives a narrower jet. Furthermore, it has been observed (Hinze, 1975) that the length of the potential core decreases with increased temperature ratio. This is the case for our simulations as well, which justifies the predicted results. The predicted potential core is 4.0 D_j for the heated jet, which should be compared to 5.45 D_j for the unheated jet, see table 7.3. This indicates that the shear layer mixing is higher when the jet has a higher temperature than the surrounding fluid. Comparing profiles of uv correlations, see figures 7.11 and 7.44, the levels for *Jet II* are somewhat higher in the initial region of the jet and the levels are shifted towards the centerline. This again shows that the amount of mixing is higher in the heated jet and that the jet is narrower.

Figure 7.70 shows the axial development of integral length and time scales for *Jet I* and *Jet II*. The axial coordinates has been normalized using the potential core length, L_c of the two jets. Figure 7.71 shows predicted two-point space-time correlation envelopes and autocorrelations in three shear layer locations in the potential core region for *Jet I* and *Jet II*. To be able to compare the two jets, the correlations have been evaluated in locations with the same x/L_c ratio. Figure 7.72 shows the same kind of comparison for spatial correlations. As can be seen in figures 7.70–7.72, there are no great differences in length and time scales for the two jets. However, since the potential core is significantly shorter for *Jet II*, turbulence structures grow faster for this jet.

Table 7.3 gives comparison of length scales, time scales and the convection velocity of turbulence structures obtained from measured and predicted data for *Jet I* and *Jet II*.

Sound pressure levels in far-field observers obtained for *Jet I* and *Jet II* using Kirchhoff surface integration are depicted in figure 7.73. As can be seen from the figure, heating the jet does not have a great affect

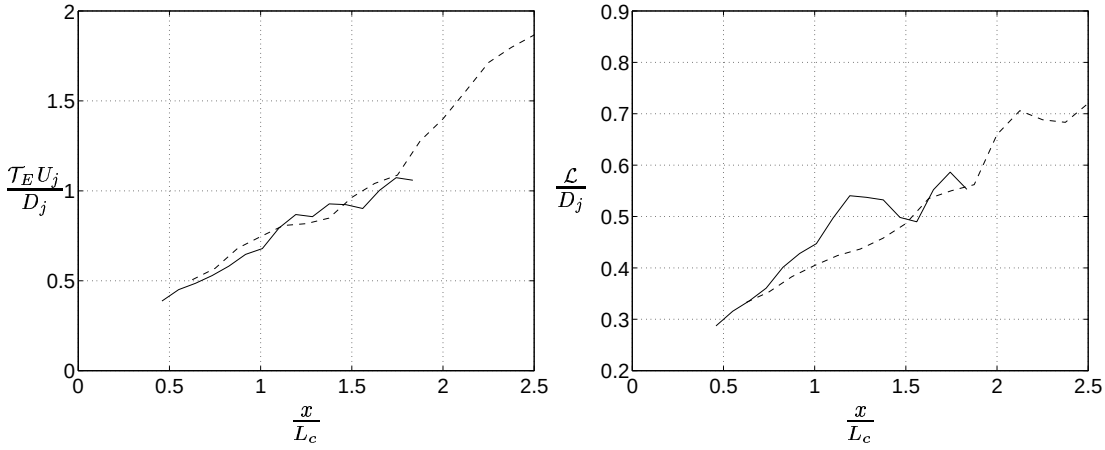

Figure 7.70: Scales of turbulence structures for *Jet I* (solid lines) and *Jet II* (dashed lines) are compared. The axial development of the integral time scale is shown in the left figure and integral length scale in the right figure.

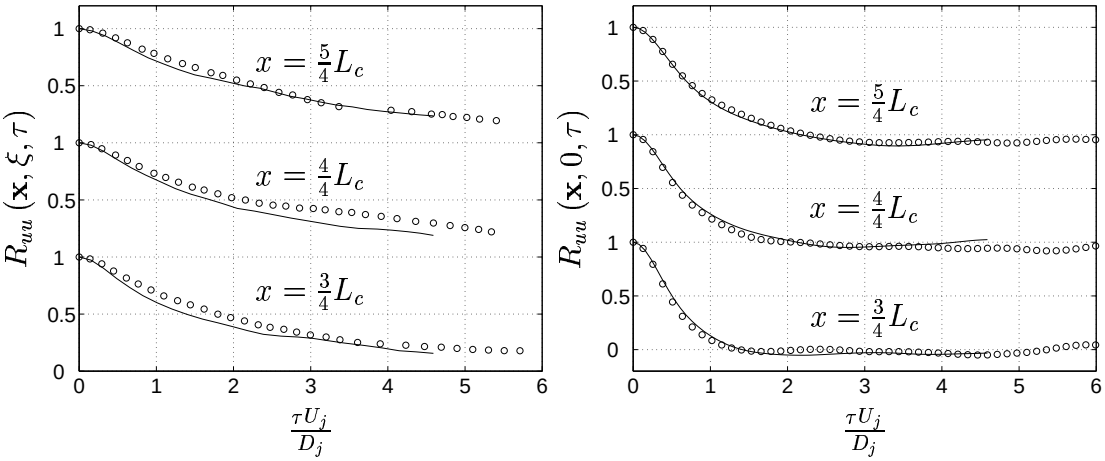

Figure 7.71: In the left figure, the envelope of the predicted two-point space-time correlation curves are compared in three shear layer locations for *Jet I* (circles) and *Jet II* (solid line). In the right figure, predicted autocorrelations in the same positions are compared. (The legend is the same as for the left figure.)

on the sound pressure levels. However, both the predicted and the measured levels are somewhat higher for *Jet II*. Thus the trend seems to be correctly predicted.

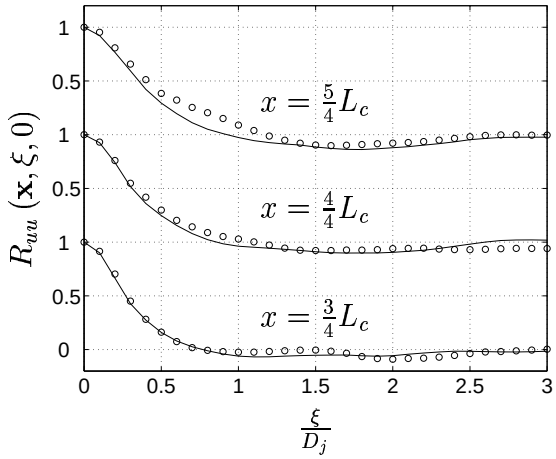

Figure 7.72: Comparison of predicted two-point correlations of axial velocity obtained in three shear layer positions for *Jet I* (circles) and *Jet II* (solid line).

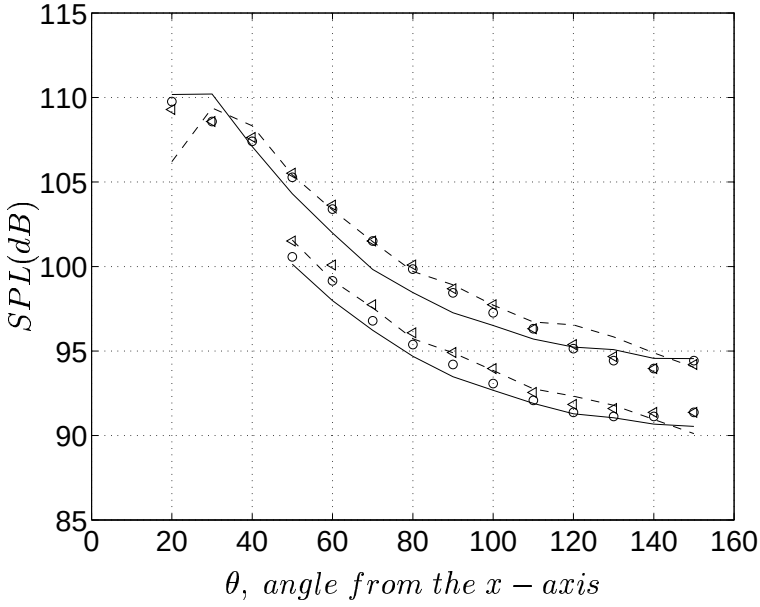

Figure 7.73: Heating effects on radiated sound. Solid and dashed lines denote unheated and heated jet, respectively, and circles and triangles denote the corresponding measured levels. The upper data set is for the $30D_j$ arc and the lower for the $50D_j$ arc. The predicted sound pressure levels are based on band-pass filtered data with a lower cut-off frequency corresponding to $St = 0.05$ and the upper to $St = 1.0$.

Jet I									
	LES			**EXP.**			**LES/EXP.**		
$\frac{L_c}{D_j}$	5.45			6.5			0.84		
x	$\frac{3}{4}L_c$	$\frac{4}{4}L_c$	$\frac{5}{4}L_c$	$\frac{3}{4}L_c$	$\frac{4}{4}L_c$	$\frac{5}{4}L_c$	$\frac{3}{4}L_c$	$\frac{4}{4}L_c$	$\frac{5}{4}L_c$
$\frac{\mathcal{L}}{D_j}$	0.371	0.447	0.538	0.341	0.442	×	1.09	1.01	×
$\frac{\mathcal{T}U_j}{D_j}$	0.542	0.679	0.859	0.664	0.753	×	0.82	0.90	×
$\frac{U^c}{U_j}$	0.71	0.65	0.70	0.78	0.75	×	0.91	0.87	×
Jet II									
	LES			**EXP.**			**LES/EXP.**		
$\frac{L_c}{D_j}$	4.0			5.0			0.80		
x	$\frac{3}{4}L_c$	$\frac{4}{4}L_c$	$\frac{5}{4}L_c$	$\frac{3}{4}L_c$	$\frac{4}{4}L_c$	$\frac{5}{4}L_c$	$\frac{3}{4}L_c$	$\frac{4}{4}L_c$	$\frac{5}{4}L_c$
$\frac{\mathcal{L}}{D_j}$	0.353	0.405	0.437	0.371	0.378	0.460	0.95	1.07	0.95
$\frac{\mathcal{T}U_j}{D_j}$	0.569	0.746	0.817	0.820	0.791	0.945	0.69	0.94	0.86
$\frac{U^c}{U_j}$	0.65	0.65	0.65	0.52	0.66	0.67	1.25	0.98	0.97

Table 7.3: Comparison of predicted and measured flow features for *Jet I* and *Jet II*. All values presented are obtained along the nozzle lip line, i.e. $r = 0.5D_j$.

7.4 Predicted Radiated Sound Using Lighthill's Acoustic Analogy

This section reports observer sound pressure levels obtained using Lighthill's acoustic analogy. The performance of this acoustic analogy is compared with that of Kirchhoff surface integration for which the predicted SPL for *Jet I* and *Jet II* was presented in previous sections, see sections 7.1 and 7.2.

Figure 7.74 compares overall sound pressure levels obtained using Kirchhoff and Lighthill's acoustic analogy in both spatial and temporal derivative formulation. The upper two figures are obtained for *Jet I* and the lower ones for *Jet II*. The sound pressure levels obtained using Kirchhoff are, as shown previously, well aligned with measured levels for both jets. As shown in the figures, the spatial derivative formulation of Lighthill's acoustic analogy gives OASPL far over the ones obtained in experiments. The temporal derivative formulation is somewhat better, at least for low angles. From 90° and above, the levels increase rapidly. In the following, only the sound pressure levels obtained using the temporal derivative formulation will be discussed.

Spectra of far-field pressure for a few observers are depicted in figures 7.75 and 7.76 for the unheated and heated jet, respectively. For *Jet I*, the amplitude of the spectra is overpredicted for high Strouhal numbers for high and low angles. However, this overprediction is not as evident in the sound pressure levels obtained for low angles as in those obtained for high angles. The reason for this is probably that the amplitudes at low Strouhal numbers are significantly higher for the low angles and thus the overprediction at high frequencies is not as dominant as for the high angles, see figure 7.75. For the heated jet, see figure 7.76, the amplitude is again overpredicted for high Strouhal numbers. In this case, however, the method fails to predict the spectrum amplitude at low Strouhal numbers. These are here far under the measured levels. This might explain the somewhat better directivity for the heated jet using Lighthill's acoustic analogy, see figure 7.74. That is, it seems that it could be a lucky coincidence that the predicted levels are closer to the measured ones for low angles in this case. The inability to capture the amplitude for low Strouhal numbers still has to be explained. It might be an effect of using an assumption not valid for heated jets when evaluating the Lighthill source term, namely, that the Lighthill tensor can be reduced to only include the Reynolds stress term. According to Lighthill (1952), this assumption is valid only in

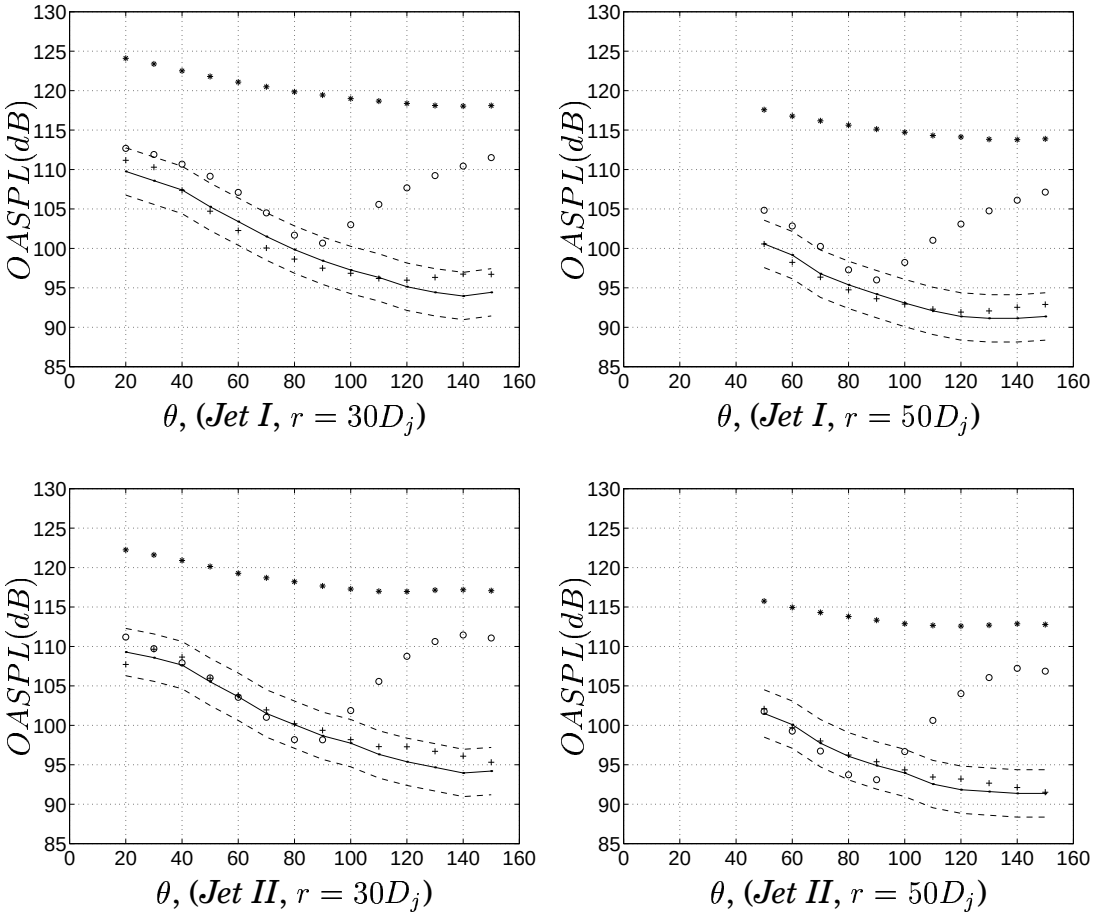

Figure 7.74: Comparison of predicted far-field sound pressure levels using different integral approaches. $'-*'$ denotes measured data and $'--'$ a 3dB deviation from the measured levels. $'+'$ denotes Kirchhoff integration, $'o'$ Lighthill's acoustic analogy on its temporal derivative formulation and $'*'$ the spatial derivative formulation.

flows in which the temperature departs little from uniformity. According to Freund (2003), the entropic part excluded in the simplified version of the Lighthill tensor gives a non-negligible sound contribution, even for isothermal jets. No tests have yet been done to validate that this is the reason for the low amplitudes.

7.4.1 Low-pass Filtering of Observer Pressure Signal

The overpredicted amplitudes in the far-field pressure spectra presented in the previous section might be an effect of the high frequency range being contaminated by spurious waves. This in turn leads to overprediction of sound pressure levels due to the contribution of these unphysical high frequency waves. When using Kirchhoff surface integration, such contributions were filtered out due to the resolution of the mesh, see sections 7.1 and 7.2, whereas, in this case, nothing will be damped out since the integration takes place directly in the source locations. The high amplitudes at high Strouhal numbers are unphysical but might still exist in the simulated flow field. Therefore, filtering approaches were tested in order to see whether these unphysical effects could be diminished. A low-pass second-order Butterworth filter with cut-off frequencies based on the local convection velocity and local cell width was implemented in the solver. Retarded time evaluation of acoustic sources was then evaluated using low-pass filtered data. The effect of post-processing the unfiltered pressure signal using a band-pass filter was also investigated.

Figure 7.77 gives sound pressure levels obtained using the built-in low-pass filter. As can be seen in the figures, the level at high angles for *Jet I* were significantly reduced. For the heated jet, on the other hand, the low-pass filtering was not as successful. The levels became somewhat lower for high angles but were in this case underpredicted for low angles. This is probably an effect of the fact that the low frequency part of the spectra is not accurately captured. However, the decrease of the sound pressure levels indicates the presence of spurious waves in the flow field.

Band-pass filtering of the unfiltered observer pressure signals resulted in the sound pressure levels shown in figure 7.78. In this case, the levels obtained for *Jet I* are in rather good agreement with measurements whereas the levels for *Jet II* are underpredicted. The observer pressure

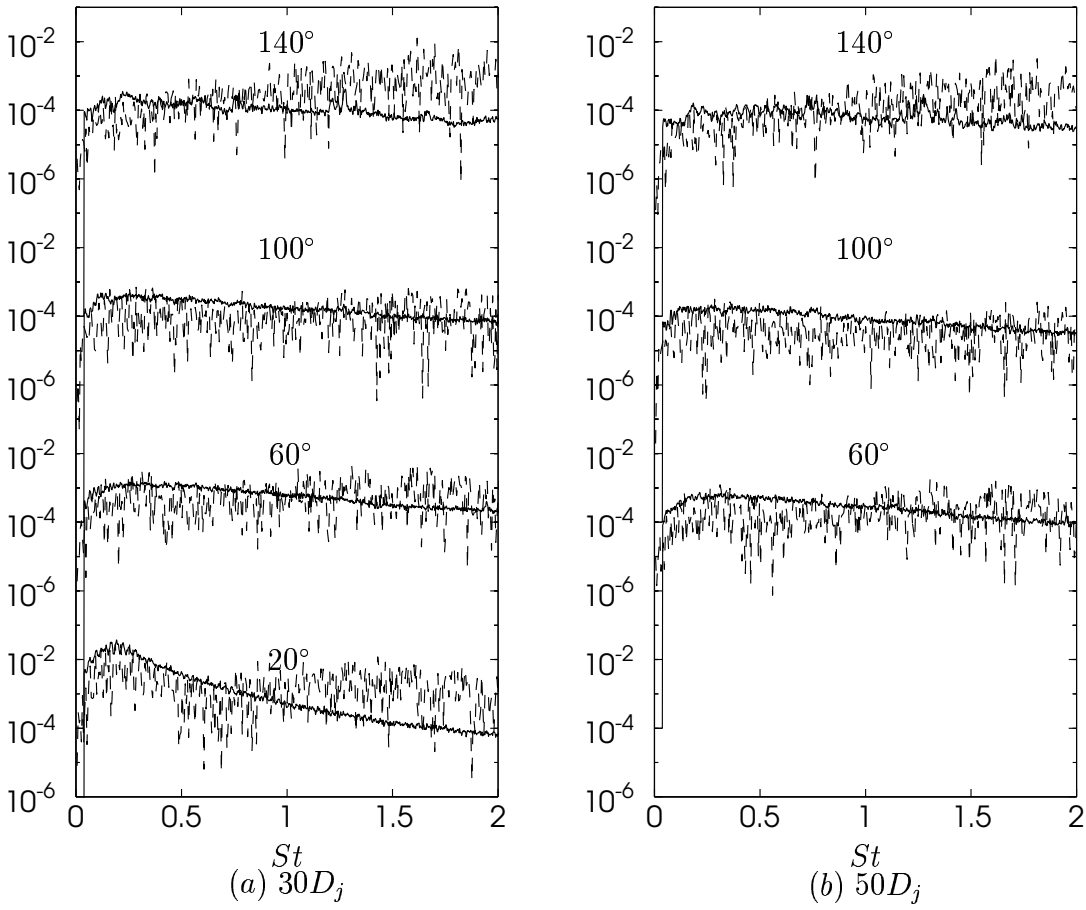

Figure 7.75: Power spectrum of far-field pressure fluctuations versus Strouhal number, $St = fD_j/U_j$, for *Jet I*. The dashed line, $'\ --\ '$ corresponds to data obtained using Lighthill's acoustic analogy in the temporal derivative formulation and the solid line corresponds to experimental data measured by Jordan *et al.* (2002*b*). In figure (a), four observer locations are represented. Starting at a location 20° from the x-axis the angle is increased by an increment of 40° per spectrum. In figure (b) the first spectrum from below is obtained for an observer location 60° from the x-axis, i.e. it should be compared with the second spectrum from below in figure (a). Note that the spectra have been staggered and the scale on the y-axis is therefore repeated.

spectra of band-pass filtered data for the unheated jet, see figure 7.79, looks very much like the ones for the pressure signal obtained using Kirchhoff, see figure 7.32. For *Jet II*, on the other hand, since the low frequency amplitudes were underpredicted, see figure 7.76, filtering

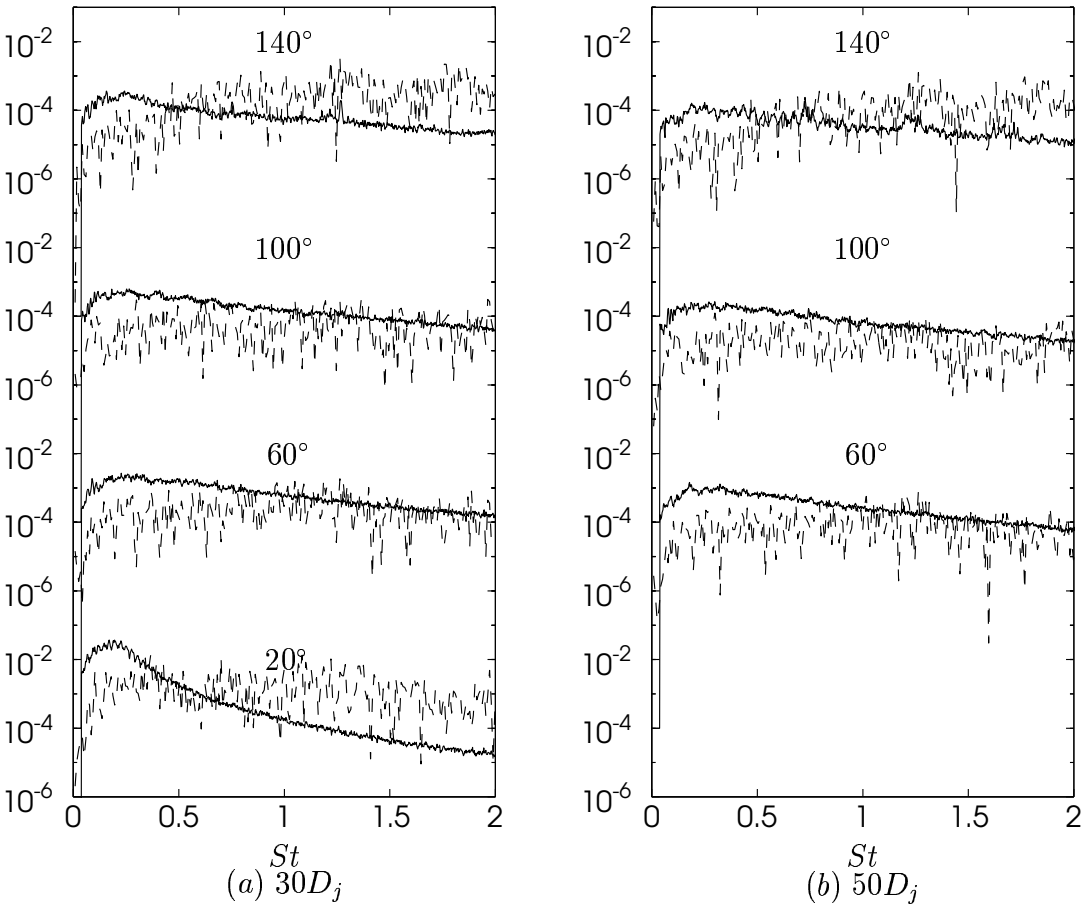

Figure 7.76: Power spectrum of far-field pressure fluctuations versus Strouhal number, $St = fD_j/U_j$, for *Jet II*. For legend see figure 7.75.

the pressure signal leads to underprediction of the sound pressure levels. The pressure fluctuation power spectra for the band-pass filtered *Jet II* data show that the filtering operation results in underpredicted spectrum amplitudes for almost all angles, see figure 7.80.

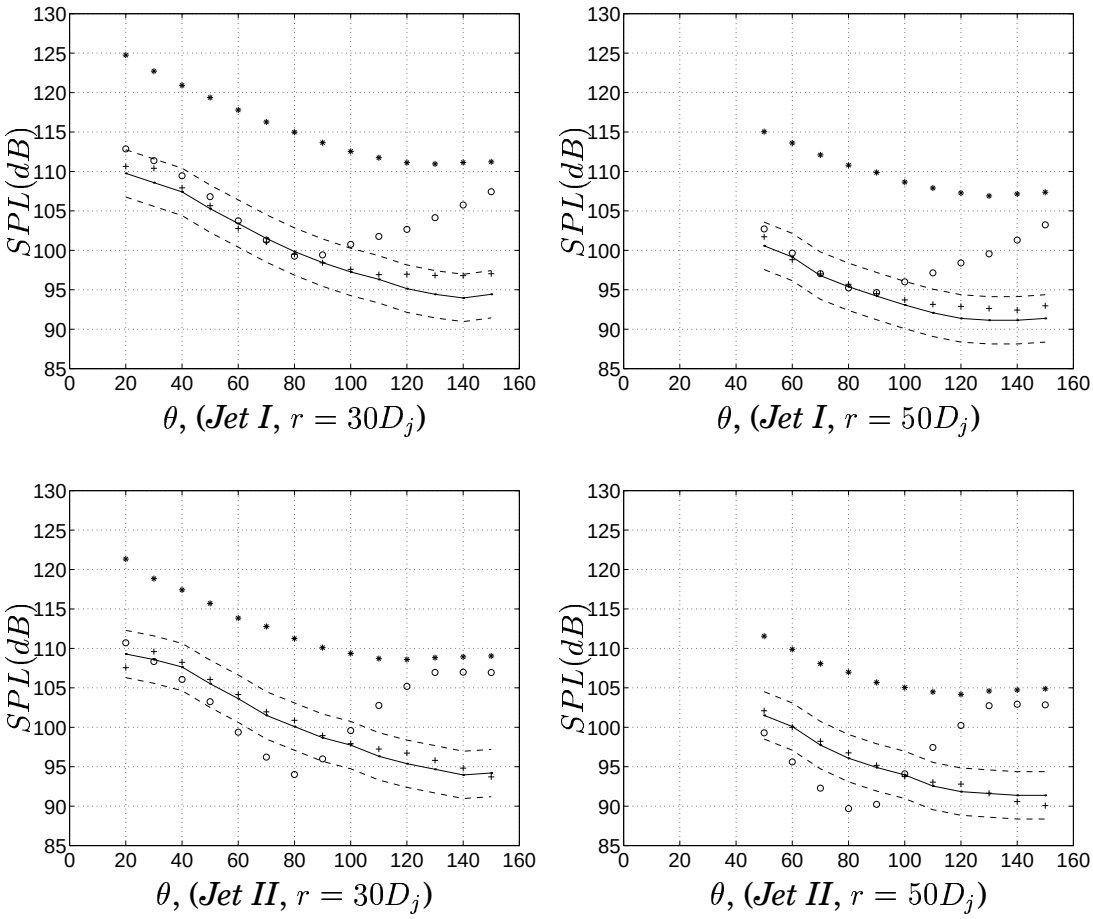

Figure 7.77: Predicted OASPL obtained by implementing a temporal Butterworth filter in the solver. For legend see figure 7.74.

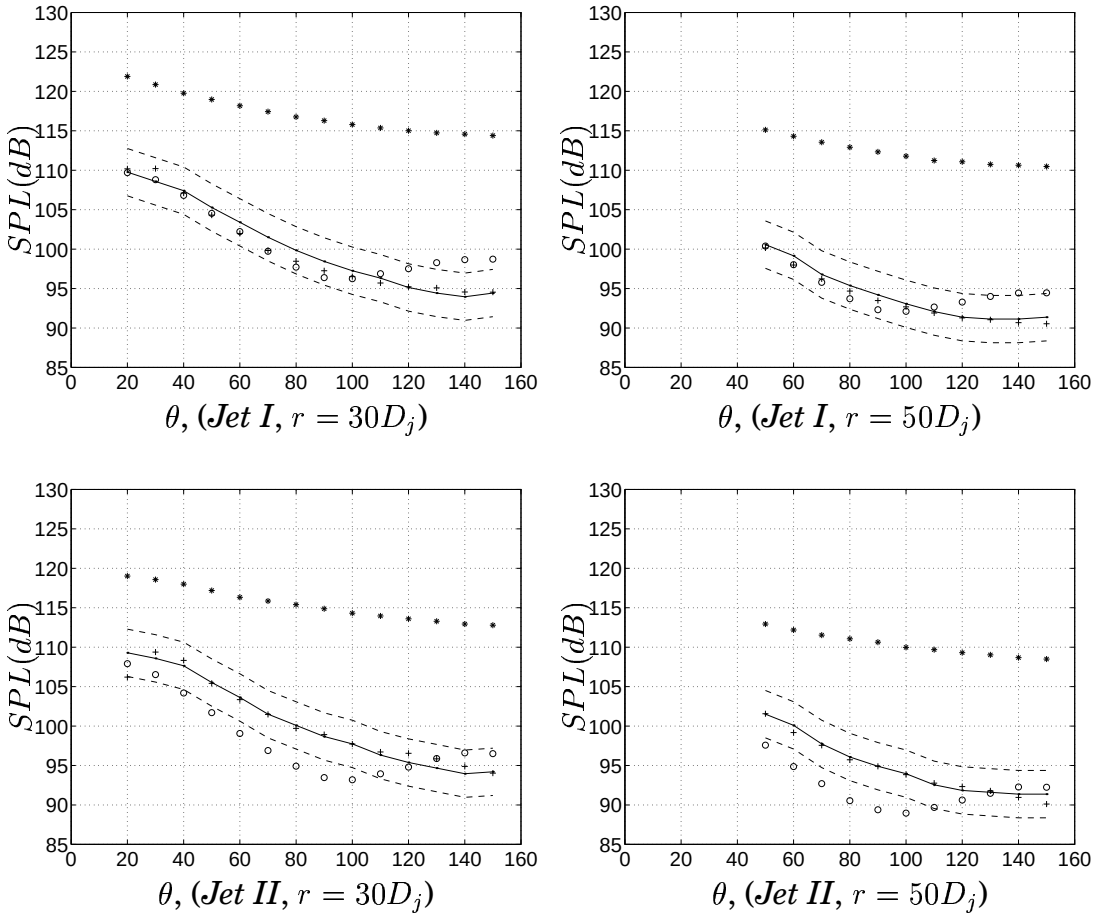

Figure 7.78: SPL obtained using band-pass filtered pressure signal. The upper cut-off frequency corresponds to a Strouhal number of $St = 1.0$ and the lower to $St = 0.05$. For legend see figure 7.74.

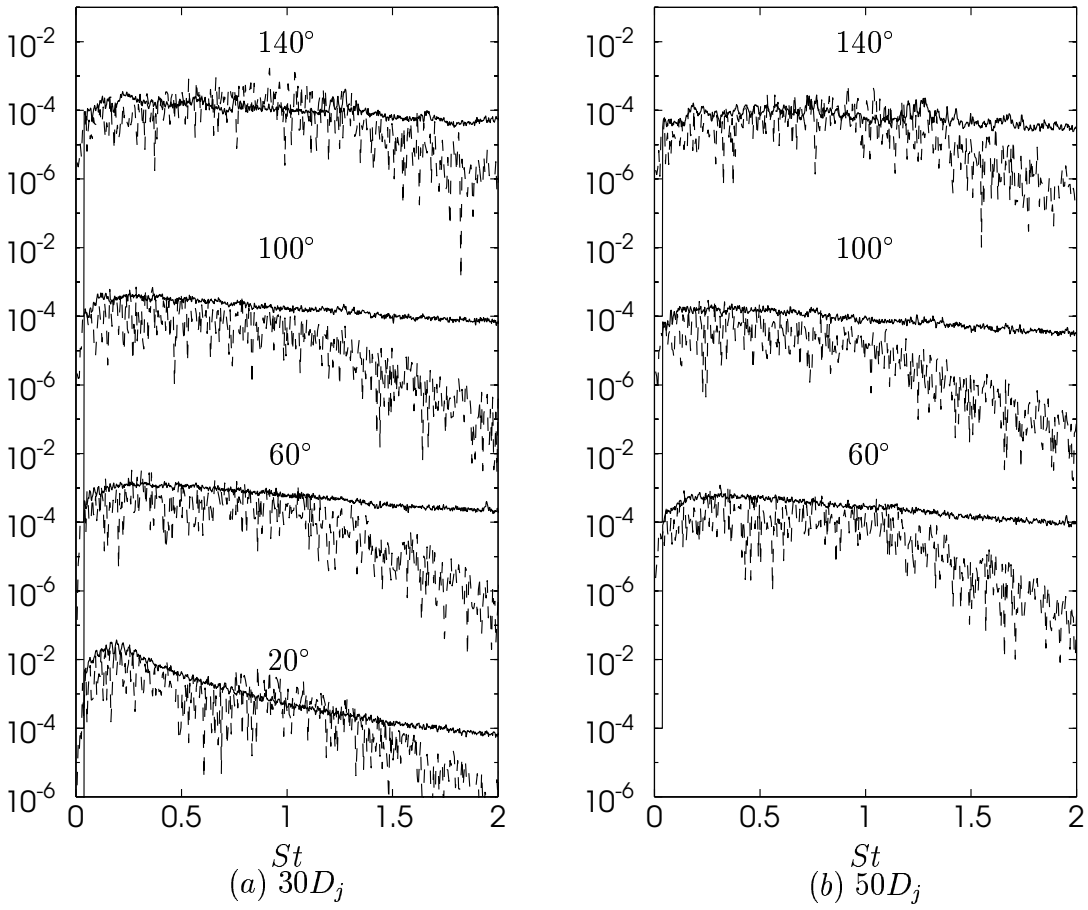

Figure 7.79: Power spectrum of far-field pressure fluctuations versus Strouhal number, $St = fD_j/U_j$, for *Jet I*. These spectra were obtained for band-pass filtered pressure signals. The upper cut-off frequency corresponds to a Strouhal number of $St = 1.0$ and the lower to $St = 0.05$. For legend see figure 7.75.

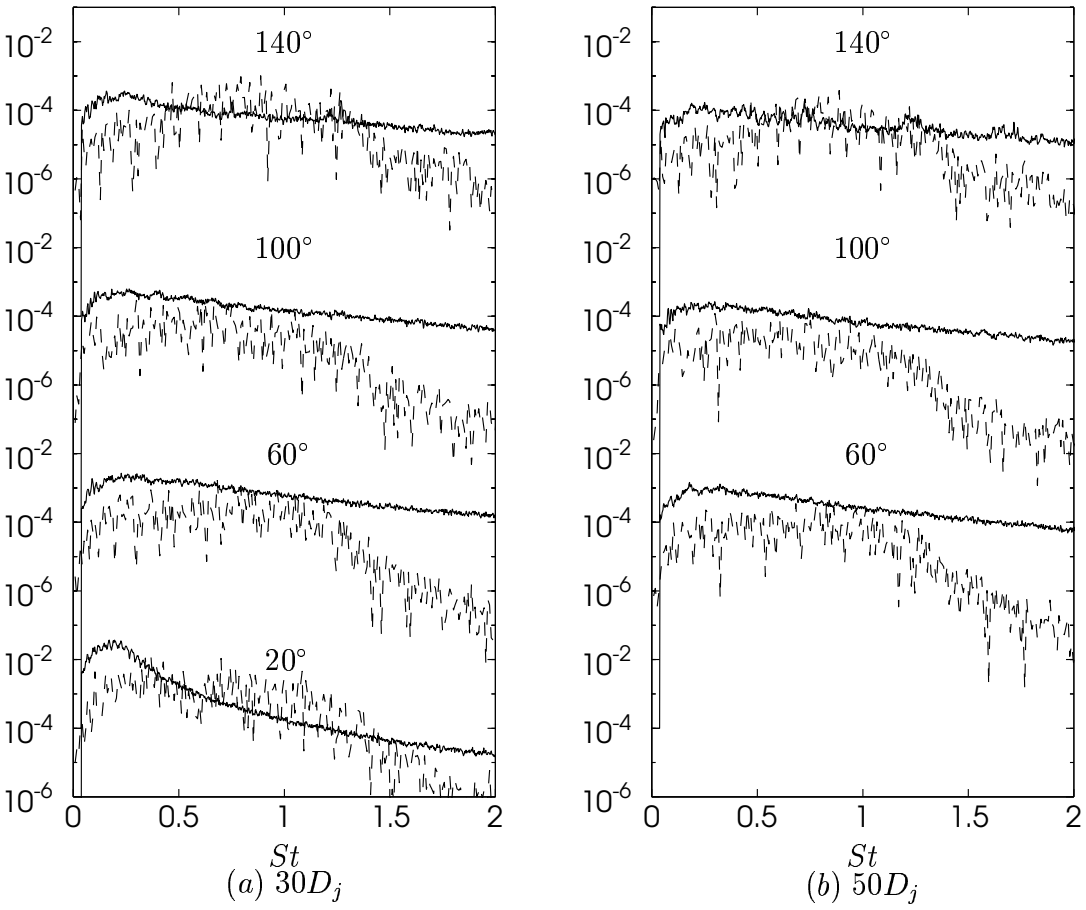

Figure 7.80: Power spectrum of far-field pressure fluctuations versus Strouhal number, $St = fD_j/U_j$, for *Jet II*. These spectra were obtained for band-pass filtered pressure signals. The upper cut-off frequency corresponds to a Strouhal number of $St = 1.0$ and the lower to $St = 0.05$. For legend see figure 7.75.

Chapter 8

Computational Resources

The computations were performed in part on a Sun-cluster using 14 SunBlade 750 MHz processors and in part on a Linux cluster using 14 AMD 1700^{+} processors. MPI[1] routines were implemented for processor communication.

The simulated time of the generated data series used in the evaluations presented in chapter 7 and the corresponding CPU time on the 14 AMD processors are presented below.

Jet I :

- Fully developed jet:
  $2.5 \times 10^{-2}\ [s] \Rightarrow \sim 1556$ CPU hours
- Accumulated statistics:
  $1.5 \times 10^{-1}\ [s] \Rightarrow \sim 9333$ CPU hours
- Time series of flow data used for evaluation of two-point correlations:
  $7.25 \times 10^{-2}\ [s] \Rightarrow \sim 4510$ CPU hours
- Observer pressure signal:
  $3.80 \times 10^{-2}\ [s] \Rightarrow \sim 2364$ CPU hours

Jet II :

- Fully developed jet:
  $2.5 \times 10^{-2}\ [s] \Rightarrow \sim 2593$ CPU hours
- Accumulated statistics (Velocity field):
  $1.05 \times 10^{-1}\ [s] \Rightarrow \sim 10889$ CPU hours

[1]Message Passing Interface

- Accumulated statistics (Heat fluxes):
  6.0×10^{-2} $[s] \Rightarrow \sim$ 7467 CPU hours
- Time series of flow data used for evaluation of two-point correlations:
  7.50×10^{-2} $[s] \Rightarrow \sim$ 7778 CPU hours
- Observer pressure signal:
  2.30×10^{-2} $[s] \Rightarrow \sim$ 2385 CPU hours

Chapter 9

Conclusions

LES of a compressible Mach 0.75 nozzle/jet configuration has been performed. The Reynolds number based on jet velocity and nozzle diameter was 5.0×10^4. Jet simulations were performed at two heating conditions, an unheated jet where the exhaust static temperature was equal to the static temperature of the surrounding air and a heated jet where the nozzle outlet temperature was twice that of the ambient air. Profiles of time and azimuthally averaged flow properties have been compared with data measured by Jordan *et al.* (2002*a*). Although some deviations occur, the results are in general in very good agreement with experiments. The good results are probably attributed to the homogeneity of the mesh used and the fact that a nozzle geometry was included in the calculation domain. Using a combination of cartesian and polar mesh blocks makes it possible to ensure that cells in the outer regions of the calculation domain are not too large and prevent cells from being clustered in the centerline region.

The maximum levels of turbulence intensities are well captured for both jets. Furthermore, the turbulence anisotropy of the jets is correctly predicted. The initial jet spreading and the potential core lengths are however not predicted correctly. This might be due to the use of a grid too coarse in the nozzle outlet region, i.e. too coarse for the subgrid scale model used. Furthermore, the entrainment velocities specified at the free boundaries probably affect the jet spreading.

Two-point space-time correlations were obtained in a number of locations in the shear layer along the nozzle lip-line. Correlation curves obtained at $x = L_c$ were in good agreement with experiments (Jordan & Gervais, 2003). Two-point space-time correlations in the shear layer were used to obtain estimates of integral length scales, integral time scales and eddy convection velocities. The agreement with correspond-

ing quantities obtained from the measured data were satisfying.

Sound pressure levels in the far-field were evaluated with hybrid approaches. Kirchhoff surface integration and Lighthill's acoustic analogy were utilized for the propagation of sound to far-field locations. Instantaneous pressure on the Kirchhoff surface and volume sources, i.e. second-order temporal and spatial derivatives of the Lighthill tensor, were obtained from the LES. Sound pressure levels obtained using Kirchhoff surface integration were in excellent agreement with the levels measured by Jordan *et al.* (2002*b*) for both jets. However, the mesh used fails to capture waves of Strouhal numbers higher than $St \simeq 1.2$. This results in a rapid fall-off of the spectrum amplitudes for higher Strouhal numbers. The lower part of the spectra is accurately captured, however. Since the sound pressure levels obtained were in good agreement with the measured levels, capturing the lower part of the spectra seems to be sufficient to represent the main part of the radiated sound. When Lighthill's acoustic analogy was used for sound propagation, the amplitude of the observer pressure fluctuation power spectra were overpredicted for high Strouhal numbers. This indicates the existence of unphysical high frequency waves in the hydrodynamic field. Because the mesh in the outer regions of the jet does not support these waves, they were damped out by numerical dissipation as the Kirchhoff surface was approached. That is, the mesh acts as a low-pass filter on the acoustic waves traveling through the domain. For upstream observers, however, some of these higher frequencies contributed to the overall sound, since the mesh in this direction is significantly finer than in the downstream direction. The observer pressure signals were band-pass filtered to investigate whether the effect of these frequencies could be diminished, which significantly improved the results for the upstream observers.

No filtering of high frequency contributions occurs with Lighthill's acoustic analogy since the integration takes place directly at the source locations. In this case, filtering the observer pressure signals improved the sound pressure levels for the unheated jet. For the heated jet, on the other hand, filtering did not result in particularly improved sound pressure levels. The deviations from the measured levels decreased to some degree for the upstream angles but the sound pressure levels were underpredicted for the downstream observer locations. The reason for this is that Lighthill's acoustic analogy fails to predict the low frequency part of the spectra when the jet is heated. This might be an effect of using the assumption that the Lighthill tensor can be sim-

plified to include only the Reynolds stress part, which is only valid for unheated flows.

With a surface integral approach, it is sufficient to use a mesh resolving the main noise generation structures and supporting acoustic waves within the frequency range contributing most to the overall sound pressure levels. However, if the aim is to capture the sound spectra in far-field locations, higher mesh resolution and probably higher-order schemes would be desirable.

It is worth mentioning that the results presented in this thesis have been obtained although a less accurate numerical scheme and a mesh of lower resolution than recommended for aeroacoustic applications were used.

Chapter 10

Future Work

The main deviation from the measured flow field was for both the simulated jets a somewhat shorter potential core, i.e. a shorter mixing region. This does not seem to affect the obtained far-field sound pressure levels a great deal. Still, it would be interesting to investigate the reasons for this underprediction. Possible causes are inadequate mesh resolution and the subgrid scale model used.

The far-field observer signals of acoustic pressure fluctuations were contaminated by high frequency spurious noise when Lighthill's acoustic analogy was used for sound propagation. Sources of such high frequency waves have to be identified. The fact that some of these effects occurred even when Kirchhoff surface integration was used for sound propagation, indicates the presence of spurious waves in the flow field. Moreover, spurious noise might be generated in the evaluation of the Lighthill tensor derivative.

For the heated jet, Lighthill's acoustic analogy, as it was implemented in this work, failed to capture the low frequency range of the pressure signal. Since the low frequencies contribute most to the radiated sound, it is of great importance to be able to represent these waves accurately. Therefore, the importance of the terms of the Lighthill tensor excluded in this work needs to be investigated.

Using Kirchhoff surface integration, the directivity of radiated sound was well captured. However, since the integration surface has to be placed outside the hydrodynamic region, the mesh in the integration surface region was not fine enough to support waves in the high frequency range. Using the surface integration formulation of Ffowcs Williams & Hawkings (1969) on its porous surface form would make it possible to use a narrower integration surface since this method al-

lows hydrodynamic fluctuations to cross the surface. Furthermore, the source region could be completely enclosed by the surface since this method enables the downstream closing surface to be included.

Bibliography

ANDERSSON, N., DAVIDSON, L. & ERIKSSON, L.-E. 2003 Large-Eddy Simulation of a Mach 0.75 jet. In *The 9th AIAA/CEAS Aeroacoustic Conference*, *AIAA 2003* 3312. Hilton Head, South Carolina.

BILLSON, M. 2002 Computational techniques for jet noise predictions. Lic. thesis, Department of Thermo and Fluid Dynamics, Chalmers University of Technology, Gothenburg.

BILLSON, M., ERIKSSON, L.-E. & DAVIDSON, L. 2002 Acoustic source terms for the linear Euler equations on conservative form. In *The 8th AIAA/CEAS Aeroacoustics Conference*, *AIAA 2002* 2582. Breckenridge, Colorado.

BOERSMA, B., BRETHOUWER, G. & NIEUWSTADT, F. 1998 A numerical investigation on the effect of the inflow conditions on the self-similar region of a round jet. *Physics of Fluids* **10** (4), 899–909.

BOGEY, C. & BAILLY, C. 2003 LES of a high Reynolds, high subsonic jet : effects of the inflow conditions on flow and noise. In *The 9th AIAA/CEAS Aeroacoustic Conference*, *AIAA 2003* 3170. Hilton Head, South Carolina.

BOGEY, C., BAILLY, C. & JUVÉ, D. 2000*a* Computation of the sound radiated by a 3-D jet using Large Eddy Simulation. In *The 6th AIAA/CEAS Aeroacoustic Conference*, *AIAA 2000* 2009. Lahaina, Hawaii.

BOGEY, C., BAILLY, C. & JUVÉ, D. 2000*b* Numerical simulation of sound generated by vortex pairing in a mixing layer. *AIAA Journal* **38** (12), 2210–2218.

BOGEY, C., BAILLY, C. & JUVÉ, D. 2001 Noise computation using Lighthill's equation with inclusion of mean flow - acoustic interactions. In *The 7th AIAA/CEAS Aeroacoustic Conference*, *AIAA 2001* 2255. Maastricht, Netherlands.

BOGEY, C., BAILLY, C. & JUVÉ, D. 2003 Noise investigation of a high subsonic, moderate Reynolds number jet using a compressible Large Eddy Simulation. *Theoret. Comput. Fluid Dynamics* **16** (4), 273–297.

COLONIUS, T. & FREUND, J. 2000 Application of Lighthill's equation to a Mach 1.92 turbulent jet. *AIAA Journal* **38** (2), 368–370.

COLONIUS, T., LELE, S. & MOIN, P. 1993 Boundary conditions for direct computation of aerodynamic sound generation. *AIAA Journal* **31** (9), 1574–1582.

DEBONIS, J. & SCOTT, J. 2001 A Large-Eddy Simulation of a turbulent compressible round jet. In *The 7th AIAA/CEAS Aeroacoustic Conference*, *AIAA 2001* 2254. Maastricht, Netherlands.

ERIKSSON, L.-E. 1995 Development and validation of highly modular flow solver versions in g2dflow and g3dflow. Internal report 9970-1162. Volvo Aero Corporation, Sweden.

ERIKSSON, L.-E. 2002 RANS prediction for test cases. Project deliverable D1.5, JEAN - EU 5th Framework Programme, G4RD-CT2000-00313. Volvo Aero Corporation, Sweden.

ERIKSSON, L.-E. 2003 Compressible CFD. Lecture notes. Division of Thermo and Fluid Dynamics, Chalmers University of Technology, Gothenburg, Sweden.

ERLEBACHER, G., HUSSAINI, M., SPEZIALE, C. & ZANG, T. 1992 Toward the large-eddy simulation of compressible turbulent flows. *Journal of Fluid Mechanics* **238**, 155–185.

FFOWCS WILLIAMS, J. & HAWKINGS, D. 1969 Sound generated by turbulence and surfaces in arbitrary motion. *Phil. Trans. Roy. Soc.* **A 264**, 321–342.

FISHER, M. & DAVIES, P. 1963 Correlation measurements in a non-frozen pattern of turbulence. *Journal of Fluid Mechanics* **18**, 97–116.

FREUND, J. 2001 Noise sources in a low-Reynolds-number turbulent jet at Mach 0.9. *Journal of Fluid Mechanics* **438**, 277–305.

FREUND, J. 2003 Noise-source turbulence statistics and the noise from a Mach 0.9 jet. *Physics of Fluids* **15** (6), 1788–1799.

FREUND, J., LELE, S. & MOIN, P. 1996 Calculation of the radiated sound field using an open Kirchhoff surface. *AIAA Journal* **34** (5), 909–916.

FREUND, J., LELE, S. & MOIN, P. 2000 Numerical simulation of a Mach 1.92 jet and its sound field. *AIAA Journal* **38** (11), 2023–2031.

GEORGE, W. 1989 The self-preservation of turbulent flows and its relation to initial conditions and coherent structures. In *Advances in Turbulence* (ed. W. George & R. Arndt), pp. 39–73. New York: Springer.

GEORGE, W. 2000 Introduction to turbulence. Internal report. Dept. of Thermo and Fluid Dynamics, Chalmers.

HINZE, J. 1975 *Turbulence*, 2nd edn. McGraw Hill, iSBN 0-07-029037-7.

HUSSEIN, H., CAPP, S. & GEORGE, W. 1994 Velocity measurements in a high-Reynolds-number, momentum-conserving, axisymmetric, turbulent jet. *Journal of Fluid Mechanics* **258**, 31–75.

JEONG, J. & HUSSAIN, F. 1995 On the identification of a vortex. *Journal of Fluid Mechanics* **285**, 69–94.

JORDAN, P. 2003 private communication. Laboratoire d'Etude Aeródynamiques, Poitiers.

JORDAN, P. & GERVAIS, Y. 2003 Modeling self and shear noise mechanisms in anisotropic turbulence. In *The 9th AIAA/CEAS Aeroacoustic Conference*, *AIAA 2003* 8743. Hilton Head, South Carolina.

JORDAN, P., GERVAIS, Y., VALIÉRE, J.-C. & FOULON, H. 2002*a* Final results from single point measurements. Project deliverable D3.4, JEAN - EU 5th Framework Programme, G4RD-CT2000-00313. Laboratoire d'Etude Aeródynamiques, Poitiers.

JORDAN, P., GERVAIS, Y., VALIÉRE, J.-C. & FOULON, H. 2002*b* Results from acoustic field measurements. Project deliverable D3.6, JEAN - EU 5th Framework Programme, G4RD-CT2000-00313. Laboratoire d'Etude Aeródynamiques, Poitiers.

LARSSON, J. 2002 Computational aero acoustics for vehicle applications. Lic. thesis, Department of Thermo and Fluid Dynamics, Chalmers University of Technology, Gothenburg.

LARSSON, J., DAVIDSON, L., OLSSON, M. & ERIKSSON, L.-E. 2003 Aero acoustic investigation of an open cavity at low Mach number. In *The 9th AIAA/CEAS Aeroacoustic Conference*, *AIAA 2003* 3237. Hilton Head, South Carolina.

LIGHTHILL, M. 1952 On sound generated aerodynamically, I. General theory. *Proc. Roy. Soc.* **A 211**, 564–587.

LIGHTHILL, M. 1953 On sound generated aerodynamically, II. Turbulence as a source of sound. *Proc. Roy. Soc.* **A 222**, 1–32.

LYRINTZIS, A. 1994 Review: The use of Kirchhoff's method in computational aeroacoustics. *ASME: Journal of Fluids Engineering* **116**, 665–676.

MANKBADI, R. 1999 Review of computational aeroacoustics in propulsion systems. *J. Propulsion and Power* **15** (4), 504–512.

MANKBADI, R., SHIH, S., HIXON, R. & POVINELLI, L. 2000 Direct computation of jet noise produced by large-scale axisymmetric structures. *J. Propulsion and Power* **16** (2), 207–215.

MITCHELL, B., LELE, S. & MOIN, P. 1999 Direct computation of the sound generated by vortex pairing in an axisymmetric jet. *Journal of Fluid Mechanics* **383**, 113–142.

MORRIS, P., SCHEIDEGGER, T. & LONG, L. 2000 Jet noise simulations for circular nozzles. In *The 6th AIAA/CEAS Aeroacoustic Conference*, *AIAA 2000* 2009. Lahaina, Hawaii.

PANTON, R. 1995 *Incompressible Flow*, 2nd edn. John Wiley & Sons, Inc., iSBN 0-471-59358-3.

REMBOLD, B., ADAMS, N. & KLEISER, L. 2002 Direct numerical simulation of a transitional rectangular jet. *International Journal of Heat and Fluid Flow* **23** (5), 547–553.

RIBAULT, C. L., SARKAR, S. & STANLEY, S. 1999 Large Eddy Simulation of a plane jet. *Physics of Fluids* **11** (10), 3069–3083.

RIBNER, H. 1969 Quadrupole correlations governing the pattern of jet noise. *Journal of Fluid Mechanics* **38**, 1–24.

SHUR, M., SPALART, P., STRELETS, M. & TRAVIN, A. 2003 Towards the prediction of noise from jet engines. *International Journal of Heat and Fluid Flow* **24** (4), 551–561.

SMAGORINSKY, J. 1963 General circulation experiment with the primitive equations. I. The basic experiment. *Monthly Weather Review* **91** (3), 99–165.

TAM, C. 1998 Jet noise: since 1952[1]. *Theoret. Comput. Fluid Dynamics* **10**, 393–405.

WILCOX, D. 1998 *Turbulence Modeling for CFD*, 2nd edn. DCW Industries Inc., iSBN 0-9636051-5-1.

WYGNANSKI, I. & FIEDLER, H. 1969 Some measurements in the self-preserving jet. *Journal of Fluid Mechanics* **38**, 577–612.

ZHAO, W., FRANKEL, S. & MONGEAU, L. 2001 Large Eddy Simulation of sound radiation from subsonic turbulent jets. *AIAA Journal* **39** (8), 1469–1477.

Appendix A

Characteristic Variables

For a homogeneous flow, the Euler equations, i.e. the inviscid part of the Navier-Stokes equations, may be rewritten in a quasi-linear form as

$$\frac{\partial Q}{\partial t} + \frac{\partial \mathcal{F}_i}{\partial Q}\frac{\partial Q}{\partial x_i} = 0 \tag{A.1}$$

Matrices $\frac{\partial \mathcal{F}_i}{\partial Q}$ are often referred to as flux Jacobians. For local analysis, the flux Jacobians may be regarded as constants and thus a linear relation can be obtained

$$\frac{\partial Q}{\partial t} + \left(\frac{\partial \mathcal{F}_i}{\partial Q}\right)_0 \frac{\partial Q}{\partial x_i} = 0 \tag{A.2}$$

In equation A.2, subscript 0 denotes the reference state for which the flux Jacobians have been evaluated. Assuming that the perturbations correspond to planar waves in space with the plane normal aligned with the vector $(\alpha_1, \alpha_2, \alpha_3)$ for which $\alpha_i \alpha_i = 1$, equation A.2 can be rewritten as

$$\frac{\partial Q}{\partial t} + \tilde{A}_0 \frac{\partial Q}{\partial \xi} = 0 \tag{A.3}$$

where

$$\tilde{A}_0 = \alpha_i \left(\frac{\partial \mathcal{F}_i}{\partial Q}\right)_0 \tag{A.4}$$

is a linear combination of the flux Jacobians and

$$\xi = \alpha_i x_i \tag{A.5}$$

is a coordinate aligned with the wave plane normal vector. Equation A.3 is a coupled system of one-dimensional linear equations describing the propagation of waves along the ξ-axis. Matrices T and T^{-1}

are found such that matrix $\tilde{A}_0$ is diagonalized using a standard eigen-decomposition procedure

$$T\tilde{A}_0T^{-1} = \Lambda = \begin{bmatrix} \lambda_1 & 0 & 0 & 0 & 0 \\ 0 & \lambda_2 & 0 & 0 & 0 \\ 0 & 0 & \lambda_3 & 0 & 0 \\ 0 & 0 & 0 & \lambda_4 & 0 \\ 0 & 0 & 0 & 0 & \lambda_5 \end{bmatrix} \tag{A.6}$$

The eigenvalues $(\lambda_1, \ldots, \lambda_5)$ can be calculated analytically as

$$\begin{aligned} \lambda_1 &= \lambda_2 = \lambda_3 = \alpha_i u_i \\ \lambda_4 &= \lambda_1 + c\sqrt{\alpha_i\alpha_i} \\ \lambda_5 &= \lambda_1 - c\sqrt{\alpha_i\alpha_i} \end{aligned} \tag{A.7}$$

Introducing the characteristic variables defined as

$$W = T^{-1}Q \tag{A.8}$$

the system of linear equations given by A.3 can be written as a uncoupled set of linear transport equations

$$\frac{\partial W}{\partial t} + \Lambda\frac{\partial W}{\partial \xi} = 0 \tag{A.9}$$

Each of the five components, w_i, of the W vector is a characteristic variable transported in a direction aligned with the ξ-axis with the characteristic speed described by the corresponding eigenvalue, λ_i. The first of the five characteristic variables may be interpreted physically as an entropy wave, the following as vorticity waves and the last two as acoustic waves.

Appendix B

Physical and Computational Space

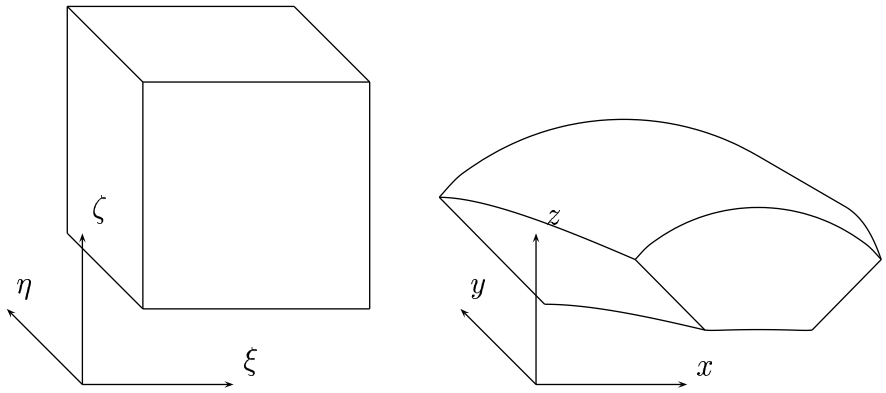

Figure B.1: A domain depicted in computational space and physical space.

An arbitrary mapping between the computational domain coordinates, i.e. (ξ, η, ζ), and the coordinates in the physical domain, i.e. (x, y, z), or vice versa, in three dimensions can be expressed as follows

$$\left\{ \begin{array}{rcl} x & = & x\left(\xi,\eta,\zeta\right) \\ y & = & y\left(\xi,\eta,\zeta\right) \\ z & = & z\left(\xi,\eta,\zeta\right) \end{array} \right. , \left\{ \begin{array}{rcl} \xi & = & \xi\left(x,y,z\right) \\ \eta & = & \eta\left(x,y,z\right) \\ \zeta & = & \zeta\left(x,y,z\right) \end{array} \right. \tag{B.1}$$

Differentiating the mapping from the physical to the computational domain gives

$$\begin{array}{rcl} dx &=& x_\xi d\xi + x_\eta d\eta + x_\zeta d\zeta \\ dy &=& y_\xi d\xi + y_\eta d\eta + y_\zeta d\zeta \\ dz &=& z_\xi d\xi + z_\eta d\eta + z_\zeta d\zeta \end{array} \tag{B.2}$$

$$\begin{bmatrix} dx \\ dy \\ dz \end{bmatrix} = \begin{bmatrix} x_\xi & x_\eta & x_\zeta \\ y_\xi & y_\eta & y_\zeta \\ z_\xi & z_\eta & z_\zeta \end{bmatrix} \begin{bmatrix} d\xi \\ d\eta \\ d\zeta \end{bmatrix} = A \begin{bmatrix} d\xi \\ d\eta \\ d\zeta \end{bmatrix}$$

where subscripts ξ, η and ζ denote differentiation with respect to the coordinates in computational space, e.g. $x_\xi = \frac{\partial x}{\partial \xi}$. Differentiating the mapping from the computational to the physical domain gives

$$\begin{array}{rcl} d\xi &=& \xi_x dx + \xi_y dy + \xi_z dz \\ d\eta &=& \eta_x dx + \eta_y dy + \eta_z dz \\ d\zeta &=& \zeta_x dx + \zeta_y dy + \zeta_z dz \end{array} \tag{B.3}$$

$$\begin{bmatrix} d\xi \\ d\eta \\ d\zeta \end{bmatrix} = \begin{bmatrix} \xi_x & \xi_y & \xi_z \\ \eta_x & \eta_y & \eta_z \\ \zeta_x & \zeta_y & \zeta_z \end{bmatrix} \begin{bmatrix} dx \\ dy \\ dz \end{bmatrix} = A^{-1} \begin{bmatrix} dx \\ dy \\ dz \end{bmatrix}$$

where the inverse of A can be calculated from A as follows using the cofactor method

$$\left[A^{-1}\right]_{ij} = \frac{(-1)^{i+j}}{det\,(A)} D_{ji} \tag{B.4}$$

D_{ij} is a sub-determinant of A obtained by deleting the i^{th} row and the j^{th} column. The inverse of A can now be expressed in terms of coordinates in the physical domain differentiated with respect to the coordinates in the computational domain as follows

$$A^{-1} = \frac{1}{det\,(A)} \begin{bmatrix} (y_\eta z_\zeta - y_\zeta z_\eta) & (x_\zeta z_\eta - x_\eta z_\zeta) & (x_\eta y_\zeta - x_\zeta y_\eta) \\ (y_\zeta z_\xi - y_\xi z_\zeta) & (x_\xi z_\zeta - x_\zeta z_\xi) & (x_\zeta y_\xi - x_\xi y_\zeta) \\ (y_\xi z_\eta - y_\eta z_\xi) & (x_\eta z_\xi - x_\xi z_\eta) & (x_\xi y_\eta - x_\eta y_\xi) \end{bmatrix} \tag{B.5}$$

where the determinant of A is calculated as

$$det\,(A) = x_\xi\,(y_\eta z_\zeta - y_\zeta z_\eta) + y_\xi\,(x_\zeta z_\eta - x_\eta z_\zeta) + z_\xi\,(x_\zeta y_\eta - x_\eta y_\zeta) \tag{B.6}$$

Differentiating a flow variable, Φ, with respect to ξ, η and ζ implies

$$\begin{aligned} d\Phi =& \frac{\partial \Phi}{\partial \xi} d\xi + \frac{\partial \Phi}{\partial \eta} d\eta + \frac{\partial \Phi}{\partial \zeta} d\zeta = \begin{bmatrix} \frac{\partial \Phi}{\partial \xi} & \frac{\partial \Phi}{\partial \eta} & \frac{\partial \Phi}{\partial \zeta} \end{bmatrix} \begin{bmatrix} d\xi \\ d\eta \\ d\zeta \end{bmatrix} \\ =& \begin{bmatrix} \frac{\partial \Phi}{\partial \xi} & \frac{\partial \Phi}{\partial \eta} & \frac{\partial \Phi}{\partial \zeta} \end{bmatrix} A^{-1} \begin{bmatrix} dx \\ dy \\ dz \end{bmatrix} \end{aligned} \tag{B.7}$$

Differentiating the same flow variable with respect to x, y and z gives

$$d\Phi = \frac{\partial \Phi}{\partial x}dx + \frac{\partial \Phi}{\partial z}dy + \frac{\partial \Phi}{\partial z}dz = \left[\begin{array}{ccc} \frac{\partial \Phi}{\partial x} & \frac{\partial \Phi}{\partial y} & \frac{\partial \Phi}{\partial z} \end{array} \right] \left[\begin{array}{c} dx \\ dy \\ dz \end{array} \right] \tag{B.8}$$

By identification of terms on the right hand side of equation B.7 and equation B.8, respectively, a relation between spatial derivatives in computational space and physical space can be obtained as

$$\left[\begin{array}{ccc} \frac{\partial \Phi}{\partial x} & \frac{\partial \Phi}{\partial y} & \frac{\partial \Phi}{\partial z} \end{array} \right] = \left[\begin{array}{ccc} \frac{\partial \Phi}{\partial \xi} & \frac{\partial \Phi}{\partial \eta} & \frac{\partial \Phi}{\partial \zeta} \end{array} \right] A^{-1} \tag{B.9}$$

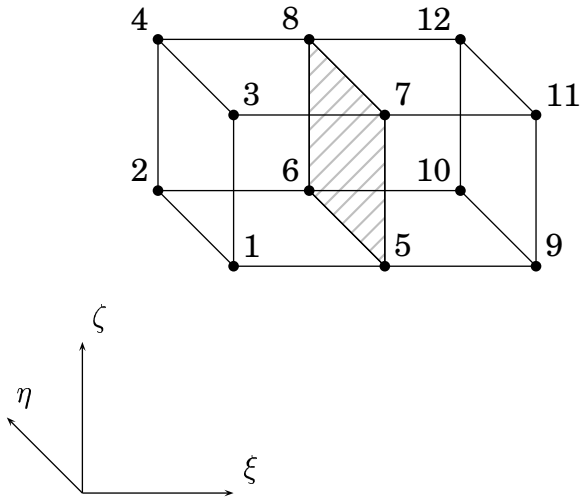

Figure B.2: Two neighboring cells in computational space, i.e. (ξ, η, ζ)-space, defined by the corner points $1 - 12$.

Using the twelve corner points defining two neighboring cells, see figure B.2, derivatives of the physical space coordinates with respect to the coordinates in computational space at the cell face can be obtained as follows.

$$
\begin{aligned}
\frac{\partial x}{\partial \xi} &= \frac{1}{8}\left[\ (x_9 + x_{10} + x_{11} + x_{12}) - (x_1 + x_2 + x_3 + x_4)\ \right] \\
\frac{\partial y}{\partial \xi} &= \frac{1}{8}\left[\ (y_9 + y_{10} + y_{11} + y_{12}) - (y_1 + y_2 + y_3 + y_4)\ \right] \\
\frac{\partial z}{\partial \xi} &= \frac{1}{8}\left[\ (z_9 + z_{10} + z_{11} + z_{12}) - (z_1 + z_2 + z_3 + z_4)\ \right]
\end{aligned}
$$

$$
\begin{aligned}
\frac{\partial x}{\partial \eta} &= \frac{1}{2}\left[\ (x_6 + x_8) - (x_5 + x_7)\ \right] \\
\frac{\partial y}{\partial \eta} &= \frac{1}{2}\left[\ (y_6 + y_8) - (y_5 + y_7)\ \right] \\
\frac{\partial z}{\partial \eta} &= \frac{1}{2}\left[\ (z_6 + z_8) - (z_5 + z_7)\ \right]
\end{aligned}
\tag{B.10}
$$

$$
\begin{aligned}
\frac{\partial x}{\partial \zeta} &= \frac{1}{2}\left[\ (x_7 + x_8) - (x_5 + x_6)\ \right] \\
\frac{\partial y}{\partial \zeta} &= \frac{1}{2}\left[\ (y_7 + y_8) - (y_5 + y_6)\ \right] \\
\frac{\partial z}{\partial \zeta} &= \frac{1}{2}\left[\ (z_7 + z_8) - (z_5 + z_6)\ \right]
\end{aligned}
$$